UCSF
UC San Francisco Electronic Theses and Dissertations

Title

Dynamic fibroblast-immune interactions shape wound healing after brain injury

Permalink

https://escholarship.org/uc/item/6p7908n4

Author

Ewing-Crystal, Nathan

Publication Date

2025

Supplemental Material

https://escholarship.org/uc/item/6p7908n4#supplemental

Peer reviewed|Thesis/dissertation

eScholarship.org Powered by the California Digital Library
University of California

Dynamic fibroblast-immune interactions shape wound healing after brain injury

by
Nathan Alexander Ewing-Crystal

DISSERTATION
Submitted in partial satisfaction of the requirements for degree of
DOCTOR OF PHILOSOPHY

in

Biomedical Sciences

in the

GRADUATE DIVISION
of the
UNIVERSITY OF CALIFORNIA, SAN FRANCISCO

Approved:

DocuSigned by:
Dean Sheppard
101CEA27F0AF442...

Dean Sheppard
Chair

DocuSigned by:

Thomas Arnold

DocuSigned by:
Adrian Erlebacher

Adrian Erlebacher

DocuSigned by:
Ari Molofsky

Ari Molofsky

DocuSigned by:
Tien Peng
256E38508AB94C9...

Tien Peng
Committee Members

ACKNOWLEDGMENTS

This dissertation is dedicated to the many people without whom the work described herein, and the scientific and personal development that enabled this work, would not have been possible. I feel incredibly lucky to have begun my scientific career at UCSF with the support of a wonderful mentor, a brilliant group of lab-mates and friends, and a loving family, all of whom have supported me the whole way.

First, without my mentor and PI, Dr. Ari Molofsky, neither this project nor my progress through graduate school would have been possible. I met Ari during my first year of medical school, and though I did not consider a rotation in his lab until a year later, when I became fascinated by neuroimmunology, I remember thinking that he seemed like a rigorous scientist and a caring, thoughtful mentor. I began my second rotation of graduate school in Ari's lab, intending to embark upon a third rotation before deciding on a thesis lab; by a few weeks into my rotation, it was clear that I would not need another. A large part of this was due to Ari himself. He was a never-ending source of encouragement, finding ways to layer suggestions for improving experiments, analyses, presentations, and more in between congratulations for successful experiments – or, more commonly (and more importantly), acknowledgments of the value of unsuccessful experiments. He was a well of optimism, and he was often the difference between outright despair and hopeful reinterpretation after receiving negative data. One of his best qualities, which I hope to emulate one day, is his ability to always focus on the bigger picture, even while carefully considering each detail. Over the past four years, Ari has taught me how to think, plan, and communicate like a scientist, and I will always be grateful for this aspect of his mentorship. Even more so, I will be grateful for his showing

me what it means to be a good mentor: to value your trainees as people; to share your passion for your science and trust that it will inspire your audience; to be a transparent, honest, and generous collaborator; and to shape a lab culture that reinforces these values. I hope to have my own lab one day, and I know that I will be thinking back to my time in graduate school as I ponder what kind of PI I want to be.

I am so thankful for the other amazing people in the Molofsky Lab, all of whom played an enormous role in shaping the scientist I am today. My lab-mates – and friends – have been a constant source of assistance, entertainment, and inspiration. Thank you to the postdocs, upon whose deep wells of knowledge I constantly drew, including Drs. Dean Merrill, Joanna Balcerek, Julia Nilsson, Marcela Taruselli, Kelly Cautivo, Madelene Dahlgren, and Julia Sbierski-Kind. Thank you to the hard-working lab managers and technicians, without whom nothing in lab would have ever happened, including Peri Matatia, Abram Rodriguez, and Elina Wells. Thank you to my three rotation students, Sophia Nelson, Nikhita Kirthivasan, and Joseph Moreno; in addition to their experimental assistance, they helped me realize that teaching is one of my favorite parts of science. I am especially thankful to have gone through graduate school alongside three other incredible graduate students. Sofia Caryotakis is one of the hardest working people I have ever met, whether during a long harvest day or a long hike through mountain lion-infested woods. Anthony Chang, who made me laugh at work more than anyone else, has shown me how to be a deep thinker in and outside of lab. Nick Mroz was my rotation mentor (a job that lasted well past the end of my rotation), my “lab dad”, and one of my closest friends. Nick taught me absolutely every scientific skill I have today, from pipetting, analyzing flow data, and organizing experimental records to dealing with professional

rejections and placing my self-worth outside of my work. I have never admired anyone more for their perseverance and scientific rigor; I am lucky to have known Nick, and I am sure that he will be answering my questions for many decades to come. Together, we four graduate students shared failures, successes, and the many moments in between. I will always remember these moments as the best parts of graduate school.

I would like to thank the many scientists outside of the Molofsky lab who made my PhD possible. Dr. Tom Arnold, my co-mentor, was an amazing collaborator throughout graduate school. His enthusiasm for science rivaled Ari's, and his ideas, reagents, and unending generosity enabled much of my thesis work. I am also grateful for the constant assistance provided by the members of Tom's lab, including Dr. Gabriel McKinsey, Dr. Carlos Lizama-Valenzuela, Remy Pennington, Aditya Katewa, and Helen Lee. Thank you to Amara Larpthaveesarp, whose work with the tMCAO stroke model was essential for my project, for sharing far more time and effort than she must have envisioned when I first asked for her help. I am thankful for my many other collaborators at UCSF: Dr. Manish Aghi and Saket Jain, who helped with our GBM analysis; Dr. Fernando Gonzalez, who provided insight into our tMCAO data; Dr. Jeanne Paz and Dr. Agnieszka Ciesielska, who helped with TBI experiments; Dr. Tatsuya Tsukui, whose fibroblast tools proved invaluable; and Dr. Anna Molofsky, who was an enormously helpful source of advice and a sounding board for pitches, figures, and drafts. I am thankful for all the scientists working on HSW12 who helped me in innumerable direct and indirect ways over four years of feedback and inspiration at floor meetings, technical assistance with experiments, and morale boosting happy hours. I am also grateful to collaborators whom I never met in person, but whose hard work I admired from afar and who taught me that science is at its

best when it is a collaborative endeavor: Dr. Leon Teo and Dr. James Bourne from Monash University, Dr. Helena Paidassi from INSERM, and Dr. Richard Daneman, Lucija Pintarić, and Dr. Nicole Lummis from UCSD.

I would like to thank the remaining members of my thesis committee. Dr. Tien Peng, an expert in stromal biology, was a valuable source of insight into – and tools to explore – the world of fibroblast biology. Dr. Adrian Erlebacher became a mentor figure the moment he told me, during my interview at UCSF, that he had also moved from the east coast and that he was happy to talk about that difficult decision if I wanted to. I came to UCSF determined to rotate in Dr. Erlebacher's lab, and it was during this rotation that I discovered my love for tissue immunology. He has been a wonderful collaborator and mentor ever since. Dr. Dean Sheppard deserves special thanks for going above and beyond regarding my scientific and professional mentorship. Beginning with his asking to meet to discuss my qualifying exam proposal, Dr. Sheppard has become one of my most consistent sources of guidance pertaining both to my project and to my path through MD/PhD training. He is also a model of the scientific generosity that is so prevalent at UCSF. Collectively, this group of scientists made my passage through graduate school immeasurably smoother than it could have been, for which I am immensely grateful.

I am so thankful for my support system outside of lab. My MSTP friends Ricky Guajardo and Lakyn Mayo have been there since the first day of medical school, and I could not have gotten through the last half decade without them. Thank you to my graduate cohort friends Kevin Chen and Kaylee Wedderburn-Pugh – also in my MSTP cohort – along with Meagan Olive, Tori Tran, and Kyla Foster (the "Boy Tacos"). Commiserating over games of darts and tootsie rolls made even the worst parts of

graduate school enjoyable, and I am so glad to have all become friends. Thank you to my parents, who are so invested in my PhD that they always ask me to re-explain my research in progressively simpler terms, even though the explanations never stick. You have always encouraged me to follow my dreams, and while your love and support have been so explicit (and implicit) that the alternative is impossible to imagine, I know that I would not be here today without you, and I do not take it for granted. I'm sorry that I had to move so far away for this part of my life; I hope (and I know) that I have made you proud. Lastly, thank you to my family who has been with me the whole time: my partner and fiancée, Chloe Prendergast. Over the last seven (and counting) years, we have moved across the country together; started graduate school together; cooked, worked, and laughed together; and built a life together (along with our cat, Willow, whose adorableness very much got in the way of my graduate work). You have been my rock: the only person in whom I can confide my deepest insecurities, and the only person I want to tell when an experiment works. I am constantly amazed by your intelligence, creativity, and dedication to your own research and learning. You inspire me every day to be the best version of myself, as a scientist, a friend, and a citizen of the world. I could not have done any of this without you; I can't wait to do the rest of it with you.

AUTHOR CONTRIBUTIONS

Chapter 1 was written by Nathan A. Ewing-Crystal.

Chapter 2 was written by the following authors:

Nathan A. Ewing-Crystal, Nicholas M. Mroz, Anthony A. Chang, Eric Dean Merrill, Sofia E. Caryotakis, Amara Larpthaveesarp, Nikhita Kirthivasan, Leon Teo, Tatsuya Tsukui, Aditya Katewa, Remy Pennington, Gabriel L. McKinsey, Sophia C K Nelson, Agnieszka Ciesielska, Nicole C Lummis, Lucija Pintarić, Madelene W. Dahlgren, Helena Paidassi, Saket Jain, Manish K. Aghi, James A. Bourne, Jeanne T. Paz, Richard Daneman, Fernando F. Gonzalez, Dean Sheppard, Anna V. Molofsky, Thomas D. Arnold*, and Ari B. Molofsky*.

*co-corresponding authors

This chapter, along with the dissertation abstract, is reprinted as a part of manuscript in preparation for submission to a peer-reviewed journal.

Conceptualization, NAEC, TDA, AVM, ABM; methodology, NAEC, NMM, SN, DS, TDA, ABM; investigation, NAEC, NMM, AAC, EDM, SEC, AL, NK, LT, TT, AK, RP, GLM, SCKN, AC, NCL, LP, MWD, HP, SJ, MKA, JAB, JTP, RD, FFG, DS; resources, AVM, TDA, ABM; data curation, NAEC, NM; writing, NAEC, TDA, AVM, and ABM; supervision, TDA, ABM.

Chapter 3 was written by Nathan A. Ewing-Crystal.

DYNAMIC FIBROBLAST-IMMUNE INTERACTIONS SHAPE WOUND HEALING AFTER BRAIN INJURY

NATHAN A. EWING-CRYSTAL

ABSTRACT

Fibroblasts and immune cells coordinate tissue regeneration and necessary scarring after injury. In the brain, fibroblasts are border-enriched cells whose dynamic molecular states and immune interactions after injury remain unclear. Here we define the shared fibroblast-immune response to sterile brain injury. Early profibrotic myofibroblasts developed from pre-existing brain fibroblasts and infiltrated brain lesions, orchestrated by fibroblast TGFβ signaling, pro-fibrotic macrophages and microglia, and perilesional glia. Myofibroblasts transitioned into several late fibroblast states including lymphocyte interactive fibroblasts. Interruption of the early myofibroblast state exacerbated sub-acute brain injury, tissue loss, and secondary neuroinflammation, with increased mortality in the tMCAO stroke model. Disruption of late lymphocyte-fibroblast niches via selective loss of fibroblast chemokine CXCL12 led to late brain-specific innate inflammation and lymphocyte dispersal with elevated IFNγ production. These data indicate the response to brain injury is coordinated by evolving temporal and spatial fibroblast states that limit functional tissue loss and chronic neuroinflammation.

TABLE OF CONTENTS

CHAPTER 1: INTRODUCTION 1

1.1 Overview 1

1.2 CNS injuries: unmet clinical needs 2

1.3 CNS wound healing 2

1.4 Fibroblasts: peripheral states and functions 3

1.5 CNS fibroblasts: homeostasis and injury 5

1.6 Macrophages: periphery and CNS 7

1.7 Macrophages in injury and fibrosis 8

1.8 Lymphocyte response to CNS injury 10

1.9 Summary 12

CHAPTER 2: DYNAMIC FIBROBLAST-IMMUNE INTERACTIONS SHAPE WOUND HEALING AFTER BRAIN INJURY 13

2.1 Results 13

2.1.1 Identification of a dynamic and persistent fibroblast response to brain injury. 13

2.1.2 Myofibroblasts spatiotemporally correlate with lesional profibrotic macrophages and disease-associated microglia. 16

2.1.3 Distinct late fibroblast states include lymphocyte interactive fibroblasts associated with T cell accumulation and persistence. 20

2.1.4 Brain lesional myofibroblasts are coordinated by TGFβ signaling, pro-fibrotic myeloid cells, and perilesional glia to drive wound healing and limit chronic inflammation. 23

2.1.5 Discrete beneficial functions of early myofibroblasts and late lymphocyte interactive fibroblasts. 28

2.2 Discussion 30

2.3 Figures 34

2.4 Supplemental files 64

2.4.1 Supplementary Video 1 64

2.4.2 Supplementary Video 2 64

2.4.3 Supplementary Video 3 64

2.5 Materials and methods 65

2.6 Manuscript information 93

CHAPTER 3: CLOSING AND FUTURE DIRECTIONS 95

REFERENCES 98

LIST OF FIGURES

Figure 1. Identification of a dynamic and persistent fibroblast response to brain injury....34

Figure 2. Additional characterization of the CNS fibroblast response to PT injury……..…36

Figure 3. Spatial transcriptomics characterization of PT injury……...38

Figure 4. Myofibroblasts spatiotemporally correlate with lesional profibrotic macrophages and disease-associated microglia ……..……39

Figure 5. Additional transcriptomic characterization of fibroblasts across species and injury models…….....……...41

Figure 6. Additional *in vivo* validation of early TGFβ-associated myofibroblasts……...43

Figure 7. Additional characterization of injury-responsive profibrotic CNS Myeloid cells…….…….……...45

Figure 8. Distinct late fibroblast states include lymphocyte interactive fibroblasts associated with T cell accumulation and persistence…….…….…….……47

Figure 9. Additional characterization of late lesional fibroblasts……..49

Figure 10. Brain lesional myofibroblasts are coordinated by TGFβ signaling, pro-fibrotic myeloid cells, and perilesional glia to drive wound healing and limit chronic inflammation……..……...51

Figure 11. Profibrotic macrophages promote CNS fibroblast expansion……...53

Figure 12. TGFβ drives CNS wound healing and resolution of inflammation…….55

Figure 13. Additional molecular characterization of injury response after fibroblast impairment……...…..…....57

Figure 14. Discrete beneficial functions of early myofibroblasts and late lymphocyte interactive fibroblasts…….……...59

Figure 15. Additional characterization of *Tgfbr2* and *Cxcl12* cKO mice……..60

Figure 16. Graphical Summary……..……..61

Figure. 17: Representative flow cytometry gating…….62

LIST OF ABBREVIATIONS

CNS: Central Nervous System

TBI: Traumatic Brain Injury

SCI: Spinal Cord Injury

GBM: Glioblastoma Multiforme

EAE: Experimental Autoimmune Encephalomyelitis

PT: Photothrombotic

CCI: Controlled Cortical Impact

DAMP: Damage Associated Molecular Pattern

SAM: Scar Associated Macrophage

DAM: Damage/Disease Associated Microglia

BAM: Border Associated Macrophage

CSF: Cerebrospinal Fluid

TRM: Tissue Resident Memory T cell

CHAPTER 1: INTRODUCTION

1.1 Overview

Brain injury results in spatiotemporally stereotyped wound healing and immune responses that collectively facilitate organ regeneration. Central nervous system (CNS) fibroblasts – rare under homeostatic conditions – have only recently been appreciated as participants in CNS remodeling after injury. Understanding how CNS fibroblasts and their dynamic states coordinate wound healing and immune responses to injury is crucial to developing effective therapies for CNS injuries and their many sequelae. The aims of this thesis are as follows:

1. Characterize the molecular and spatiotemporal fibroblast response to CNS injury.
2. Define molecular mechanisms driving injury-induced fibroblast responses.
3. Identify functional roles for fibroblast subset(s) after injury.

1.2 CNS injuries: unmet clinical needs

Injuries to the central nervous system (CNS) are leading causes of death and disability worldwide[1–3], owing to the adult brain and spinal cord's limited capacity for regeneration, the high prevalence and severity of chronic sequelae, and a lack of effective treatment options. CNS injuries are broadly categorized into 1) stroke (disruption of CNS blood flow, with ischemic and hemorrhagic subtypes), 2) traumatic brain injury (TBI, including severe head injuries/concussions and mild/chronic injuries), and 3) spinal cord injury (SCI). Additionally, though not "injuries", brain cancers including glioblastoma multiforme (GBM) bear molecular resemblance to CNS injury and regenerative responses[4,5], consistent with characterizations of cancers as "wounds that never heal"[6]. CNS injuries lead to chronic cognitive and functional impairments[7–10] and increase the risk of seizures[11] and neurodegenerative diseases including Alzheimer's Disease[12,13], reflecting shared elements of underlying pathology[12]. Treatments for these CNS diseases aim to limit early damage and loss of neuronal function but do not directly enhance subacute and chronic reparative processes. For example, stroke treatment involves clot-dissolving agents and is contraindicated after hyper-acute injury due to the risk of hemorrhage[14,15]. Similarly, effective treatments for TBI[3], Alzheimer's Disease[16], and GBM[17] are key unmet needs, reflecting a critical gap in our mechanistic understanding of the cells and signals that dictate CNS healing[18–20].

1.3 CNS wound healing

Organ remodeling after injury includes walling off core necrotic regions that are not salvageable while preserving the penumbra of potentially viable tissue. In the CNS, extensive work over the last century has focused on gliosis, a wound-healing process

largely involving astrocytes (“astrogliosis”), a type of brain-resident stromal cell. Astrocytes are an abundant brain cell type, with homeostatic roles in maintaining blood-brain barrier integrity, promoting synapse function and homeostasis, and providing metabolic support and protection to neurons[21]. After CNS injury (and across CNS pathology more broadly), astrocytes acquire a “reactive” phenotype involving upregulation of specific reactive genes, most notably GFAP; these reactive astrocytes hypertrophy, proliferate, migrate to lesion borders, and attempt to reform the glia limitans of the blood brain barrier. The resulting glial scar is required for neuroprotection from excitotoxic molecules, oxidative stress, metabolic damage, edema, inflammatory cells and cytokines, and infectious microbes, though excessive astrogliosis can also inhibit neuronal axon regeneration[21]. Despite the critical importance of effective tissue-level wound healing in functional recovery from CNS injury, over a century of research has been unable to produce a safe and effective treatment aimed at modulating (facilitating, preventing, or “fine-tuning”) astrogliosis. However, in recent decades, it has become clear that additional stromal cells subsets – including fibroblasts – are also involved in CNS remodeling after injury[22–31] and in CNS pathology more broadly[32–39], revealing a critical knowledge gap in our conventional understanding of CNS wound healing.

1.4 Fibroblasts: peripheral states and functions

Stromal cells are present in virtually all organs and include fibroblasts and mural cells (vascular smooth muscle cells and pericytes, lining large and small vessels, respectively). Fibroblasts are best known for secreting and remodeling extracellular matrix (ECM) to maintain tissue structure. However, fibroblasts are particularly versatile cells that play diverse roles in organ homeostasis, with emerging single cell

transcriptomics identifying both tissue-restricted states[40] and cross-organ conserved states, including a universal fibroblast state with elevated mesenchymal progenitor capacity[41]. These universal fibroblasts are enriched around natural tissue borders such as larger vessels, fascial planes, and organ surfaces, including the meningeal linings of the brain[42,43]. Additional fibroblast subsets regulate immune homeostasis and inflammation[33,36,38,43–55], including via the coordination of lymphocyte expansion, activation, and cytokine production at tissue borders during immune challenges[42,56,57]. Myofibroblasts, an alternate pro-fibrotic fibroblast state, emerge with tissue injury, produce abundant ECM, and drive wound contraction[6,58]. Typically transitory, myofibroblasts can chronically expand in disease to promote tissue scarring, fibrosis, and resistance to cancer immunotherapy[40,59], often reinforced by macrophage subsets and high bioavailability of the cytokine TGFβ[60–62]. Myofibroblasts can arise from multiple stromal cell sources, including universal fibroblasts[40], tissue-specific parenchymal fibroblasts[63], and vasculature-associated mural cells (e.g., pericytes, smooth muscle cells)[64].

Fibroblasts also display substantial plasticity, transitioning between discrete states in response to changing pathological and micro-environmental context. After skin wounding, acute inflammation-associated fibroblasts give way to subacute myofibroblasts in a spatiotemporally coordinated progression[6], although late stages were not directly examined. In lung fibrosis, alveolar fibroblasts pass through a chemokine-producing inflammatory state before acquiring a profibrotic *Cthrc1*-lineage$^+$ myofibroblast identity[63]. Finally, universal/adventitial fibroblasts can give rise to tissue- and perturbation-specific signatures, including myofibroblasts that suppress tumor-directed immune

responses[40,59]. However, while extensive research has documented the versatility and plasticity of peripheral fibroblast states and their diverse roles in homeostasis and pathology, how these states map onto CNS fibroblast populations is not understood.

1.5 CNS fibroblasts: homeostasis and injury

The CNS, well known for its relative immune privilege, has also long been considered a “fibro-privileged” organ, owing to the common conception that the presence of fibroblasts (and their potential for driving fibrotic responses) poses an intolerable risk to functional brain parenchyma. Indeed, unlike most other organs, the brain lacks *bona fide* parenchymal fibroblasts. Instead, CNS fibroblasts are restricted to CNS borders, including the covering meninges, CSF-producing choroid plexus, and perivascular spaces around larger vessels[65–67]. Though relatively rare, border-associated CNS fibroblasts are implicated in maintaining meningeal structure[66], promoting immune surveillance[68], and regulating CSF/interstitial fluid exchange[69,70]. Additionally, recent studies have begun to identify substantial transcriptional fibroblast heterogeneity among and within these microanatomic niches[34,53,68,71–75], hinting at additional – though as yet unappreciated – functional diversity.

Recent studies have also identified potential roles for CNS fibroblasts after injury, contrary to longstanding notions that astrocytes are the primary cell type involved in CNS remodeling after injury. Non-glial stromal cells – potentially including fibroblasts – have been implicated in CNS pathologies including human SCI, stroke, multiple sclerosis, and glioblastoma[28,29], and in mouse models of SCI[23–25,31], intracerebral hemorrhage[30], TBI[22], stroke[26–28], and diverse infectious, inflammatory, and malignant CNS pathologies[32,35,36,38]. Initial reports across several CNS pathologies described these cells as pericytes[24,25,28,29],

though often based on markers shared by fibroblasts[25,74]. Other more recent studies have argued for a fibroblast origin based on a lack of pericyte markers[25,31] or lineage tracing[30,38], with contemporary investigations concluding that ontogeny (cellular/developmental origin) likely depends on microanatomical context and specific pathology[75,76].

While fibroblast ontogeny remains controversial, the molecular states and functional importance of these cells is even less well appreciated. Beyond the identification of a proliferative myofibroblast state in Experimental Autoimmune Encephalomyelitis (EAE, a model for Multiple Sclerosis)[38] and SCI[76,77], the heterogeneity of CNS fibroblast states – and the potential for plasticity and state transitions – is poorly understood. Similarly, the functional importance of this response is only beginning to be appreciated. Early experiments aimed at stromal cell ablation found that while global stromal cell ablation prevented tissue regeneration after spinal cord injury, a mild reduction (i.e., inefficient ablation) actually enhanced axonal and tissue regeneration[24,25]. In EAE, fibroblasts – and fibrosis – impair oligodendrocyte migration and exacerbate pathology[38]. However, in a model of intracerebral hemorrhage, fibroblast ablation prevented blood brain barrier repair and impaired neurological recovery. Thus, contrary to popular notions that fibrosis (like excessive gliosis) would be *necessarily* maladaptive in the CNS, emerging work suggests that stromal cells, including fibroblasts, play diverse and context-dependent roles to promote – or impair – wound healing. While this seemingly critical response is a tempting therapeutic target, a full understanding of the fibroblast states and molecular mechanisms underlying this complex biology is an essential prerequisite to any attempt to fine-tune fibroblast functions after CNS injury.

1.6 Macrophages: periphery and CNS

Macrophages are phagocytic innate immune cells that are abundant within all organs and play diverse roles in health and disease. Broadly, macrophages consume any foreign or unwanted components of the tissues in which they reside while also helping coordinate the resulting immune response(s)[78]. Macrophages can sense and shape their tissue microenvironments via the expression of a broad swathe of pattern recognition receptors (including pathogen-associated and damage-associated molecular patterns), chemokine receptors, and cytokine receptors, along with numerous pro- and anti-inflammatory chemokines. Thus, macrophage identities and functions are informed by their tissue of residence and their positioning within said tissue.

In the brain, microglia are the dominant macrophage subset (and are the only resident parenchymal immune cell of the naïve brain). Derived initially from the yolk sac, microglia are long-lived cells that play numerous roles in brain development and homeostasis. Microglia regulate neuronal population sizes via phagocytic clearance of precursor cells or neuronal processes during development[79], and they subsequently coordinate synaptic and neuronal health during adulthood via phagocytosis of synapses[80] and remodeling of ECM[81,82]. However, microglia are largely restrained/less active at rest, potentially explaining observations that their removal from the brain does not dramatically impact organismal health[83]. Accordingly, one of the dominant roles of microglia is that of a sentinel, capable of sensing infection, inflammation, or damage, rapidly activating, and coordinating downstream immune responses, as discussed below. While rarer than microglia, non-microglial macrophages in the perivascular, leptomeningeal, and periventricular/choroid plexus-associated spaces – collectively referred to as “border-

associated macrophages" (BAMs) – are another yolk sac-derived macrophage subset with recently appreciated roles in health and disease[84,85]. Specifically, these macrophages regulate the flow of CSF[86] while monitoring its contents for relevant antigens[84]. Similarly to microglia, they can become activated in disease states and may play important roles in subsequent neuroinflammatory processes. Finally, monocytes can differentiate into macrophages in peripheral tissues – a process that is uncommon in the homeostatic brain, at least in rodents, but becomes relevant after injury.

1.7 Macrophages in injury and fibrosis

In conjunction with a wound-healing response, CNS injury induces a robust and dynamic immune response involving all the above subsets. Thrombosis and ischemia initiate a number of thrombo-inflammatory processes, including activation of the complement cascade and upregulation of endothelial selectins, collectively initiating the recruitment of numerous immune cell subsets[87]. Simultaneously, microglia – through recognition of Damage Associated Molecular Patterns (DAMPs), early innate cytokines, and complement – become activated, showing typical changes such as de-arborization and ameboid transformation[2,87]. In the early phases of the CNS injury immune responses, microglia are the dominant reactive immune cell, phagocytosing dead cells and debris to limit the extent of injury and producing chemokines and cytokines to coordinate other arms of the immune response[87,88]. Other macrophage subsets including BAMs and monocyte-derived cells are rapidly activated and/or recruited (e.g., via the CCL2-CCR2 axis), often responding either to DAMPs or to chemokines/cytokines released by microglia. Once within the injured or perilesional brain parenchyma, these populations engage in further phagocytosis/inflammatory signaling. The ontogenic and micro-

anatomical origin of each myeloid cell response, as well as its pathologic context, may contribute to said cell-type's ultimate phenotype and function, with a resultant diversity of dynamic and interconnected myeloid programs that collectively shape functional recovery[89–92]. Nevertheless, there may also be some phenotypic and transcriptional convergence of these responses, likely driven by niche signals. For example, monocytes entering the brain downregulate circulating monocyte markers and acquire a macrophage-like – or microglia-like – identity, which may persist for months[93]. Similarly, across distinct pathologies including neurodegeneration, stroke, and TBI, microglia acquire a conserved transcriptional identity known as Disease Associated Microglia (DAM)[94,95].

Relatedly, macrophage subsets may converge on disease-relevant phenotypes in peripheral pathology, specifically including tissue fibrosis. It has long been appreciated that fibroblasts and macrophages engage in reciprocal interactions under homeostatic conditions[78,96]. More recently, transcriptional profiling of macrophages across fibrotic disease has revealed a specific macrophage "state" associated with myofibroblasts, tissue injury, and tissue fibrosis (Scar Associated Macrophages, SAMs[62]). While some controversy remains as to whether the SAM state is profibrotic itself or merely associated with fibrotic contexts[97], macrophages are well-characterized contributors to fibrosis across numerous disease states[98,99]. This profibrotic role often depends in part on the production of TGFβ[100–104], with macrophages producing an initial dose of TGFβ that can activate self-sustaining pro-fibrotic feedback loops among distinct cell types including fibroblasts. Similar profibrotic roles, maladaptive in fibrotic disease, are beneficial in the context of wound healing, where evolving macrophage-fibroblast interactions are required

for appropriate tissue remodeling[6]. However, the extent to which the complex myeloid response to CNS injury intersects with the emerging stromal/fibroblast response to injury remains unknown.

1.8 Lymphocyte response to CNS injury

Later stages of the immune response to CNS injury are dominated by lymphocytes, particularly T cells. T lymphocytes, effectors of the adaptive arm of the immune system, are activated by their cognate antigens to exert effector functions including cellular killing and cytokine release. Naïve T cells and some memory T cell subsets traffic through peripheral tissues and surveil for antigens; similarly, most peripheral organs contain populations of tissue-resident memory T cells (TRM), which develop after immune responses, associate with tissue niches enabling long-term maintenance, and rapidly initiate immune responses upon reinfection[105]. In contrast, the brain contains very few naïve and circulating memory T cells and only small populations of TRM[106], contributing to the long-standing notion that the brain is an immune-privileged organ[107]. Notably, the meninges contain numerous homeostatic lymphocytes, including T cells, which surveil cerebrospinal fluid (CSF)[68] and produce cytokines that can affect brain physiology and behavior[106,108–110]. Nevertheless, T cells are unable to enter into brain parenchyma via the perivascular space without antigen-induced activation[66].

CNS injury enables T cell infiltration into the brain parenchyma, in part by enabling the systemic spread of CNS autoantigens[111,112] and inducing changes in cerebral vasculature (e.g., adhesion molecule expression and tight junction permeability)[113]. T cell infiltration begins within hours after injury, peaks at subacute timepoints, and can persist for weeks[18,88]; early T cell infiltration is largely antigen-independent, while subsequent

accumulation may represent antigen-dependent clonal expansion[111]. The functions of CNS injury-induced lymphocytes are variable and likely context-dependent. For example, animal studies have shown that early T cell responses to ischemic stroke are detrimental: T cell-deficient mice show smaller lesions and better functional recovery after stroke[111,114], though pathology may depend on the specific antigen recognized. Conversely, regulatory T cells (Tregs) promote functional recovery from injury[115,116]; T cells *inversely* correlate with lesion size during chronic phases of stroke[117]; and autoreactive T cells promote recovery after SCI[112].

Finally, most research on T cells after CNS injury has focused on early timepoints (e.g., within days of injury). Persistent T cells have been observed weeks to months after CNS injury[18,118]; however, it remains unclear whether these cells resemble the brain TRM observed after viral and parasitic infections[119–124], what tissue niches maintain these long-lasting populations, and what function(s) these lymphocytes may be playing. One relevant function likely involves effector cytokine production and signaling to brain parenchymal cells; indeed, T cell-derived cytokines can regulate neuronal inhibitory balance, memory, and social behavior at rest[106,108–110] or after CNS infection[125]. Our own group recently identified a role for IFNγ-producing T cells in reducing seizure susceptibility after TBI[118], consistent with observations that IFNγ promotes tonic GABA signaling[109]. T cell immunity has also recently been implicated in neurodegeneration[126–128], another common chronic sequela of CNS injury[87]. Thus, a full understanding of late, persistent CNS T cell responses will be essential to design effective interventions targeting chronic stages of CNS injury and healing.

1.9 Summary

CNS injuries, including stroke, TBI, and SCI, currently lack effective interventions. Injury induces a wound-healing response involving glial cells such as astrocytes but also stromal cells, including fibroblasts. Simultaneously, injury induces an immune response consisting of an early wave of myeloid cells, including reactive microglia and recruited peripheral monocyte-derived macrophages, and a later wave of adaptive immune cells including T lymphocytes. These wound healing and immune responses are complex and interconnected, likely involving macrophage-fibroblast and fibroblast-lymphocyte interactions, and evolving, with multiple cell-types passing through distinct, context-dependent states. Collectively, they dictate tissue repair and functional recovery. In this thesis, I investigate how brain fibroblast states and their local immune partners sculpt the injured, healing, and remodeled brain.

CHAPTER 2: DYNAMIC FIBROBLAST-IMMUNE INTERACTIONS SHAPE WOUND HEALING AFTER BRAIN INJURY

2.1 Results

2.1.1 Identification of a dynamic and persistent fibroblast response to brain injury.

To establish the microanatomic positioning, or *topography*, of brain fibroblasts after injury, we used Collagen 1 lineage tracing to specifically and indelibly track fibroblasts in mice ($Col1a2^{CreER}$; $R26^{TdT}$). In the uninjured brain, fibroblasts were absent from the neuron- and glia-rich parenchyma and instead localized to CNS borders, including larger perivascular, meningeal, periventricular, and choroid plexus regions, as previously shown[39,66] (**Fig. 1a, Fig. 2a**). In a sterile brain injury model involving focal cortical ischemia (photothrombotic/PT injury), fibroblasts expanded into damaged brain regions, produced Collagen 1 and other ECM components, and formed a lesion distinct from parenchymal astrocytic gliosis by 14 days post-injury (dpi) (**Fig. 1b**). In models of traumatic brain injury (controlled cortical impact, CCI) or ischemic stroke with focal ischemia-reperfusion injury (transient middle cerebral artery occlusion, tMCAO), similar brain fibroblast infiltration was observed (**Fig. 1c,d, Fig. 2b,c**). In a non-human primate cortical stroke model, peri-lesional fibrosis ($COL6^{+}$) was detected at 7dpi and persisted for at least one year post-injury (**Fig. 1e**). Focusing on the spatiotemporally reproducible PT cortical injury model, we next defined the kinetics of fibroblast expansion using multiple fibroblast reporter lines. Fibroblast infiltration was gradual: fibroblasts were first detected near the leptomeningeal–wound border by 4dpi, expanded by 7dpi, surrounded and infiltrated the contracting lesion by 14-21dpi, and persisted for at least one-year post injury (**Fig. 1f,g,**

Fig. 2d, Supplementary Video 1). Nuclear flow cytometry, which optimized lesional cell recovery, revealed that fibroblasts were ~40% of all lesional nuclei at 14dpi, a frequency comparable to the resting dural meninges (**Fig. 2e,f**). Fibroblasts were present at lesional borders and closely associated with regions of intralesional vascular remodeling (**Fig. 2g,h, Supplementary Video 2**). These findings reveal a pattern of injury-driven brain fibroblast infiltration that is coordinated, long-lasting, and conserved across several models of brain injury.

Next, we characterized the cellular origin of brain lesional fibroblasts, which could derive from pre-existing brain fibroblasts subset(s) and/or perivascular mural cells (i.e., pericytes or smooth muscle cells). We used reporter mice for *Col1* expression to simultaneously track current and prior fibroblast identity ($Col1a1^{GFP}$ with $Col1a2^{creER}$; $Rosa26^{TdT}$, respectively)[65]. $Col1a2^{creER}$ recombination was >95% specific for current brain fibroblasts ($Col1a1^{GFP+}$) with a ~50% sensitivity (TdT^+ recombination frequency) in both resting fibroblasts and PT lesional fibroblasts at 21dpi (GFP^+) that were recombined prior to injury, consistent with a predominantly fibroblast origin (**Fig. 2i-l**). As expected, lesional fibroblasts expressed canonical fibroblast markers (e.g., Dcn, Col6a1, Postn, Gli1-lineage$^+$), whereas expression of mural cell markers was sparse (**Fig. 2m,n**). Lineage tracing of pericytes using the $Ng2^{creER}$ allele (which also marks oligodendrocyte-lineage cells), or vascular smooth muscle using $Acta2^{creER}$, revealed minimal detected contributions of these mural cell lineages to PT lesional fibroblasts (**Fig. 2o-s**), although *Ng2*-lineage$^+$ cells accumulated within the neighboring glial scar**.** Similar results were observed in the distal middle cerebral artery occlusion (dMCAO) model of stroke: lineage-traced fibroblasts ($Col1a2^{creER}$) infiltrated and expanded within fibrotic lesions, whereas

lineage-traced pericytes (Atp13a5^{creER}) did not detectably expand within the lesion (**Fig. 2t,u**). To determine whether the precursor fibroblasts that gave rise to lesional fibroblasts resided in the dural meninges, we applied 4-OHT to the intact cranium of *Col1a2* lineage tracer mice immediately prior to PT injury, inducing sparse recombination in cranial-associated dural fibroblasts but not penetrating to recombine in leptomeningeal or perivascular fibroblasts (**Fig. 2v-z**). After PT injury, fibroblast recombination in lesions was similar to levels detected in the dural meninges (8-10%) TdT^{+}, **Fig. 2aa,ab**), suggesting minimal contributions to the PT lesion fibroblast pool from unlabeled stromal cell sources that could dilute this frequency. These data suggest a fibroblast cellular source within the outer meninges for most PT lesional fibroblasts; however, the ontogeny and micro-anatomical origin of injury-associated fibroblasts likely depend on the CNS injury site and type[76], similar to the diverse ontogenies of injury-driven myofibroblasts in peripheral organs[129,130].

To define brain fibroblast dynamic positioning after PT injury, we first performed spatial transcriptomics across rest and injury time points, herein called acute, subacute, and chronic phases of brain injury and repair (2dpi, 7dpi, 21dpi; **Fig. 1h**). Dimensionality reduction revealed 23 spot-based spatial clusters (**Fig. 1i**, **Fig. 3a,b**), with one cluster further subclustered (**Fig. 1i,** c10). We identified four major fibroblast-containing spatial clusters (*Col1a1*-enriched) with distinct temporal, molecular, and microanatomical patterns (**Fig. 1j,k, Fig. 3c,d**). Two spatial clusters that were both fibroblast-enriched and injury-associated were an early-fibroblast-enriched cluster transiently abundant at 7dpi in perilesional regions (c10.0; **Fig. 1l,** red), and a late-fibroblast-enriched cluster abundant at 21dpi in the lesion core (c8; **Fig. 1l,** blue). We also identified a fibroblast-enriched brain

border cluster (c3; **Fig. 1i,** brown) and a fibroblast- and glial-enriched late lesion-brain interface cluster (c13; **Fig 1i**, cyan; **Fig. 3e-g**). Next, we compared differentially expressed genes between the early- and late-fibroblast-enriched clusters (c10.0, red, and c8, blue; **Fig. 1m**). The early-fibroblast signature included genes implicated in pro-fibrotic processes and certain macrophage-related chemokines/growth factors[40,60]. In contrast, the late-fibroblast signature was enriched for ECM molecules and adaptive immune-associated genes.

We noted that many "early fibroblast-enriched" cluster upregulated genes were well-described targets of TGFβ signaling, including *Cthrc1, Lrrc15,* and *Postn*[40,60]. TGFβ is a pleiotropic cytokine with intersecting roles in organ physiology and immunity and is particularly critical to driving pro-fibrotic ECM-depositing fibroblasts that often express αSMA, here called myofibroblasts[100]. We developed a myofibroblast-associated TGFβ score, representing genes elevated in primary lung fibroblasts treated with high TGFβ, and found this score was correlated with the early-fibroblast spatial signature (**Fig. 1n, Fig. 3h**). The early fibroblast signature was also enriched for proliferation-related genes (e.g., *Mki67*), a canonical feature of pro-fibrotic fibroblasts[100] (**Fig. 1o, Fig. 3i**). These data suggest a dynamic PT lesional fibroblast response, with a subacute TGFβ-associated myofibroblast state followed by distinct chronic fibroblast state(s).

2.1.2 Myofibroblasts spatiotemporally correlate with lesional profibrotic macrophages and disease-associated microglia.

To define brain injury-associated fibroblasts at a cellular resolution, we next performed single nuclear RNA sequencing (snRNAseq) of the PT lesional and perilesional

cortex across the injury time course, including control uninjured cortex and cranial meninges samples, with a final library of 28,187 nuclei (**Fig. 4a, Fig. 5a**). Unsupervised clustering identified brain cell types such as neurons, astrocytes, oligodendrocytes, endothelial, immune, and stromal cells (**Fig. 5b-f**). Stromal cell sub-clustering (involving 8,096 fibroblasts and 189 mural cells) identified 7 PT lesion-enriched fibroblast clusters, 5 fibroblast clusters mapping to the resting cranial meninges, and 1 mural cell cluster (**Fig. 4b,c, Fig. 5g**). PT lesional fibroblast states evolved across the injury timespan, mirroring findings suggested by spatial sequencing (**Fig. 4d, Fig. 5h**). Myofibroblast and proliferative myofibroblast states dominated subacute time points (7dpi). Myofibroblasts expressed canonical markers such as *Cthrc1, Acta2, Lrrc15, Postn, Fn1, Tgfbi,* and *Dcn*, with enrichment for programs associated with ECM organization and connective tissue/cartilage development (**Fig. 4e,f**). *Tgfb1* was identified as the ligand most likely to drive the myofibroblast state (**Fig. 4g**). Similarly, in a stroke model performed in non-human primates, we also identified discrete populations of brain fibroblasts[131] (**Fig. 5i,j**), with subacute injury-associated fibroblast clusters (7dpi) showing higher expression of myofibroblast genes and a myofibroblast-associated transcriptomic score (**Fig. 5k-n**). Analysis of published scRNAseq data from human patients with TBI[132] (**Fig. 5o-q**) or glioblastoma multiforme (GBM)[35] (**Fig. 5r-w)** also revealed small fibroblast clusters with transcriptomic evidence of a myofibroblast program. These findings are consistent with a conserved cross-species myofibroblast state that emerges in response to diverse brain injuries.

Next, we validated the presence of a myofibroblast response *in vivo.* Using nuclear flow cytometry, we found that 7dpi lesional fibroblasts were enriched for pSMAD3, a

hallmark of active TGFβ signaling (**Fig. 6a,b**). Immunofluorescent microscopy confirmed an early and transient lesional myofibroblast population, as marked by αSMA (**Fig. 6c-e**). We also performed myofibroblast cellular lineage tracing using *Cthrc1*, a gene selectively expressed in pro-fibrotic (myo)fibroblasts experiencing elevated TGFβ-signaling[129] (Cthrc1^{creER}; R26^{TdT}, **Fig. 4h,i**). Continuous C*thrc1*-lineage labeling throughout the PT injury time course revealed widespread fibroblast expression in the lesion and injured dural meninges (**Fig. 4j, Fig. 6f, Supplementary Video 3**). Similar to the resting lung[129], *Cthrc1*-lineage^{+} fibroblasts were sparse in resting meninges and cortex and lineage-tracing experiments indicated they did not give rise to PT lesional fibroblasts (**Fig. 4k, Fig. 6f**). Using timed tamoxifen induction, we found that fibroblast *Cthrc1* expression (TdT) peaked between 0 and 7dpi and was again minimal by 14dpi, though *Cthrc1* lineage-traced lesional fibroblasts persisted for at least one year post injury (**Fig. 4l-n**). Similar myofibroblast kinetics were observed using αSMA lineage tracer mice, which additionally marks expected vascular smooth muscle cells (**Fig. 6g-l**). Proliferation, as tracked via nuclear EdU incorporation, was also elevated in early myofibroblasts (**Fig. 6m,n**), consistent with our transcriptomic data. *Cthrc1*-lineage^{+} fibroblasts were also observed in both the tMCAO and TBI models of brain injury (**Fig. 6o-p**). Together, these data suggest a transient, brain injury-associated myofibroblast state that ultimately wanes, giving rise to discrete and persistent late lesional fibroblast state(s).

Similar to fibroblasts, macrophages are also present across organs, including resident microglia in the CNS; although tissue macrophages adapt to their local organ, they can also adopt cross-organ conserved states that regulate organ damage and fibrotic responses[62,86,99]. Concurrent with the fibroblast response, we observed an injury-

responsive population of myeloid cells (Iba1^{+}) that formed a perilesional ring by 2-7dpi, infiltrated the PT lesion core by 14dpi, and persisted for weeks with spatial proximity to fibroblasts (**Fig. 4o, Fig. 7a,b**). To better map the ontogeny of this myeloid cell response, we tracked myeloid cells deriving from reactive microglia (P2ry12^{creER})[95], infiltrating monocytes (Ccr2^{creER})[91], or border-associated and perivascular macrophages (BAM/PVM; PF4^{cre})[86]. PT lesional contributions were apparent from both resident (*P2ry12*-lineage^{+}) and recruited myeloid cells (*Ccr2*-lineage^{+}). Microglia-derived and monocyte-derived cells spatially diverged by 14dpi – with enrichment in the outer glial scar (GFAP^{+}) and inner lesional core, respectively – but overlapped in the fibroblast-glial border, inhabiting similar regions of subacute fibroblastic ECM (**Fig. 7c-i**). Flow cytometry confirmed that early infiltrating monocytes (*Ccr2*-lineage^{+}) differentiated into both lesional macrophages and dendritic cells (**Fig. 7j,k**). BAM/PVM lineage-derived cells (PF4-*lineage*$^{+}$) were diffusely present across lesional areas and time points (**Fig. 7l-n**).

We also defined injury-associated myeloid cell heterogeneity via snRNAseq; nuclear sub-clustering identified homeostatic microglia, disease-associated microglia (DAM), inflammatory monocytes and dendritic cells, and several macrophage subsets (**Fig. 4p, Fig. 7o-q**). Macrophage subsets were further parsed as (a) BAM/PVM border macrophages[86], (b) macrophages resembling monocyte-derived scar- or lipid-associated macrophages (SAM/LAM), with fibrosis-associated roles in other organs[62], here called SAM, and (c) low abundance “ECM Macrophages”. A profibrotic SAM score[62,97] was enriched in brain SAM and DAM clusters, particularly at 7dpi, and this profibrotic score and the cluster signatures were each enriched in early areas of lesional border fibrosis (**Fig. 4q, Fig. 7r**). FABP5 – a SAM marker – was visualized in close proximity to *Cthrc1*-

lineage^{+} myofibroblasts and co-localized with cells of both microglial and monocytic lineage near lesional borders (**Fig. 7s-u**). Moreover, single-nuclear transcriptomics from non-human primate stroke and human TBI revealed similar SAM score enrichment among myeloid cells (**Fig. 7v,w**).

To investigate potential mechanisms underlying the association between myofibroblasts and the SAM/DAM myeloid state, we performed ligand-receptor analysis, which predicted that SAM/DAM cells could potentially signal to myofibroblasts via diverse signals including *Tgfb1* **(Fig. 4r, Fig. 7x**) and that lesional myofibroblasts could reciprocally influence SAM/DAM via signals such as *Csf1* (M-CSF)[95]. In an *ex vivo* coculture assay, 7dpi PT lesions – enriched in myofibroblasts – promoted increased microglial expression of DAM markers, as compared with 21dpi lesions or microglial monoculture controls (**Fig. 7y**). Collectively, these data suggest a transient profibrotic myeloid cell identity convergence in resident microglia and recruited monocyte-derived macrophages that is spatiotemporally and functionally associated with myofibroblasts, likely reflecting a response to shared environmental cues associated with injuries (e.g., dead cells, debris, lipids, cytokines[62]), and raising the likelihood of bi-directional fibroblast-macrophage “pro-fibrotic” state interactions.

2.1.3 Distinct late fibroblast states include lymphocyte interactive fibroblasts associated with T cell accumulation and persistence.

While the myofibroblast state was predominant at subacute phases of brain injury, distinct fibroblast states were identified at late stages after injury (21dpi, **Fig. 8a**). Altered dural and leptomeningeal (pial-like and arachnoid-like) fibroblasts were identified via

expression of respective meningeal layer markers[75] (**Fig. 8b**). These states, which showed a border distribution at rest, were predicted to reform the meningeal layer between lesion and brain parenchyma (**Fig. 4d, Fig. 8c, Fig. 9a**). Quantitative immunofluorescent microscopy confirmed this predicted topography, with leptomeningeal fibroblasts (Aldh1a2^{+}/Laminin^{+}) directly adjacent to reactive brain astrocytes, and altered dural fibroblasts (Alpl^{+}) present at the lesion-meningeal interfaces (**Fig. 8d,e, Fig. 9b-d**). A “late inner fibroblast” state was enriched in the lesion core (**Fig. 8d,e,** FGF13^{+}), expressing ECM genes but lacking canonical markers of highly active profibrotic myofibroblasts (e.g., *Acta2*, *Cthrc1, Lrrc15*) (**Fig. 4e**). Instead, late inner fibroblasts expressed some markers associated with smooth muscle function (e.g., *Cdh18, Sema3c*), potentially reflecting a fibroblast vascular remodeling state (**Fig. 2g,h, Fig. 9e-i**). Lymphocyte interactive fibroblasts were found in outer lesional border regions and were phylogenetically most similar to dural fibroblasts (**Fig. 8d,e,** CD80^{+}; **Fig. 9j**). Notably, all late fibroblast states were strongly represented amongst *Cthrc1*-lineage^{+} fibroblasts (**Fig. 9k**), suggesting that a majority of brain injury-associated fibroblasts pass through a shared and transient myofibroblast state (*Cthrc1*$^{+}$) before acquiring their discrete late identities and positionings. Immunofluorescent microscopy also identified the presence of all late fibroblast identities after stroke via tMCAO (**Fig. 9l**), indicating potential conservation of fibroblast dynamics – and functions – across brain injury.

The lymphocyte interactive fibroblast cluster was particularly noteworthy, as it was enriched for pathways associated with lymphocyte engagement, including signals that recruit and support lymphocytes and that are particularly associated with immunoregulatory fibroblastic reticular cells (FRC) present in the lymph nodes, spleen,

and tertiary lymphoid tissues (e.g., *Cxcl12, Ccl19, Ccl8, Cxcl16*)[68,133] (**Fig. 8f,g**). Mirroring the emergence of this fibroblast state, T lymphocytes were rare in the uninjured brain and early phases of brain injury but accumulated by 14dpi (**Fig. 8h, Fig. 9m, Fig. 17a**). Lesional T cells were predominantly $CD4^+$ and $CD8^+$ T cells, with a relative enrichment of $CD8^+$ T cells at chronic time points; most $CD4^+$ T cells expressed the transcription factor Tbet (*Tbx21*), consistent with a T helper type 1 (Th1) IFNγ-expressing identity (**Fig. 8i,j, Fig. 9n**). T cells persisted through at least 60 days, and the lesioned hemisphere was enriched for T cells with a tissue-resident memory (Trm) lymphocyte phenotype ($CD44^+$ $CD69^+$; **Fig. 8h, Fig. 9o**).

To test potential brain fibroblast-lymphocyte interactions after injury, we first defined the spatial relationships between T cells and lesional fibroblasts, increasing our sensitivity with the use of a pan-T cell reporter that labels both $CD4^+$ and $CD8^+$ T cells ($CD4^{cre}$; $R26^{TdT}$, **Fig. 8k,l**). By chronic time points after injury, we identified spatial proximity between T cells and fibroblast ECM, with fibroblast-associated T cells preferentially persisting over time (**Fig. 8m,n, Fig. 9p,q**). T cells were closer to fibroblast-dense regions – and more lesion-associated – than total macrophages/microglia ($Iba1^+$; **Fig. 8o, Fig. 9r**). T cells were also in close proximity to lymphocyte-interactive fibroblasts ($CD80^+$; **Fig. 8p,q, Fig. 9s**). To directly test the ability of fibroblast-dense late PT lesions to support lymphocyte survival, we developed an *ex vivo* assay wherein primary T cells were cocultured with dissected brain lesions (**Fig. 8r**). We found that 21dpi lesions supported increased T cell survival over 72 hours without impacting T cell proliferation or activation (**Fig. 8s, Fig. 9t-v, Fig. 17b**). Chronic lesions at 21dpi promoted increased T cell survival compared with early 7dpi lesions, and purified meningeal fibroblasts were

also sufficient to support T cell survival *in vitro* (**Fig. 8t, Fig. 9w,x**), though other lesional cells may also participate, including dendritic cells which also accumulated during PT injury and were enriched in the lesioned cortex through 60dpi (**Fig. 9y)**. These data suggest the presence of a late fibroblast state that can recruit and support brain lymphocytes and potentially modulate their functions.

2.1.4 Brain lesional myofibroblasts are coordinated by TGFβ signaling, pro-fibrotic myeloid cells, and perilesional glia to drive wound healing and limit chronic inflammation.

Next, we investigated the functional impacts of fibroblast-immune dialogues at multiple time points after brain injury. Given the spatiotemporal associations between lesional profibrotic myeloid cells (macrophages/microglia) and myofibroblasts, we first functionally tested the roles of acute to subacute myeloid cells. We confirmed the predicted beneficial role of lesional macrophages[91,116,134], using clodronate liposomes to deplete infiltrating monocytes, early macrophages, and total perilesional myeloid cells (**Fig. 11a-e, Fig. 17c,d**)**.** Treatment with clodronate liposomes reduced PT lesional fibroblasts and fibroblastic ECM coverage and increased lesion size (**Fig. 10a-c, Fig. 11f-h**), implicating macrophages in myofibroblast expansion and brain wound healing. Ligand-receptor analysis highlighted *Tgfb1* as one macrophage ligand that could contribute to the support of myofibroblasts (**Fig. 4r, Fig. 7x**). Indeed, *Tgfb1* colocalized with perilesional myeloid cells by 2dpi, and myeloid cells expressed the highest *Tgfb1* after injury (**Fig. 11i,j**). TGFB1 was also highly expressed by myeloid cells after stroke in non-human primates and after TBI in humans (**Fig. 7v,w, Fig. 11k,l**). To directly

investigate the functional importance of myeloid *Tgfb1*, we performed PT injury in mice with both microglia and macrophages conditionally induced to be TGFb1-deficient ($Cx3cr1^{creER}$; $Tgfb1^{flox/GFP\text{-}KO}$); these mice also had lower lesional fibroblastic ECM coverage, consistent with at least a partial contribution of myeloid cell-derived *Tgfb1* to the injury-induced fibroblast response (**Fig. 11m-o**).

Next, we tested the functional contributions of the myofibroblast state after brain injury. High levels of TGFβ promote myofibroblast differentiation, activation, proliferation, migration, and ECM production in peripheral organ wound healing, as well as many fibrotic and inflammatory pathologies[100]. Given the diverse roles of TGFβ in development[135], we used a genetic system where fibroblasts can be "blinded" to all TGFβ signaling in an inducible manner ($Col1a2^{creER}$; $Tgfbr2^{flox}$; conditional KnockOut/cKO, **Fig. 10d**). Adult cKO mice were viable and fibroblast resting topography was not impacted (**Fig. 12a**), likely consistent with a muted contribution of the TGFβ-driven myofibroblast state in adult mouse physiology[40] and/or less a transcriptionally active $Col1a2^{creER}$ allele at rest. However, after brain injury, lesional fibroblasts and associated ECM were greatly reduced in cKO mice, particularly within the inner lesion core, with increased lesion size (**Fig. 10e-h, Fig. 12b-g**). Flow cytometry of the PT-injured cortex revealed that infiltrating neutrophils were elevated acutely but declined by 4dpi in both control and cKO mice; however, cKO mice had a secondary lesional neutrophilia that persisted through at least 21dpi (**Fig. 10i**). Microscopy confirmed increased late perilesional neutrophils, and lesional monocytes were also increased (**Fig. 12h,i**). Persistent myeloid inflammation was specific to the lesioned cortical hemisphere in cKO mice, without differences identified in the contralateral hemisphere, meninges, blood, or spinal cord, nor did we detect overt

spinal cord abnormalities (**Fig. 12j-p**). Staining for apoptotic executor protein cleaved caspase 3 (cCasp3/CC3) revealed elevated extracellular puncta in the corpus callosum of cKO mice (**Fig. 12q,r**), a marker of neuroinflammation and white matter degeneration after TBI[136]. Fibroblasts can regulate the adjacent blood-brain barrier[39], and leakage/bleeding resulting from loss of this support[30] could contribute to neuroinflammation, apoptosis, and tissue loss. However, while we observed increased vascular leakage and hemorrhage after PT injury, as determined by Evans Blue extravasation and quantification of perilesional erythroid cell (RBC) accumulation, there was no significant further increase in cKO mice (**Fig. 12s,t**).

To orthogonally test the role of brain myofibroblasts after injury, we also used myofibroblast deleter mice (Cthrc1^{creER}; Rosa26^{DTA}), in which tamoxifen administration drives selective apoptosis of pro-fibrotic fibroblasts that are rare in resting mice.[129] Similar to myofibroblast-impaired cKO mice (Col1a2^{creER}; Tgfbr2^{flox}), Cthrc1-deleter mice had increased brain lesion size and reduced lesional ECM (**Fig. 10j-l**); these impacts were modest, consistent with known inefficient *Cthrc1*-driven myofibroblast deletion[129]. Next, we tested for a functional role of TGFβ in wound healing at chronic time points, delaying tamoxifen induction of PT-injured cKO mice until *after* most fibroblasts had transitioned out of the myofibroblast state (i.e., “late tamoxifen,” beginning 14dpi). In these mice, early lesional myofibroblasts were unperturbed. Late tamoxifen-induced mice showed no differences in late lesion size or neutrophil levels, with mild reductions in lesional ECM (**Fig. 10m,n, Fig. 12u**). Together, these data suggest a critical window after PT brain injury during which myofibroblasts limit the extent of subacute perilesional damage and

secondary innate neuroinflammation; however, the prevalence and functional importance of the myofibroblast state diminished by chronic time points.

TGFβ is canonically secreted into the ECM as a latent cytokine that requires activation[135], often via integrins $\alpha_v\beta_1$, $\alpha_v\beta_6$, and $\alpha_v\beta_8$[137]. While brain-associated co-expression of $\alpha_v\beta_1$ or $\alpha_v\beta_6$ was restricted to dural meningeal fibroblasts, $\alpha_v\beta_8$ co-expression was high in astrocytes and oligodendrocytes, with variable expression in lesional fibroblasts (**Fig. 12v**). To test for a functional role of the candidate integrin $\alpha_v\beta_8$, we utilized a well-validated blocking antibody, ADWA11[138]. Mice treated with $\alpha_v\beta_8$-blockade (AWDA11) partially phenocopied *Tgfbr2* cKO mice with reduced lesional fibroblasts and fibroblastic ECM coverage, although lesion sizes were not significantly altered (**Fig. 10o,p, Fig. 12w-z**). As in cKO mice, $\alpha_v\beta_8$-blockade drove chronic neutrophilic inflammation and trending increases in monocytes that were specific to the lesioned cortex (**Fig. 10q, Fig. 12aa-ac**). *Itgb8* reporter mice showed high TdT expression in perilesional astrocytes ($GFAP^+$) and minimal expression in lesional fibroblasts (**Fig. 12ad**). To functionally test the role of glial $\alpha_v\beta_8$, we genetically deleted *Itgb8* from the brain cortical parenchyma, including both glial cells and neurons **(**$hGfap^{cre}$; $Itgb8^{flox}$ mice; **Fig. 10r)**. After PT injury, there was reduced lesional ECM with unchanged lesion size, phenocopying $\alpha_v\beta_8$-blockade (**Fig. 10r,s, Fig. 12ae**). Similar results were observed using $Emx1^{cre}$, another brain parenchymal-targeting *Cre* allele with broader developmental expression (**Fig. 12af-ah**). These data implicate brain lesion-adjacent glial cells in optimally licensing TGFβ-mediated myofibroblast expansion via *Itgb8*, although additional cells, integrins, and/or mechanisms of TGFβ activation likely contribute[135].

Next, we investigated the cellular and molecular consequences of interrupting brain injury-associated myofibroblast programs. We again performed snRNAseq of PT lesional tissue and associated residual parenchyma at subacute and chronic timepoints, testing mice with TGFβ-blind fibroblasts (cKO, Col1a2^{creER}; Tgfbr2^{flox}), disrupted *Itgb8*-driven TGFβ activation (ADWA11), and controls, with a final library of 60,070 nuclei (**Fig. 13a**). After the identification of the expected brain cell types (**Fig. 13b,c**), we focused on lesional stromal cells (including 18,455 fibroblasts and 496 mural cells), which mapped onto our previously defined brain fibroblast states (**Fig. 13d-i)**. cKO mice had a profound loss of the subacute myofibroblast state clusters at 7dpi and a substantial reduction in multiple late-state fibroblast clusters at 21dpi, including dural-like, inner lesional, and lymphocyte-interactive states, consistent with a model where myofibroblasts give rise to late lesional fibroblast states (**Fig. 10t, Fig. 13j**). Quantitative fluorescent microscopy was also performed: cKO mice showed a reduction in myofibroblasts at 7dpi, as expected, and subsequently decreased lymphocyte interactive, pial-, and dural-like fibroblasts, with trending decreased late inner fibroblasts at 21dpi (**Fig. 13k-p**). The relative preservation of arachnoid-like leptomeningeal fibroblasts in cKO mice could indicate a strong selective pressure for restoration of this border state and raises the possibility that lesional leptomeningeal fibroblasts in cKO mice can emerge without passing through a TGFβ-driven myofibroblast state. Mice with $\alpha_v\beta_8$-blockade had relatively preserved fibroblast states; however, myofibroblasts from both cKO and $\alpha_v\beta_8$-blockaded mice expressed fewer ECM and pro-fibrotic genes (**Fig. 10u, Fig. 13q,r**), consistent with a shared impairment of the myofibroblast program.

Given predicted bidirectional fibroblast-macrophage interactions, we also defined the impacts of cKO myofibroblast interruption on brain lesional myeloid cells (**Fig. 13s-u**). cKO mice had reduced DAM and SAM myeloid clusters by snRNAseq, and trajectory analysis revealed impaired monocyte-to-SAM and microglia-to-DAM transitions (**Fig. 13v,w**). We orthogonally validated a relative decrease in SAM via flow cytometry, supporting an interruption of reciprocal myofibroblast-profibrotic macrophage interactions (**Fig 4w, Fig. 13x**). $\alpha_v\beta_8$-blockaded mice showed an expected cross-macrophage pro-inflammatory (M1-like) and dysmature transcriptional signature, consistent with known roles for *Itgb8*-mediated TGFβ autocrine signaling in supporting homeostatic microglial identity[139,140] (**Fig. 13y,z**). cKO mice also had reduced lesion-associated T cells, consistent with the loss of myofibroblast-derived late lymphocyte-interactive fibroblasts, with residual T cells largely confined to the disrupted lesion-parenchymal interface (**Fig. 10x, Fig. 13aa**). Lymphocytes from cKO mice had transcriptomic divergence by 21dpi, particularly within $CD8^+$ and $\gamma\delta$ T cell clusters, including increased expression of *Itgae*, the gene for CD103 (**Fig. 13ab-ad**). CD103 is a $CD8^+$ T cell residency marker, including in the brain parenchyma[124], and may reflect the observed altered perilesional lymphocyte topography in cKO mice. These data suggest that evolving fibroblast-immune interactions in the injured brain shape both the innate and the adaptive immune landscapes.

2.1.5 Discrete beneficial functions of early myofibroblasts and late lymphocyte interactive fibroblasts.

Next, we sought to characterize functionally relevant contributions of the transient myofibroblast state to brain injury and repair. As PT damage is a mild injury model, with

little functional brain impairment[141] (not shown), we turned to tMCAO, a more severe ischemia-reperfusion injury model that mirrors aspects of human stroke microanatomy and pathophysiology[142]. Control mice formed robust fibrotic lesions by 14 dpi, whereas mice with TGFβ-blind fibroblasts (cKO, Col1a2^{creER}; Tgfbr2^{flox}) displayed impaired fibrotic lesion – but not glial scar – formation, as well as substantial cortical tissue loss (**Fig. 14a**). cKO mice also displayed increased mortality (~90% versus ~15% of controls; no death among uninjured controls, **Fig. 14b**). Uninjured cKO mice showed no signs of peripheral organ dysfunction or inflammation (**Fig. 15a-c**), consistent with the relative lack of myofibroblast-state fibroblasts in healthy adult mouse tissues[40]. To better define how myofibroblasts were impacting mortality, we analyzed brains at 3dpi, prior to significant death in either genotype. cKO tMCAO injured brain hemispheres were enlarged relative to control hemispheres, with elevated polyclonal IgG staining, supportive of increased bleeding and edema (**Fig. 14c, Fig. 15d,e**). cKO brains had decreased mature oligodendrocytes and increased degenerating/dying neurons (**Fig. 14d, Fig. 15f**). Collectively, these data suggest that an intact myofibroblast response is required to limit early-to-subacute brain ischemic damage and functional tissue loss.

Next, we focused on the lymphocyte-interactive fibroblast state that was unique to late time points after injury. The chemokine CXCL12 signals via CXCR4 and drives fibroblast-lymphocyte interactions in several contexts[68]; we found that *Cxcl12* was highly expressed by late fibroblast subsets – particularly including the lymphocyte interactive fibroblast state – but was minimally expressed by the myofibroblast state (**Fig. 15g,h**). We used Col1a2^{creER} to conditionally delete *Cxcl12* from all fibroblasts in adult mice, thereby bypassing developmental roles of Cxcl12[143] (**Fig. 14f**). Chronic lesions from mice

with *Cxcl12*-deficient fibroblasts had decreased perilesional T cells without a change in PT lesion area, ECM deposition, or lymphocyte-interactive fibroblast coverage (**Fig. 14g-j, Fig. 15i-l**). In accordance with reduced late lesional lymphocytes that are poised to make IFNγ[125], lesion-proximal MHCII$^+$ cells showed a trending decrease, and flow cytometry confirmed a trend towards reduced MHCII expression on lesion-enriched macrophages (**Fig. 15m,n**). In contrast, total brain-infiltrating T cells – as assessed by flow cytometry – were not altered, indicating decreased lesional localization for T cells in the absence of fibroblast-derived CXCL12 (**Fig. 15o,p**). We also found increased effector cytokine expression among brain cortical CD4$^+$ and CD8$^+$ T cells, with a larger IFNγ^+ and smaller IL-17$^+$ subset elevated (**Fig. 14k-m, Fig. 15q-s**). No differences were identified with the inhibitory cytokine IL-10 or within meningeal or circulating T cells (**Fig. 14n, Fig. 15t-y**), suggesting local lesional impacts. Additionally, neutrophils were modestly elevated in injured hemispheres of mice with *Cxcl12*-deficient fibroblasts (**Fig. 14o**). These data suggest that late fibroblast subsets – particularly including immune interactive fibroblasts - maintain lesional niches, at least in part via the chemokine CXCL12, to support long-term lymphocyte accumulation but with dampened cytokine expression (**Fig. 14p**). These data support a model where fibroblasts and their interactions with immune cells are unexpected critical regulators of early brain injury and repair as well as long-term CNS neuroimmune balance (**Fig. 16**).

2.2 Discussion

Here, we characterize a functionally relevant fibroblast-immune conversation after brain injury, conserved across several animal models and species, involving fibroblast

activation, proliferation, migration, and ultimate persistence in multiple discrete states. We identify at least two discrete adaptive functions of brain fibroblasts after injury that act at discrete temporal phases. While fibroblasts are recently appreciated participants in CNS physiology and pathology, their ontogeny has remained controversial. Distinct studies arguing for pericyte[22,24,28,29] or fibroblast[31,76] origins for damage-associated CNS stromal cells have sometimes relied on shared markers[39] or qualitative lineage tracing[30]. Additionally, in contrast to peripheral organ injury-associated fibroblasts[6,60] or resting CNS fibroblasts[34,68,74,75], the dynamic states of CNS fibroblasts after injury are poorly defined. We use stromal cell lineage tracing to quantitatively define resting CNS fibroblasts as a major source for PT injury-responsive fibroblasts, though we do not rule out additional contributions. Our data is also consistent with a dural meningeal fibroblast origin, though injury-associated CNS fibroblast ontogeny is likely contextual and may be influenced by the nearest stromal cell sources[76].

Independently of ontogeny, we also show that the myofibroblast state, driven by TGFβ signaling, is a critical and temporally restricted player in brain injury. Profibrotic myofibroblasts proliferate, migrate, and engage in reciprocal interactions with profibrotic macrophage and microglial states (SAM/DAM) at sub-acute time periods after injury. Of note, this convergent profibrotic state – resembling both peripheral scar-associated macrophages[62] and disease-associated microglia[95] – suggests that the signals involved in PT injury-induced fibrosis play broader roles in tissue injury and regeneration across CNS pathology. While profibrotic macrophage programming seems to transcend ontogeny and traditional macrophage polarization states[144,145], heterogeneous expression of pro-inflammatory “M1-like” macrophage markers, as well as reparative “M2-

like" markers (e.g., *Arg1*), within SAM/DAM subsets suggests further macrophage state and positional parsing that remains to be performed[146]. Disruption of myeloid cells that provide TGFβ1, perilesional brain cells expressing integrin $\alpha_v\beta8$ that can liberate TGFβ, or fibroblast TGFβ signaling each attenuated the subacute brain fibroblast response. Glial cells such as astrocytes are a likely source of integrin $\alpha_v\beta_8$, particularly given observed expression patterns, though our work does not identify a singular cellular source. In mice with inducible loss of the myofibroblast state, brain lesions were larger – associated with increased loss of neuronal tissue – with late, unresolved innate inflammation that surpassed the post-injury peak. The mechanisms driving elevated late perilesional inflammation, which was also observed after blockade of $\alpha_v\beta8$-mediated TGFβ activation, remain to be fully elucidated; however, they likely involve feedback loops with secondary damage and subsequent further inflammatory cell recruitment. We propose that the myofibroblast state prevents this cycle by rapidly forming a new emergency border between lesioned tissue and salvageable brain – involving ECM and/or locally enriched chemokines – that limits damage-induced neutrophil migration between susceptible parenchyma and ischemic tissue[147] or disrupted vasculature[66]. Some fibroblasts may adopt late immune-suppressive states to further impact this balance[59]. Finally, loss of the myofibroblast state in a model of severe stroke was associated with excessive brain swelling, antibody extravasation, oligodendrocyte loss, neuronal degeneration, and higher mortality, suggesting that the myofibroblast state is clinically beneficial, at least in sub-acute time frames after CNS injury. Future experiments with CNS-restricted fibroblast tools will be key to identifying any roles of peripheral fibroblasts, although our data strongly suggest local fibroblast impacts. How the myofibroblast state differentially

impacts human CNS injuries across healthspan, neuroanatomy, and type of CNS injury remains intriguing and unknown.

Using integrated spatial and single nuclear transcriptomics and quantitative imaging, we also characterized the spatiotemporal evolution of a stereotypical brain fibroblast response to injury. Subacute myofibroblasts transitioned to distinct late states including meningeal border fibroblasts and lymphocyte-interactive fibroblasts that persisted long-term. These transitions may reflect evolving tissue requirements after injury-induced disruption of brain anatomic and immunologic protection[148], with early prioritization of physical boundary reformation and later prioritization of meningeal border homeostasis and immune protection, including lymphocyte recruitment, retention, and regulation. We show that fibroblast-derived CXCL12 was required for optimal recruitment of late lymphocytes to the lesion; fibroblast CXCL12 loss resulted in increased brain lymphocyte pro-inflammatory cytokines and persistent cortical neutrophilia, suggesting a critical immunomodulatory role for late lesional fibroblasts. Key future questions include how fibroblasts coordinate with lesional myeloid cells to provide these inhibitory/regulatory lymphocyte signals. As brain injuries are associated with several long-term sequelae that include risk of seizures, psychiatric disease, and neurodegeneration, we speculate that brain fibroblasts modulate chronic neuroimmune positioning and “tone” that impact these disease susceptibilities. Fibroblasts also display context-dependent state transitions in peripheral organs and diseases, including skin wounding[6], lung fibrosis[129], ulcerative colitis[45], and cancers[40,55,59], consistent with dynamic functions as coordinators of organ homeostasis and wound repair, representing intriguing therapeutic targets for brain disease.

2.3 Figures

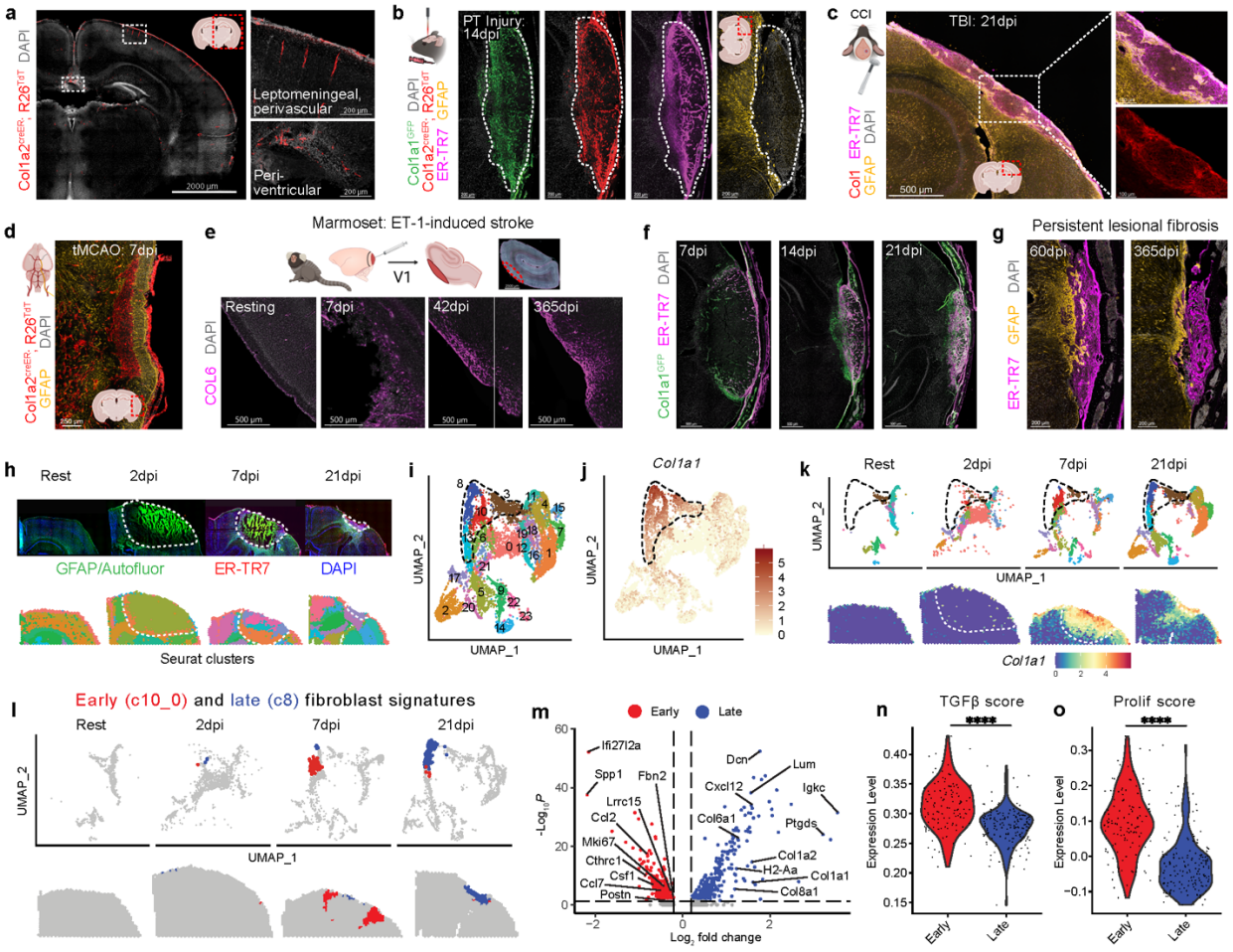


Fig. 1. Identification of a dynamic and persistent fibroblast response to brain injury. **a**, Homeostatic brain fibroblasts (Col1a2^{creER}; Rosa26^{TdT+}). Insets: pial/perivascular fibroblasts (top), periventricular/choroid plexus fibroblasts (bottom). Tamoxifen days -9-7 before sacrifice to track ontogeny. **b**, Lesional fibroblasts (Col1a1^{GFP+}; Col1a2^{creER}; Rosa26^{TdT+}) after photothrombotic (PT) injury (image of GFAP^{+} gliosis from separate mouse). Tamoxifen days -16-14 before injury. **c**, Fibrotic lesion (Col1^{+}, ER-TR7^{+}) within glial scar (GFAP^{+}) after controlled cortical impact (CCI) model of traumatic brain injury (TBI). **d**, Lesional fibroblasts after transient Middle Cerebral Artery Occlusion (tMCAO) stroke. Tamoxifen days -7-5 before injury to track ontogeny. **e**, Time course showing Collagen 6 (COL6) expression and persistence after endothelin-1-induced (ET-1) ischemic stroke (adult marmosets). **f-g**, PT injury time course showing fibroblasts (Col1a1^{GFP+}) and/or associated ECM (ER-TR7). **h**, Immunofluorescence (top) showing astrocyte- (GFAP^{+}) and fibroblast-dense regions (ER-TR7^{+}), and spatial plots (bottom, from same tissue) with 55μm spot-based clusters. Early necrosis-associated autofluorescence is prominent; white dotted lines denote lesion borders (10X Genomics, Visium). **i-j**, UMAP plots showing spot-based clusters (**I**) or fibroblast-enriched spots (**J**,

(Figure caption continued on the next page)

(Figure caption continued from the previous page)
Col1a1^{+}). 4 main fibroblast-enriched clusters highlighted (black dotted line). **k**, Time course showing fibroblast-enriched spots in UMAP (top) or spatial plots (bottom). **l-m,** UMAP and spatial plots (**l**) and volcano plot (**m**) comparing 7dpi "early-fibroblast-enriched" signature (cluster 10_0, red) and 21dpi "late-fibroblast-enriched" signature (cluster 8, blue). **n-o**, TGFβ score (**n**, genes upregulated in adventitial fibroblasts cultured with TGFβ) or proliferation score (**o**, 23 gene signature) across early/late fibroblast signatures. n=118 (early) or 160 (late) spots. ****p<0.0001; Mann-Whitney test (**n,o**). 200μm (**a**), 14μm (**b,f-g**), 30μm (**c**), 50μm (**d**), 40μm (**e**), or 10μm (**h**) slices; images represent two or more mice.

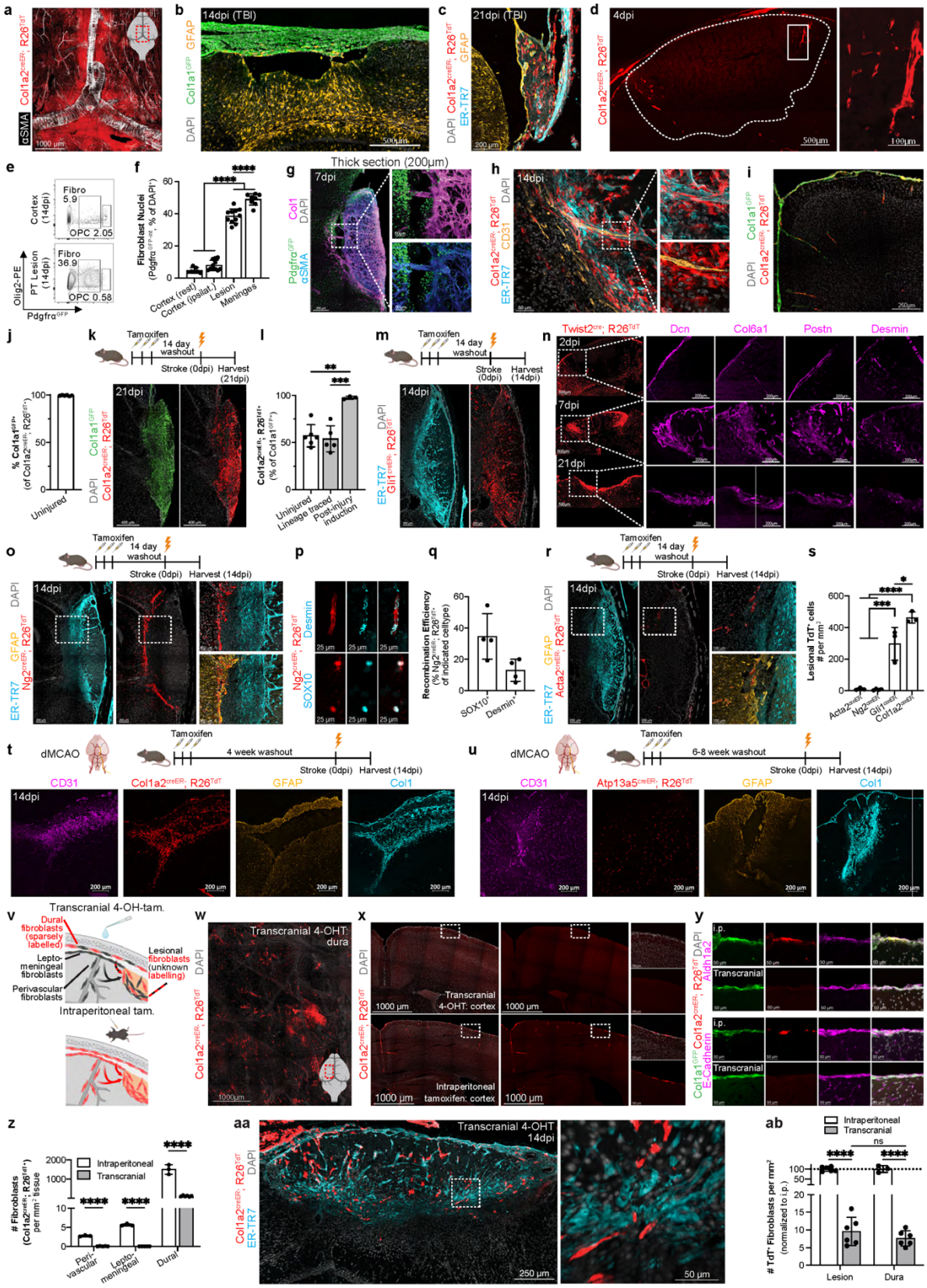


Fig. 2. Additional characterization of the CNS fibroblast response to PT injury. a,
(Figure caption continued on the next page)

(Figure caption continued from the previous page)
Homeostatic dural meningeal fibroblasts (Col1a2^{creER}; Rosa26^{TdT+}; whole-mounted dura, tamoxifen days $^{-}$11-$^{-}$7 before harvest). **b-c**, fibroblast infiltration (Col1a1^{GFP+}, **b,** or Col1a2^{creER}; Rosa26^{TdT+}, **c**) after CCI model of TBI (tamoxifen days $^{-}$18-$^{-}$16). **d**, Fibroblast expansion near lesion borders (white dotted line) by 4dpi (tamoxifen days $^{-}$14-$^{-}$12, $^{-}$7, 0-2dpi). **e-f**, Flow plot (**e**) and quantification (**f**) of fibroblast nuclei in Pdgfrα^{GFP} mice (marking fibroblasts and oligodendrocyte precursor cells [OPC]). n=7 (resting cortex), 11 (ipsilateral cortex/lesion, 14dpi), or 8 mice (dura, resting or 14dpi). **g-h**, Expanded perilesional vasculature and associated ECM after PT injury, with Pdgfrα^{GFP+} nuclei (**g**) or fibroblasts (**h**) visualized in lesional perivascular spaces. **i-l**, Resting fibroblasts (Col1a1^{GFP+}) partially recombined by Col1a2^{creER} (i.e., TdT^{+}) (**i**), quantification of *GFP* expression within recombined cells (**j**), 21dpi lesional fibroblasts (Col1a1^{GFP+}) with a fibroblast origin (TdT^{+}) (**k**), and quantification of recombination efficiency before and after injury (**l**). Tamoxifen days $^{-}$16-$^{-}$14 (before injury, "uninjured"/"lineage-traced") or 7-9dpi ("post-injury induction"). n=6 (uninjured), 5 (lineage traced), or 3 (post-injury) mice (1 40μm slice [uninjured] or 2 14μm slices averaged/mouse). **m**, Lineage traced fibroblasts in Gli1^{creER}; Rosa26^{TdT} mice (preferentially recombining fibroblast subsets in multiple tissues). Tamoxifen days $^{-}$16-$^{-}$14 before injury. **n**, Time course showing stromal/fibroblast (Twist2^{cre}; Rosa26^{TdT+}) expression of fibroblast markers (Dcn, Col6a1, Postn) and pericyte marker (Desmin). Serial sections; images representative of n=2-3 (2dpi), 2-6 (7dpi), or 2-7 (21dpi) mice. **o-q**, Lack of lineage traced lesional cells (with extra-lesional accumulation) in Ng2^{creER}; Rosa26^{TdT} mice (**o**), images of *Ng2*-lineage^{+} pericytes (Desmin^{+}) or oligodendrocyte-lineage cells (SOX10^{+}) (**p**), and quantification of recombination efficiency within each lineage (**q**). n=4 mice. Tamoxifen days $^{-}$16-$^{-}$14 before injury**. r,** Lack of lineage traced lesional cells (with sparse smooth muscle visible) in Acta2^{creER}; Rosa26^{TdT} mice. Tamoxifen days $^{-}$16-$^{-}$14 before injury. **s,** Quantification of lesional recombined cells in Acta2^{creER}, Ng2^{creER}, Gli1^{creER}, and Col1a2^{creER} mice. n=3 (Acta2^{creER}, Gli1^{creER}, Col1a2^{creER}) or 4 (Ng2^{creER}) mice. **t-u**, Lineage traced fibroblasts (**t**, Col1a2^{creER}; Rosa26^{TdT}) but not pericytes (**u**, Atp13a5^{creER}; Rosa26^{TdT}) accumulating within fibrotic lesions (Col1^{+}) after distal Middle Cerebral Artery Occlusion (dMCAO). Serial sections, 14dpi; tamoxifen given for 3 days, 4 weeks (**t**) or 6-8 weeks (**u**) prior to injury. **v-z,** Schematic (**v**) showing transcranial 4-hydroxy-tamoxifen (4-OHT) induction (top) and intraperitoneal tamoxifen induction (bottom). Transcranial 4-OHT sparsely recombines dural (**w**) but not perivascular or leptomeningeal (pial or arachnoid) fibroblasts (**x**), highlighted with arachnoid markers Aldh1a2 and E-Cadherin (**y**, top and bottom) and quantified in **z.** 2-10 days after induction; n=3 (intraperitoneal), 5 (transcranial-perivascular/leptomeningeal), or 6 (transcranial-dural) mice. **aa-ab**, Image (**aa**) and quantification (**ab**) of lesional fibroblasts recombined via transcranial 4-OHT. n=6 (lesion [2 slices averaged/mouse] and dura-transcranial) or 3 mice (dura-intraperitoneal). Graphs show mean$\pm$s.d. ns=not significant, *p<0.05, **p<0,01, ***p<0.001, ****p<0.0001; one-way ANOVA, Tukey post-test (**f,l,s**); multiple T-tests, Holm-Sidak correction (**z**); two-way repeated-measures ANOVA, Sidak's post-test (**ab**). 14μm (**b-d,h,k,m-p,r,aa**), 200μm (**g**), 40μm (**i**,**n** [desmin],**x,y**), or 10μm (**t,u**) slices; images represent two or more mice.

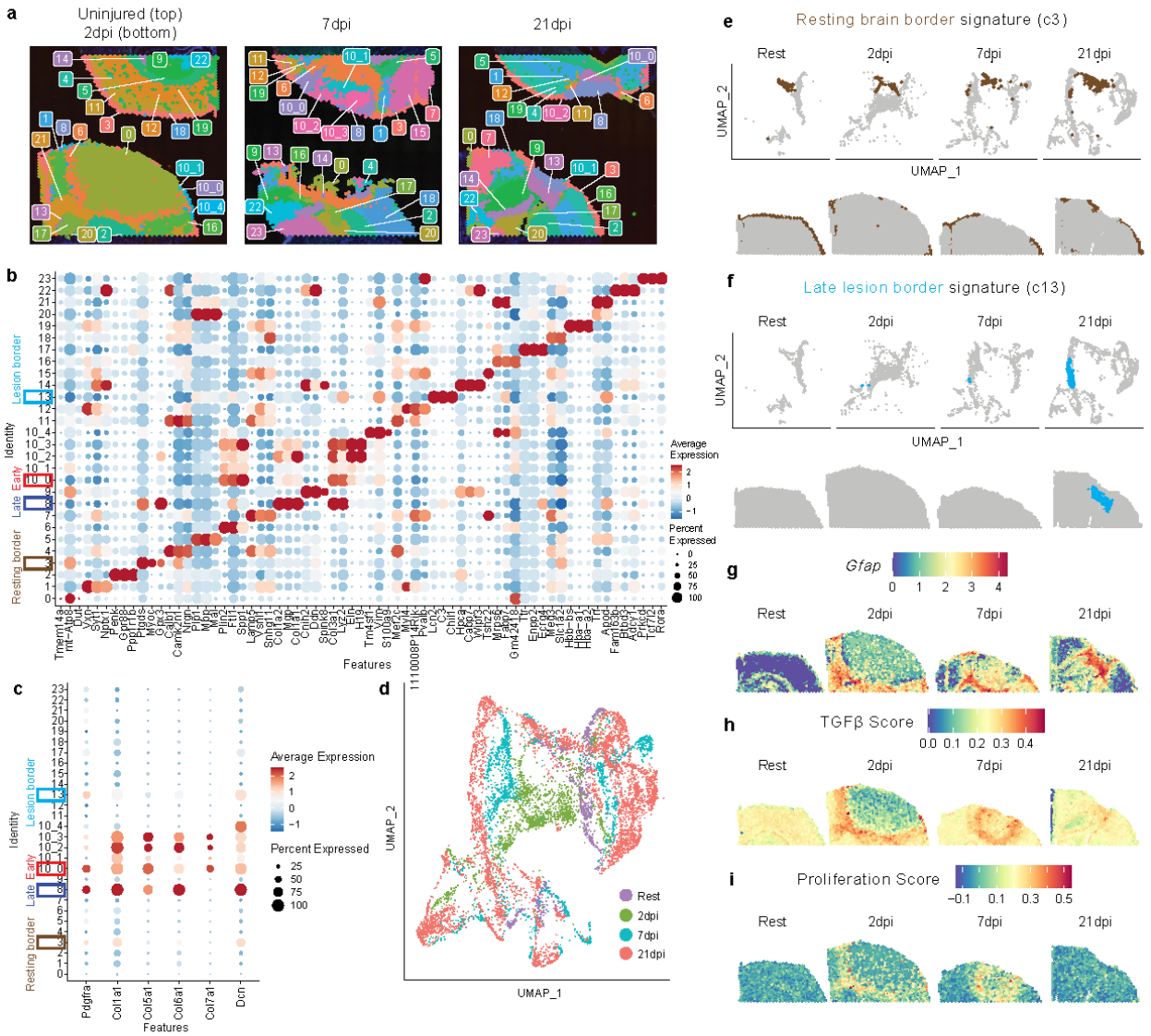


Fig. 3. Spatial transcriptomics characterization of PT injury. a, Spatial transcriptomics plot showing all spot-based clusters. Slices shown in original Visium slide configuration with two slices per capture area: rest (top left), 2dpi (bottom left), 7dpi (middle, 2 biological replicates), and 21dpi (right, 2 biological replicates). **b-c**, Dot plots showing marker genes (**b**) or fibroblast-associated genes (**c**) for all spot-based clusters. c3 ("resting brain border"), c8 ("late fibroblast"), c10_0 ("early fibroblast"), and c13 ("late lesion border") are highlighted (colored boxes). c10_0 was selected from c10 for further analysis based on high *Pdgfra* expression. **d**, UMAP showing spot-based clusters colored by timepoint, highlighting divergence among fibroblast-containing clusters. **e-f**, UMAP and spatial plots showing distribution of "resting brain border" fibroblast signature (**e**, cluster 3, brown) and "late lesion border" fibroblast signature (**f**, cluster 13, cyan). **g-i**, Spatial plots showing astrocyte-containing spots (**g**, *Gfap*$^{+}$) and distribution of "fibroblast TGFβ score" (**h**) or "proliferation score" (**i**).

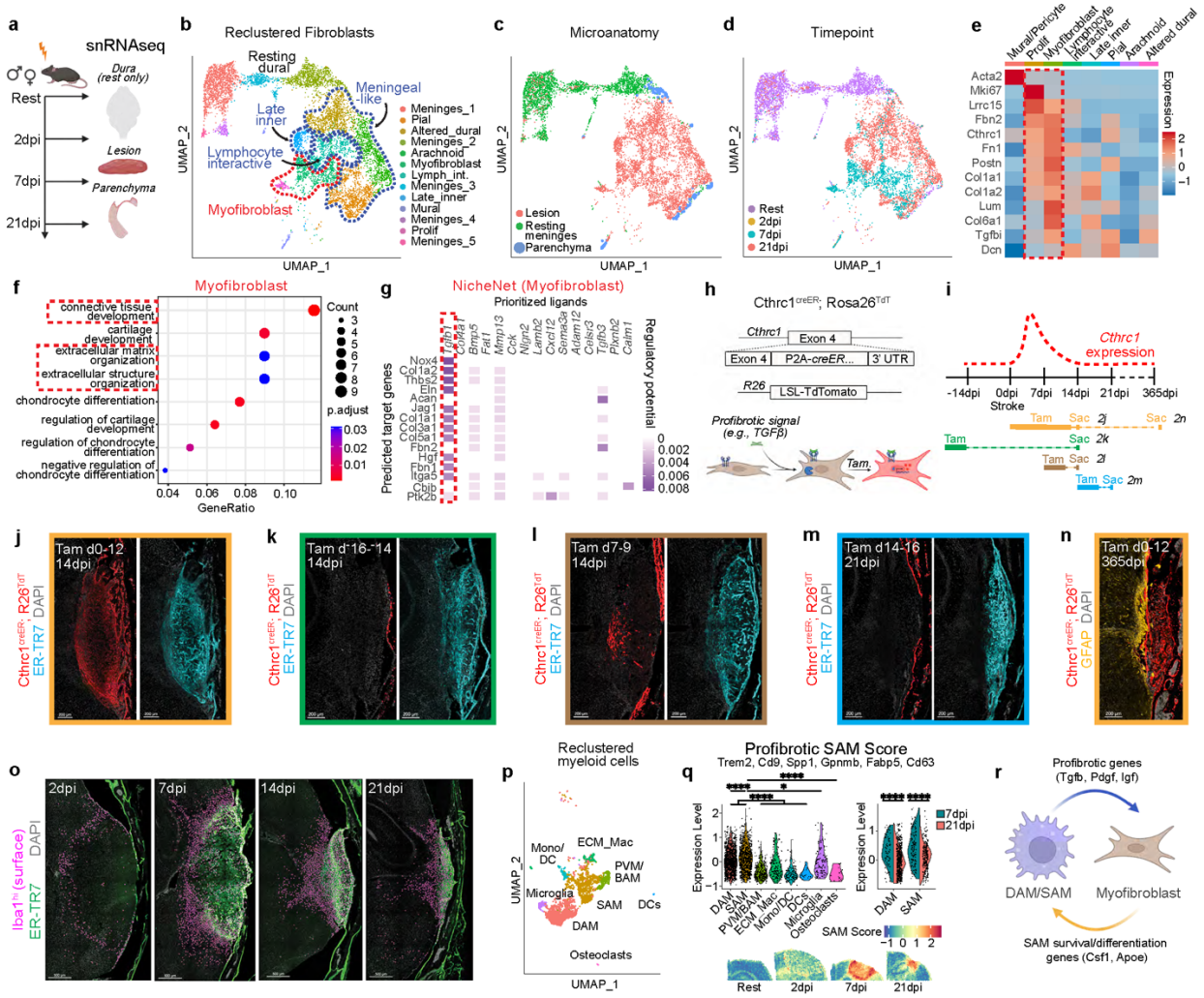


Fig. 4. Myofibroblasts spatiotemporally correlate with lesional profibrotic macrophages and disease-associated microglia. **a**, snRNAseq experimental schematic showing sample timepoints and microanatomy. **b-d**, UMAPs showing fibroblast subclusters (**b**), microanatomy (**c**, parenchymal fibroblasts enlarged for visibility), or timepoint (**d**). Dotted lines (**b**) highlight early myofibroblast/proliferative clusters (red) and multiple late states (blue). **e**, Heatmap of select fibrosis-related genes expressed in proliferative and myofibroblast clusters (red dotted line). **F-G**, Gene set enrichment analysis (**f**) and ligand-transcriptional-network analysis (**g**, NicheNet) within myofibroblasts. *Tgfb1* highlighted as top predicted driving ligand. **h-i,** Schematics showing Cthrc1^{creER}; Rosa26^{TdT} lineage tracing[129] (**h**) and hypothesized *Cthrc1* expression trajectory (**i**, with tamoxifen induction regimens for [**j-n**]). **j-n,** Confocal microscopy showing *Cthrc1*-lineage^{+} lesional fibroblasts after PT injury (tamoxifen induction and harvest days indicated), with robust injury-induced *Cthrc1* (*TdT*) expression (**j**) but lack of lineage-traced fibroblasts (**k**). Active *Cthrc1* expression is reduced but present at 7dpi (**l**, shown at 14dpi) and absent by 14dpi (**m**, shown at 21dpi). Labeled fibroblasts persist through 365dpi (**n**). **o**, Confocal microscopy showing time course of myeloid cell (Iba1^{hi} surface) lesional accumulation. **p-q**, Annotated UMAP of reclustered myeloid cells (**p**) and

(Figure caption continued on the next page)

(Figure caption continued from the previous page)
violin or spatial plots of profibrotic "SAM score" (**q**; *Trem2, Cd9, Spp1, Gpnmb, Fabp5,* and *Cd63*). In **q**: left, score by cluster; n=1267 (DAM), 816 (SAM), 305 (PVM/BAM), 173 (ECM_Macs), 116 (Mono/DC), 20 (DCs), 110 (Microglia), or 19 (Osteoclasts) nuclei. Right, score by timepoint within "DAM" and "SAM" lesional clusters; n=168/1080 (7/21dpi DAM) or 247/506 (7/21dpi SAM) nuclei. Bottom, score mapped onto spatial transcriptomic Visium data. **r**, Schematic showing potential ligand-receptor interactions between SAM/DAM and myofibroblasts, derived from **Fig. 7x**. **p<0.01, ****p<0.0001; Kruskall-Wallis test, Dunn's multiple comparisons correction (**q**, left; relevant comparisons shown); Mann-Whitney test (**q,** right). 14μm slices; images represent two or more mice.

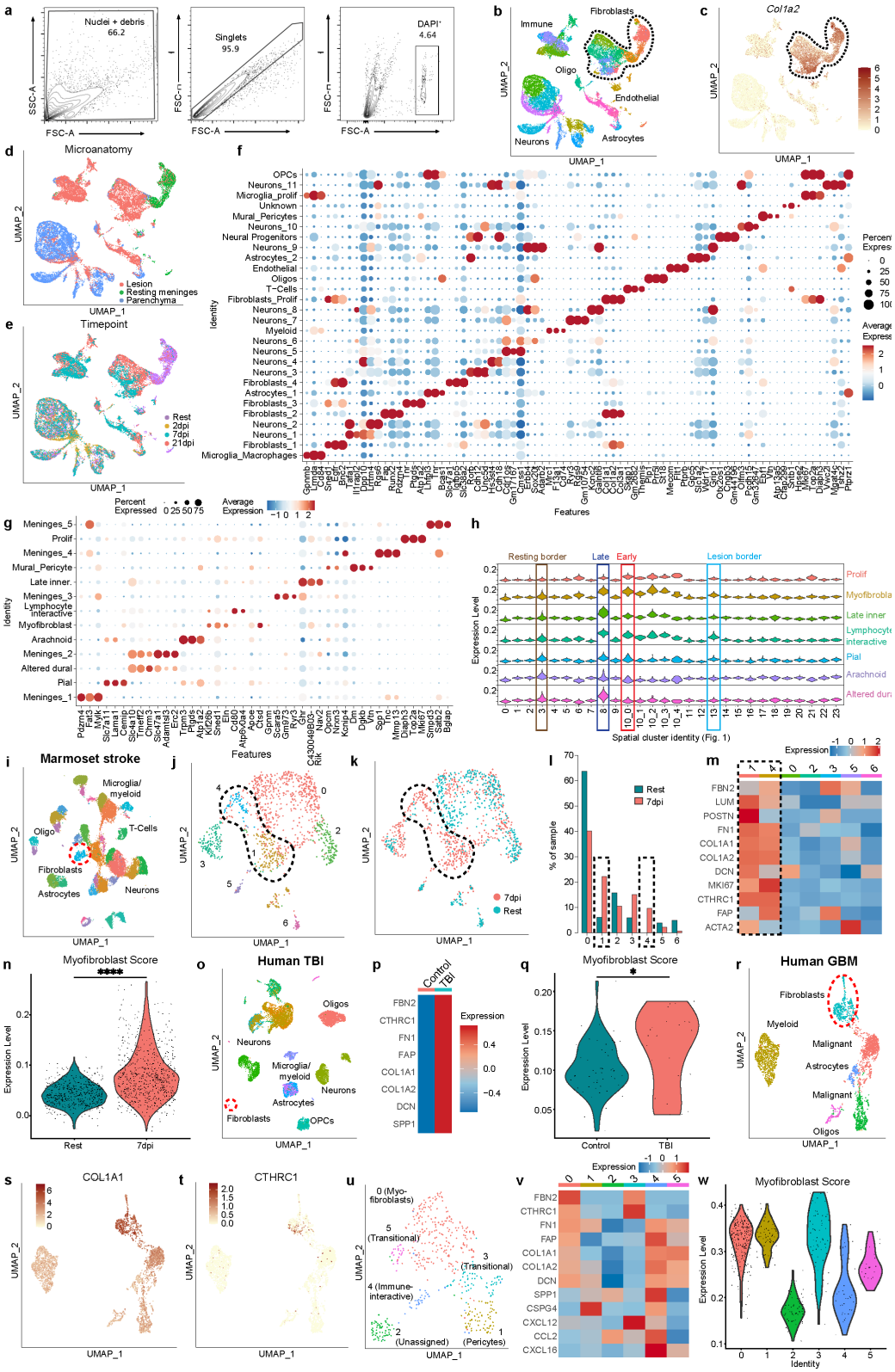


Fig. 5. Additional transcriptomic characterization of fibroblasts across species and injury models. a, Gating strategy for sorting DAPI⁺ nuclei for snRNAseq. **b-c**, Global

(Figure caption continued on the next page)

(Figure caption continued from the previous page)
UMAP (**b**) and *Col1a2* feature plot (**c**) showing fibroblast clusters (black dotted line) along with immune, oligodendrocyte lineage, endothelial, astrocyte, and neuron clusters. **d-e**, Global UMAPs showing barcode-based microanatomical metadata (**d**) or timepoint metadata (**e**). Neurons show parenchymal origin and broad temporal distribution, dural fibroblasts (dissected only at rest) show meningeal origin and resting distribution, and lesional fibroblasts, immune cells, and glial cell subsets show lesional origin and temporal heterogeneity. **f-g**, Dot plots showing marker genes for all cellular clusters (**f**) or all fibroblast subclusters (**g**). **h**, Violin plots mapping each lesional fibroblast cluster identity (via marker-DEGs) onto spatial transcriptomic clusters (**Fig. 1**), with spatial "fibroblast-enriched signatures" highlighted. **i**, Adult marmoset annotated snRNAseq data (Boghdadi et al.[131]) from endothelin-1-induced stroke (cortex, 7dpi). Fibroblasts highlighted (red dotted line) based on COL1A2 expression. **j-k**, UMAPs showing integrated fibroblasts from 7dpi (described in **i**) and resting adult marmoset dataset, showing annotated fibroblast subclusters (**j**) and timepoint (**k**). Black dotted line highlights 7dpi-enriched clusters 1 and 4. **l-m**, Bar plot showing relative cluster abundance (**l**, as proportion of fibroblast nuclei), and heatmap of select fibroblast/myofibroblast-related genes across fibroblast clusters (**m**). Black dotted line highlights 7dpi-enriched clusters 1 and 4. **n,** Violin plot showing myofibroblast-associated TGFβ score. n=529 (rest) or 663 (7dpi) fibroblasts. **o**, Human TBI annotated snRNAseq data (Garza et al.[132]), including control tissues (varying timepoints; controls from subjects with non-neurological causes of death). Fibroblasts highlighted (red dotted line) based on COL1A2 expression. **p-q**, Heatmap and violin plot showing elevated expression of selected fibroblast/myofibroblast genes (**p**) or myofibroblast-associated TGFβ score (**q**) in post-TBI fibroblasts. n=54 (control) or 23 (post-TBI) fibroblasts. **r-t**, Human glioblastoma multiforme (GBM) tissue snRNAseq data (Jain et al[35]), shown as UMAP (**r**) and feature plots of COL1A1 (**s**) or CTHRC1 (**t**). Cancer-associated fibroblasts are highlighted in (**r**) (red dotted line). **u-w**, UMAP showing reclustered fibroblasts (**u**), and heatmap or violin plot showing fibroblast expression of select fibroblast/myofibroblast genes (**v**) or myofibroblast-associated TGFβ score (**w**), enriched in cluster 0. n=235 (c0), 67 (c1), 66 (c2), 63 (c3), 38 (c4), or 25 (c5) fibroblasts. *p<0.05, ****p<0.0001; Mann-Whitney test (**n,q**).

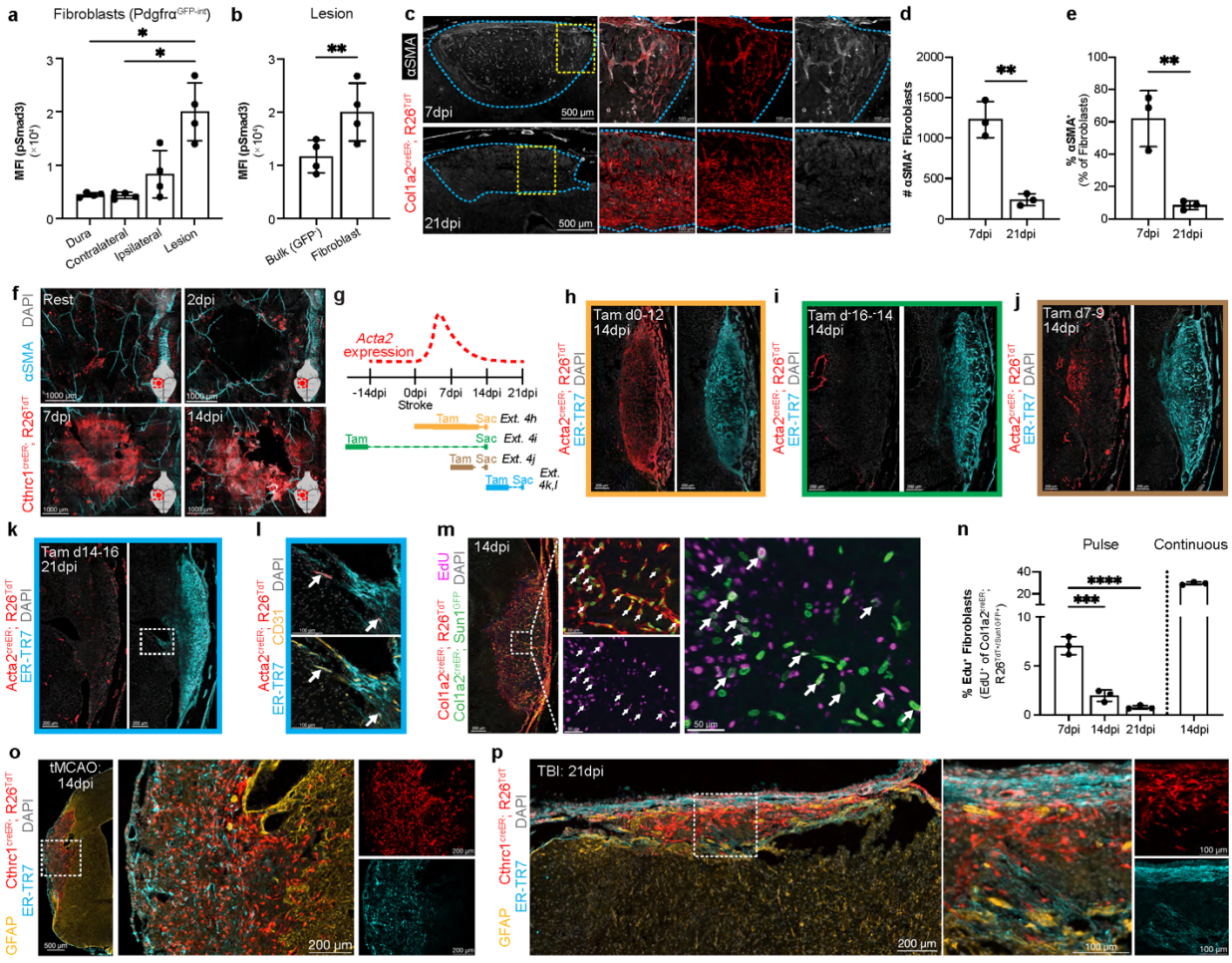


Fig. 6. Additional *in vivo* validation of early TGFβ-associated myofibroblasts. a-b, Nuclear flow cytometry showing elevated pSmad3 expression within lesional fibroblasts (Pdgfr$\alpha^{GFP\text{-}int}$) relative to dural/parenchymal fibroblasts (**a**) or other lesional cells (**b**). 7dpi; n=4 mice. **c-e,** Image of αSMA$^+$ expression among fibroblasts (Col1a2^{creER};R26^{TdT+}) at 7/21dpi (**c**), and quantification of the number (**d**) and percentage (**e**) of αSMA$^+$ fibroblasts. n=3 mice/group. **f,** Confocal microscopy showing Cthrc1^{creER}; Rosa26^{TdT+} fibroblasts in whole-mounted dural meninges at indicated timepoints. Tamoxifen days $^-$16-$^-$14 prior to injury (rest); days $^-$1-1 (2dpi); days 0-2, 5 (7dpi); or days 0-2, 5, 12 (14dpi). **g**, Schematic showing tamoxifen induction for (**h-l**) and hypothesized trajectory for *Acta2* (gene for αSMA) expression. **h-l**, Confocal microscopy showing *Acta2*-lineage$^+$ lesional fibroblasts after PT injury (tamoxifen induction and harvest days indicated), with but robust injury-induced *Acta2* (*TdT*) expression (**h**) but lack of lineage-traced fibroblasts (**i**). Active *Acta2* expression is reduced but present at 7dpi (**j**, shown at 14dpi) and absent by 14dpi (**k,** shown at 21dpi). **l** (inset from **k**) shows expected Acta2^{creER}; Rosa26^{TdT+} vascular smooth muscle cells (white arrows) near CD31$^+$ vessels. **m-n,** Image (**m**) and quantification (**n**) of fibroblast proliferation (EdU incorporation) 2 hours after EdU pulse ("Pulse"; 7dpi, 14dpi, or 21dpi) or after EdU injection every other day ("Continuous", and shown in **m**; 14dpi). In insets (**m**), arrows mark proliferating fibroblasts. Fibroblasts defined as

(Figure caption continued on the next page)

(Figure caption continued from the previous page)
Col1a2^{creER}; Rosa26$^{TdT+/Sun1GFP+}$. n=3 mice/timepoint (2 slices/mouse). **o-p**, *Cthrc1*-lineage^{+} fibroblasts within fibrotic scar after tMCAO (**o**) or TBI (**p**). Tamoxifen days 0,1,2,5,12 (**n**) or 0,1,2,5 (**o**). 14μm slices. *p<0.05, **p<0.01, ***p<0.001, ****p<0.0001; one-way repeated-measures ANOVA, Tukey post-test (**a**); paired Student's T-test (**b**); Student's T-test (**c,d**); one-way ANOVA, Tukey post-test (**n**).

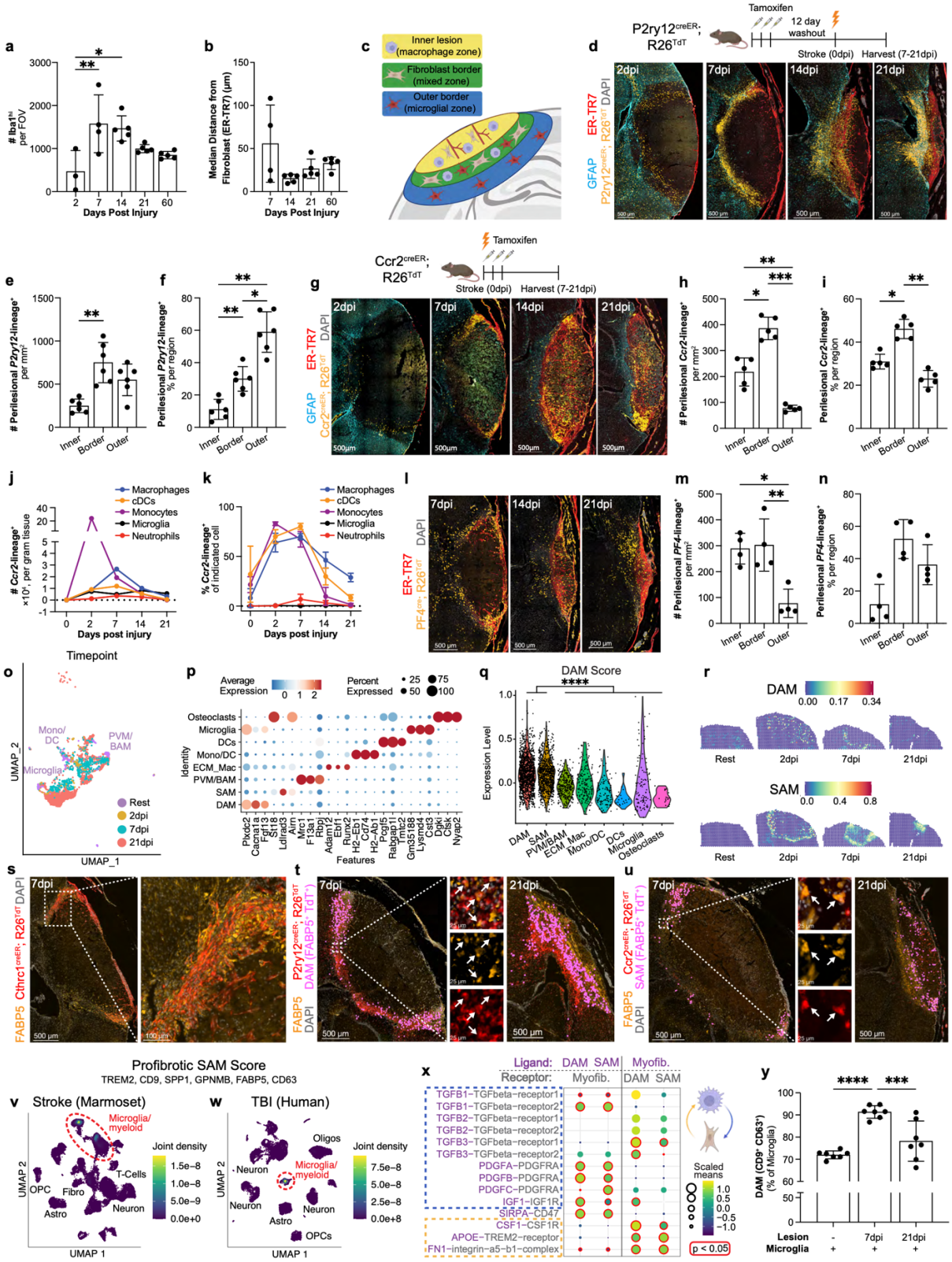


Fig. 7. Additional characterization of injury-responsive profibrotic CNS myeloid cells. a-b, Quantification of **Fig. 4o** showing number of myeloid cells (Iba1^{hi}

(Figure caption continued on the next page)

(Figure caption continued from the previous page)
macrophages and reactive microglia) per slice (**a**) and median myeloid cell distance from the nearest fibroblast-associated ECM (ER-TR7^{+}) surface (**b**). n=3 (2dpi), 4 (7dpi), or 5 (14/21/60dpi) mice (2-4 slices averaged/mouse). (**c**) Schematic showing myeloid cell distribution by ontogeny. **d-f**, Immunofluorescent imaging from microglia lineage tracer mice (**d,** P2ry12^{creER}; Rosa26^{TdT}; tamoxifen days $^{-}$14-$^{-}$12 before injury), with quantification of lineage traced cell density (**e**) and proportion (**f**) in inner core, fibrotic border, or outer glial regions at late timepoints (14/21dpi). n=6 mice. **g-i**, Imaging from monocyte lineage tracer mice (**g**, Ccr2^{creER}; Rosa26^{TdT}; tamoxifen 0-2dpi). with quantification of density (**h**) and proportion (**i**) by region, as above. n=5 mice. **j-k**, Time course showing *Ccr2*-lineage traced cells as normalized counts (**j**) or as a proportion of indicated population (**k**). Tamoxifen 0-2dpi. n=4 (0/2dpi), 3 (7/21dpi), or 5 (14dpi) mice. **l-n**, Imaging from BAM/PVM lineage tracer mice (**l,** PF4^{cre}; Rosa26^{TdT}), with quantification of density (**m)** and proportion (**n**) by region, as above. n=4 mice. **o-q**, UMAP of reclustered myeloid cells (**o**, colored by timepoint; major resting populations labelled), dot plot showing myeloid subcluster marker genes (**p**), and violin plot of Disease Associated Microglia ("DAM") score (**q**, an aggregate of 30 published DAM-specific markers). n=1267 (DAM), 816 (SAM), 305 (PVM/BAM), 173 (ECM_Macs), 116 (Mono/DC), 20 (DCs), 110 (Microglia), or 19 (Osteoclasts) nuclei. nuclei. **r,** DAM/SAM snRNAseq identities mapped onto spatial transcriptomic data. **s-u**, Imaging of FABP5^{+} cells near Cthrc1^{creER}; R26^{TdT+} myofibroblasts at 7dpi (**s**), and surfaced images of FABP5^{+} DAMs (microglia-derived, **t**) or SAMs (monocyte-derived, **u**) in perilesional/border regions at 7dpi (with inset) or 21dpi. **v-w**, Density plots showing expression of SAM score among myeloid cells after stroke in marmosets (**v**) or TBI in humans (**w**). **x**, Ligand-receptor interactions between SAM or DAM and myofibroblasts (CellPhoneDB). Left half: ligand (first/purple molecule in labelled pair) expressed by SAM/DAM, receptor (grey) expressed by myofibroblast. Right half: ligand expressed by myofibroblast, receptor expressed by SAM/DAM. Dotted lines and schematic (right) highlight modules with macrophage-expressed ligands (blue) or myofibroblast-expressed ligands (orange). **y,** Expression of DAM markers (CD9/CD63) on sorted homeostatic microglia cultured for 72 hours alone or with 7/21dpi lesions. n=7 wells/condition. Graphs show mean±s.d. ns=not significant, *p<0.05, **p<0.01, ***p<0.001, ****p<0.0001; one-way ANOVA, Tukey post-test (**a,b,y**); one-way repeated-measures ANOVA, Tukey post-test (**d,e,g,h,m,n**); Kruskall-Wallis test, Dunn's multiple comparisons correction (**q,** relevant comparisons shown). 14μm slices; images represent 2 or more mice.

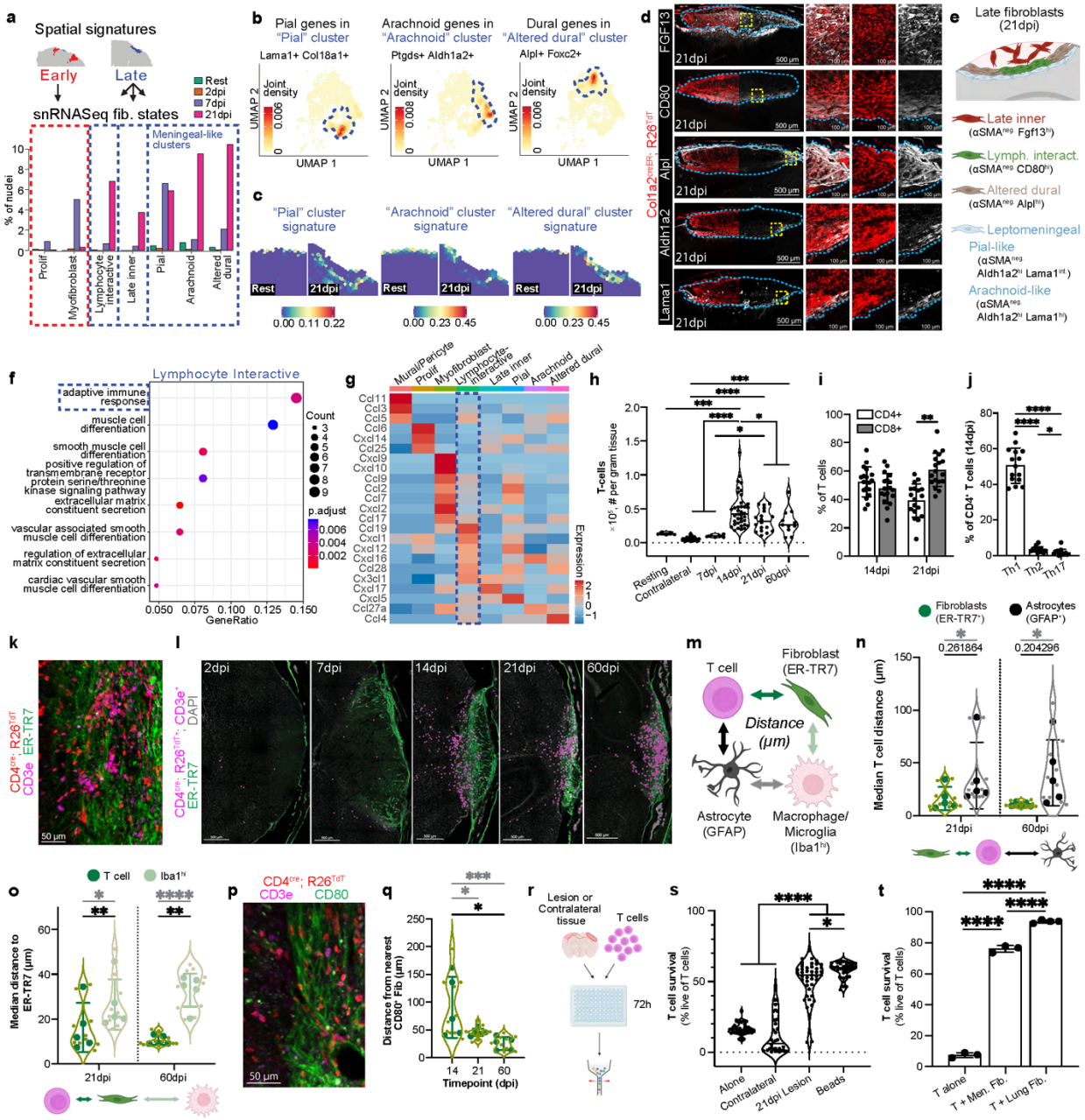


Fig. 8. Distinct late fibroblast states include lymphocyte interactive fibroblasts associated with T cell accumulation and persistence. a, Fibroblast cluster abundance over time, with corresponding early/late spatial signatures. **b**, Co-expression of pial, arachnoid, and dural genes[75] among corresponding clusters. **c**, snRNAseq signatures mapped onto spatial transcriptomic data, showing meningeal-like fibroblast distribution at rest (left, meningeal border) and 21dpi (right, new lesional-parenchymal border). **d-e,** Fluorescent imaging (**d**) and cartoon (**e**) of late fibroblast subset topography, including FGF13^{+} late inner fibroblasts, CD80^{+} lymphocyte interactive fibroblasts, Alpl^{+} altered dural fibroblasts, and Aldh1a2^{+}/Lama1^{+} leptomeningeal (pial/arachnoid) fibroblasts. **f**, Gene set enrichment analysis among lymphocyte interactive fibroblasts. **g**, Heatmap of

(Figure caption continued on the next page)

(Figure caption continued from the previous page)
chemokines expressed in at least 0.5% of any cluster, with lymphocyte interactive fibroblasts highlighted (blue dotted line). **h-j,** Total T cells (**h**, $CD3^+$), $CD4^+/CD8^+$ T cells (**i**), or Th1/2/17 $CD4^+$ T cells (**j**, $Tbet^+/Gata3^+/ROR\gamma t^+$; 14dpi) after PT injury (cortical flow cytometry). n=5 (rest), 46 (contralateral), 6 (7dpi), 38 (14dpi), 18 (21dpi), or 11 (60dpi) mice (**h**); 18 mice/timepoint (**i**); or 15 mice (**j**). **k-l**, Image (**k,** 21dpi) and time course (**l,** surfaces) showing T cells ($CD4^{cre}$; $Rosa26^{TdT+}$; $CD3e^+$) near fibroblast-rich lesions (ER-$TR7^+$). **m**, Schematic for proximity analysis between T cells ($CD4^{cre}$; $Rosa26^{TdT+}$; $CD3e^+$) or myeloid cells ($Iba1^{hi}$, macrophages/reactive microglia) and fibroblast ECM (ER-TR7) or reactive astrocytes (GFAP). **n-o**, Median T cell distance from nearest fibroblast-ECM or astrocyte surface (**n**), and T or myeloid cell distance from nearest fibroblast surface (**o**). 21/60dpi. n=5 mice/timepoint (2 slices averaged/mouse; slice values and statistics shown with lighter colors/smaller points). **p-q,** Image (**p,** 21dpi) and quantification (**q**) of T cell proximity to $CD80^+$ lymphocyte interactive fibroblasts, 14/21/60dpi. n=5 mice/timepoint (2 slices averaged/mouse). **r-s**, Schematic for *ex vivo* lesional coculture (**r**) and quantification of T cell survival (**s**, 21dpi lesions). n=30 (alone), 31 (contralateral), 44 (21dpi lesion), or 29 (beads) wells. **t,** T cell survival after coculture with dural meningeal or lung fibroblasts. n=3 (alone, meningeal) or 4 (lung) wells. Graphs show mean±s.d. *p<0.05, **p<0.01, ***p<0.001, ****p<0.0001; one-way ANOVA, Tukey post-test (**h**,**q,s**,**t**); multiple T-tests, Holm-Sidak correction (**i; n,o** [paired per point, unpaired per slice]); one-way repeated-measures ANOVA, Tukey post-test (**j**). 14μm slices; images represent two or more mice.

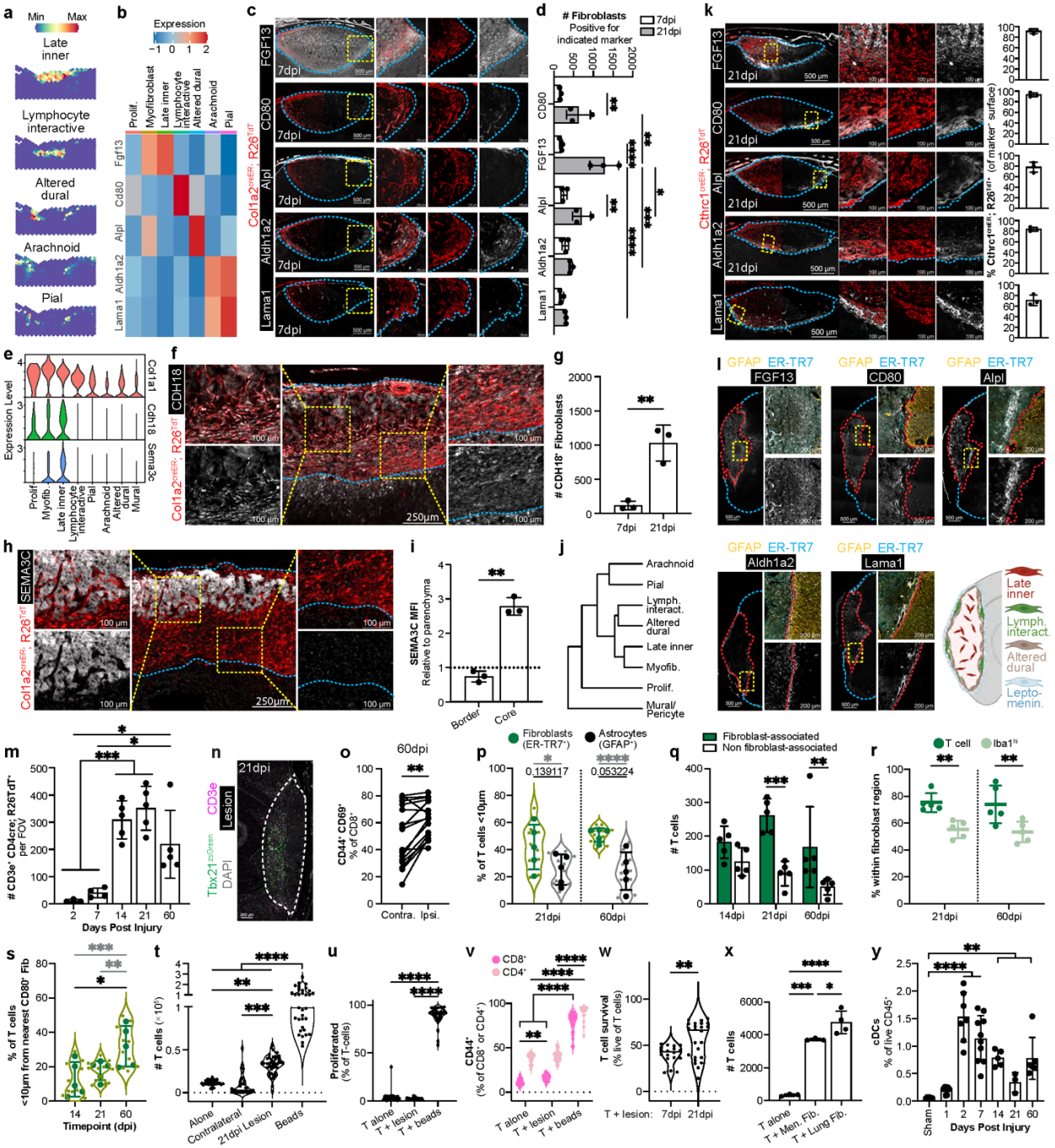


Fig. 9. Additional characterization of late lesional fibroblasts. a, Single nuclear signatures of late lesional fibroblast states mapped onto spatial transcriptomic data, showing expected localization. **b,** Heatmap of selected late fibroblast state markers used for imaging. **c,** Late fibroblast state markers shown at 7dpi. **d**, Quantification of **c** and **Fig. 8d**, showing the number of subset marker-positive fibroblasts at 7/21dpi. n=3 mice/timepoint. **e-i**, Violin plots (**e**) showing ECM (*Col1a1*) and smooth muscle-related[149,150] (*Cdh18, Sema3c)* genes (enriched among late inner fibroblasts), with imaging and quantification of CDH18^{+} fibroblasts (**f,g**) and SEMA3C within the inner core *(Figure caption continued on the next page)*

(Figure caption continued from the previous page)
(21dpi; **h,i**). n=3 mice/timepoint. **j,** Phylogenetic tree showing lesional stromal cell cluster relationships. **k,** Imaging (left) and quantification (right) of subset marker expression among *Cthrc1*-lineage^{+} fibroblasts (tamoxifen continuously, i.e. days 0-2, 5, 8, 11, etc.; fibroblast- vs. non-fibroblast-adjacent Fgf13/Lama1 quantified). n=3 mice. **l,** Fibroblast subset marker staining after tMCAO (14dpi) and cartoon of fibroblast subset topography. **m**, Perilesional T cell time course (CD4^{cre}; Rosa26^{TdT+}; CD3e^{+}). n=3 (2dpi), 4 (7dpi), or 5 (14/21/60dpi) mice (2-5 slices averaged/mouse). **n**, Lesional type 1 lymphocytes (Tbet$^{zsGreen+}$, 21dpi). **o**, Tissue resident memory CD8^{+} T cell distribution (CD44^{+} CD69^{+}; 60dpi). n=17 mice. **p-r**, T cell proportion <10μm from nearest fibroblast-associated ECM (ER-TR7^{+}) or astrocyte (GFAP^{+}) surface (**p**), T cells within or outside fibroblast-dense lesion (**q**), and T or myeloid cell (Iba1^{hi}) proportion within lesion (**r**). n=5 mice/timepoint (2-4 slices averaged/mouse; slice values and statistics shown with lighter colors/smaller points). **s,** T cell proportion <10μm from nearest CD80^{+} fibroblast. n=5 mice/timepoint (2 slices averaged/mouse; slice values and statistics shown with lighter colors/smaller points). **t-v**, T cell counts (**t**), proliferation (CTV dilution, **u**), and activation (**v**, CD44^{+}) after coculture (21dpi lesions). n=36 (**t,u**) or 33 (**v**; alone), 31 (contralateral), 43 (**t**) or 44 (**u,v;** 21dpi lesion), and 33 (**t,u**) or 30 (**v**; beads) wells. **w**, T cell survival after coculture with 7dpi or 21dpi lesion. n=18 (7dpi) or 24 (21dpi) wells. **x,** T cell survival counts after coculture with dural meningeal or lung fibroblasts. n=3 (alone, meningeal) or 4 (lung) wells. **y,** Conventional dendritic cell (cDC) infiltration and persistence after PT injury (cortical flow cytometry). n=6 (sham/60dpi), 7 (1/2dpi), 10 (7dpi), 5 (14dpi), or 3 (21dpi) mice. Graphs show mean$\pm$s.d. ns=not significant, *p<0.05, **p<0.01, ***p<0.001, ****p<0.0001; two-way repeated-measures ANOVA, Sidak's post-test (**d,q,v**); student's T-test (**g,w**); paired Student's T-test (**i,o**); one-way ANOVA, Tukey post-test (**m,s-u,x,y**); multiple T-tests, Holm-Sidak correction (**p** [per slice]); multiple paired T-tests, Holm-Sidak correction (**p** [per point], **r**). 14μm slices; images represent two or more mice.

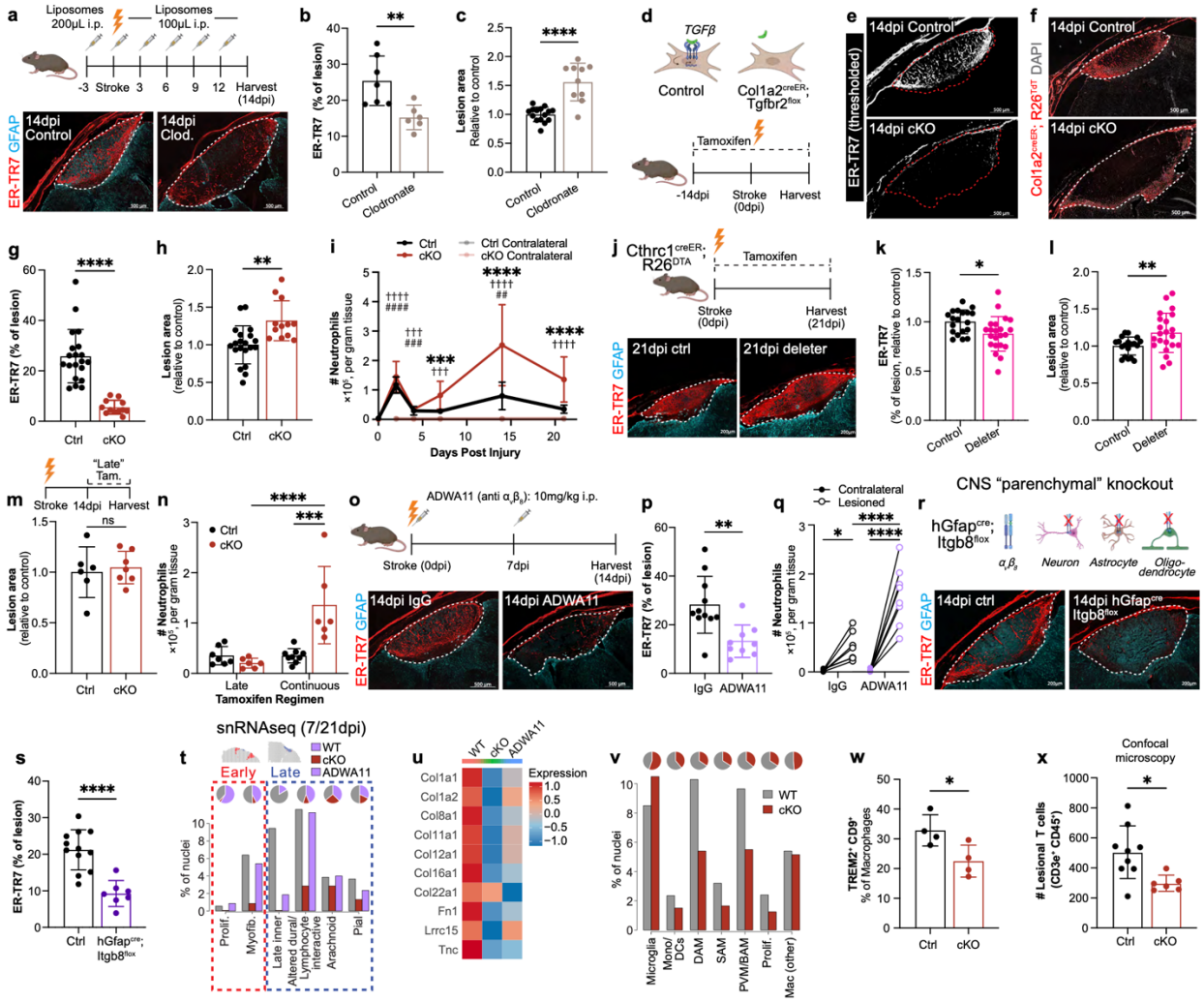


Fig. 10. Brain lesional myofibroblasts are coordinated by TGFβ signaling, pro-fibrotic myeloid cells, and perilesional glia to drive wound healing and limit chronic inflammation. a-c, Lesional images after control/clodronate liposomes (**a**), ECM (ER-TR7) coverage (**b**), and lesion size (**c,** normalized per experiment), 14dpi. n=7 and 15 (control, **b** and **c**) or 6 and 10 (clodronate, **b** and **c**) mice (2 slices averaged/mouse). **d**, Schematic of ablated TGFβ-signaling in Col1a2^{creER}; Tgfbr2^{flox} cKO fibroblasts (control and cKO tamoxifen induction days $^{-}$14-$^{-}$12, $^{-}$7, 0-2, 5, 8, etc.). **e-h**, Control/cKO lesional images with thresholded ER-TR7 (**e**) or lineage traced fibroblasts (**f**, Col1a2^{creER}; Rosa26^{TdT+}), ER-TR7 coverage (**g**), and lesion size (**h**, normalized per experiment), 14dpi. n=20 (control) or 12 (cKO) mice (2 slices averaged/mouse). **i**, Cortical neutrophil time course in controls/cKOs. n=6 (0dpi-control [non-littermate], 2/4/7dpi-control, 2/7/21dpi-cKO), 12 (14dpi-control), 9 (21dpi-control), 3 (0dpi-cKO), 5 (4dpi-cKO), or 7 (14dpi-cKO) mice. **j-l,** Control or myofibroblast deleter (Cthrc1^{creER}; Rosa26^{DTA}) lesional images (**j**), ER-TR7 coverage (**k**, normalized per experiment), and lesion size (**l,** normalized per experiment), 21dpi. n=19 (control; cre-negative or vehicle) or 22 (deleter) mice (2 slices averaged/mouse). **m,** Lesion size in controls/cKOs after late tamoxifen (days 14-16, 19, 22, 25). 28dpi; n=6 (control) or 7 (cKO) mice/group (2 slices

(Figure caption continued on the next page)

(Figure caption continued from the previous page)
averaged/mouse). **n**, Cortical neutrophils in controls/cKOs after late or continuous tamoxifen, 21dpi. n=7 (control-late), 6 (cKO-late, cKO-continuous), or 9 (control-continuous) mice. **o-q,** Control (IgG) or $\alpha_v\beta_8$-blocked (ADWA11) lesional images (**o**), ER-TR7 coverage (**p**), and cortical neutrophils (**q**), 14dpi. n=11 (IgG) or 9 (ADWA11) mice (**p**, 2 slices averaged/mouse); n=7 (IgG) or 8 (ADWA11) mice (**q**). **r-s**, Control or $hGfap^{cre}$; $Itgb8^{flox}$ lesional images (**r**) and ER-TR7 coverage (**s**), 14dpi. n=12 (control) or 7 (cKO) mice (2 slices averaged/mouse). **t**, Fibroblast cluster abundance (snRNAseq) in control, cKO ($Col1a2^{creER}$; $Tgfbr2^{flox}$), and ADWA11-treated mice (7/21dpi). Red/blue boxes highlight early/late-enriched states. **u**, Myofibroblast genes within the myofibroblast cluster. **v-x**, Myeloid cluster abundance (**v**), SAM frequency (**w**, flow cytometry, 14dpi), or perilesional T cells (**x**, 14dpi) in controls/cKOs. n=4 mice/group (**w**); n=9 (control) or 6 (cKO) mice (**x**, 2 slices averaged/mouse). Graphs show mean±s.d. *p<0.05, **p<0.01, ***p<0.001, ****p<0.0001; * lesioned-control vs. lesioned-cKO; # lesioned-control vs. contralateral-control; † lesioned-cKO vs. contralateral-cKO (**i**). Student's T-test (**b**,**c**,**g**,**h,k,l,m,p,s,w,x**); two-way repeated-measures ANOVA, Sidak's post-test (**i** [per timepoint], **q**); two-way ANOVA, Sidak's post-test (**n**). 14μm slices; dotted lines show lesion boundary (**a,e,f,j,o,r**); images represent two or more mice.

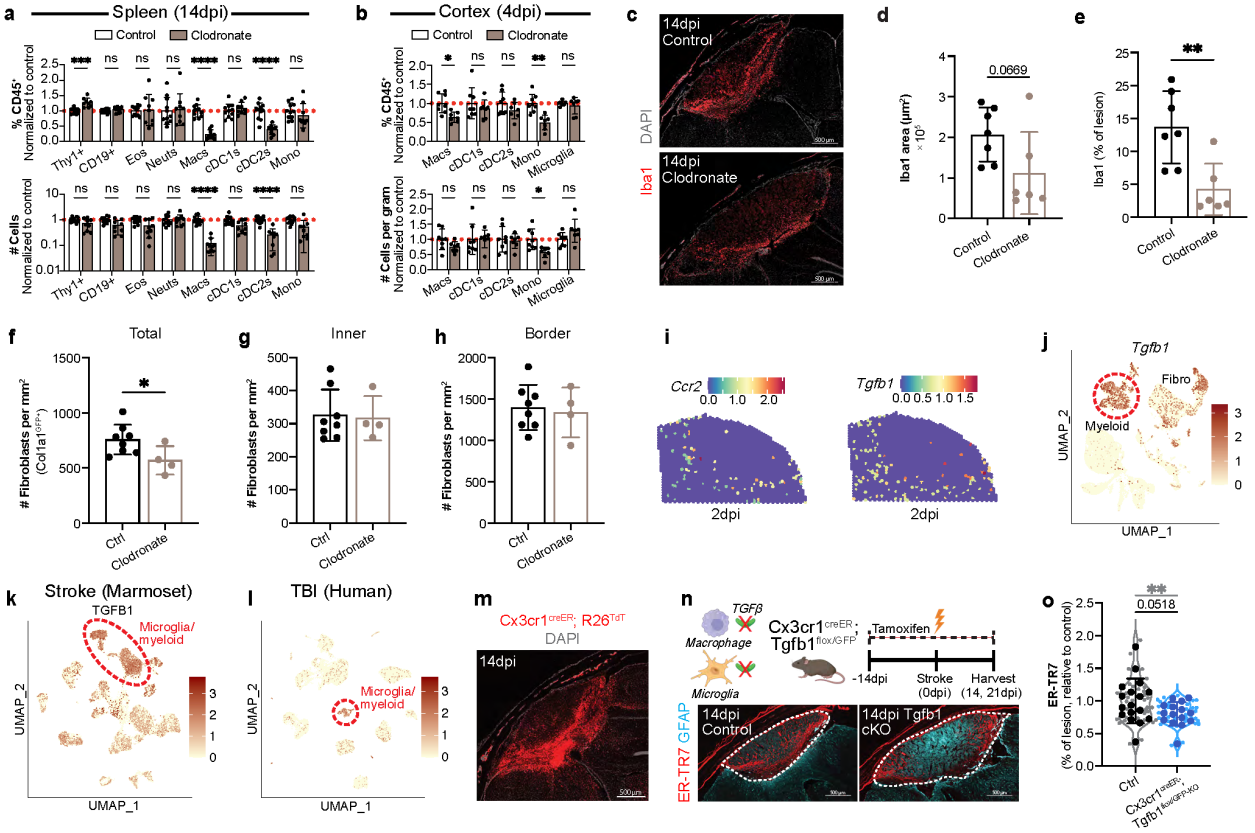


Fig. 11. Profibrotic macrophages promote CNS fibroblast expansion. a-b, 14dpi splenic immune cells (**a**) or 4dpi cortical phagocytic myeloid cells (**b**) after treatment with control or clodronate liposomes, as frequency (top) or counts (bottom). n=11 and 8 (control, **a** and **b**) or 9 and 7 (clodronate, **a** and **b**) mice. Within each experiment, clodronate liposome-treated mice were normalized to control liposome-treated mice. **c-e**, Perilesional myeloid cell (Iba1) staining at 14dpi, with images (**c**) and quantification via thresholding (**d**) and normalization to reactive astrocyte (GFAP)-traced lesion area (**e**). n=7 (control) or 6 (clodronate) mice (2 slices averaged/mouse). **f-h,** Quantification of lesional Col1a1^{GFP+} fibroblast total density (**f**) and density within in inner core (**g**) or fibrotic border (**h**) in control or clodronate-treated mice. 14dpi; n=8 (control) or 4 (clodronate) mice (2 slices averaged/mouse). **i,** Spatial transcriptomic feature plots from Visium dataset (**Fig. 1**) showing *Ccr2* and *Tgfb1* transcripts in perilesional distribution at 2dpi. **j-l**, Feature plot of *Tgfb1,* plotted in order of expression, from mouse PT injury snRNAseq (**j**), marmoset stroke snRNAseq (**k**), or human TBI snRNAseq (**l**); dotted lines highlight myeloid cells. **m**, Representative image showing recombined macrophages and microglia (TdT^{+}) in a Cx3cr1^{creER}; Rosa26^{TdT} mouse (tamoxifen as below; 14dpi). **n-o**, Lesional images (**n**; dotted line shows lesion boundary) and ER-TR7 coverage (**o**, normalized per experiment) following genetic targeting of macrophage and microglial *Tgfb1* in Cx3cr1^{creER}; Tgfb1$^{flox/GFP\text{-}KO}$ mice (14dpi). Controls were littermate Cx3cr1^{creER}; Tgfb1$^{flox/+}$ mice; tamoxifen as in **Fig. 10d**. n=17 (control) or 15 (*Tgfb1* cKO) slices (2 slices averaged/mouse; slice values and statistics shown with lighter colors/smaller points). Graphs show mean±s.d. ns=not significant, *p<0.05, **p<0.01, ***p<0.001, ****p<0.0001; *(Figure caption continued on the next page)*

(Figure caption continued from the previous page)
multiple T-tests, Holm-Sidak correction (**a,b**); Student's T-test (**d-h, o**). 14μm slices; images represent two or more mice.

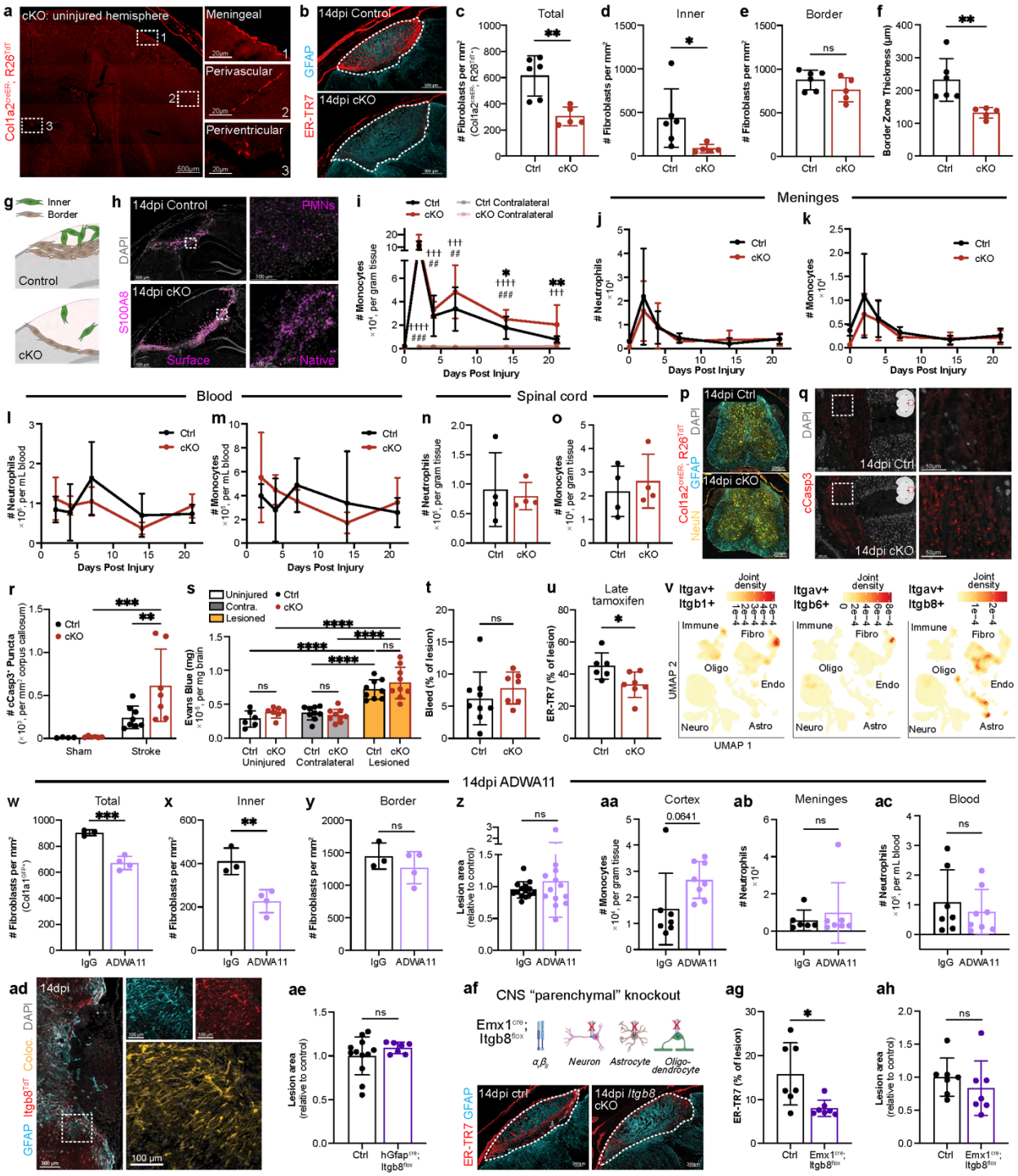


Fig. 12. TGFβ drives CNS wound healing and resolution of inflammation. a, Intact fibroblast topography in uninjured cKO (Col1a2^{creER}; Tgfbr2^{flox}) parenchyma (insets: leptomeningeal/perivascular/periventricular fibroblasts). **b**, Lesional images showing ER-TR7 in controls or cKOs, 14dpi (tamoxifen as in **Fig. 4d**; dotted line shows lesion boundary). **c-g**, Quantification of lesional Col1a2^{creER}; Rosa26^{TdT+} fibroblasts fibroblast total density (**c**) and density within inner core (**d**) or fibrotic border (**e**), with cKOs

(Figure caption continued on the next page)

(Figure caption continued from the previous page)
showing overall and inner fibroblast reduction with an intact but thinner lesional border (**f**), summarized in (**g**). 14dpi; n=6 (control) or 5 (cKO) slices/group (2 slices averaged/mouse). **h**, S100A8^{+} neutrophils (PMN; left, surfaced; right, native) in controls (top) or cKOs (bottom), 14dpi. **i,** Time course showing cortical monocytes in controls/cKOs. n=6 (0dpi-control [non-littermate], 2/4/7dpi-control, 2/7/21dpi-cKO), 12 (14dpi-control), 9 (21dpi-control), 3 (0dpi-cKO), 5 (4dpi-cKO), or 7 (14dpi cKO) mice. **j-o**, Neutrophil or monocyte counts in meninges (**j-k**), blood (**l-m**), or 14dpi spinal cord (**n-o**) of controls/cKOs. n=3 (0dpi control [non-litermate]/cKO), 6 (2/4/7dpi control, 2/21dpi cKO), 12 (14dpi control), 9 (21dpi control), 5 (7dpi cKO), 5 (4dpi cKO, **j-k**) or 6 (4dpi cKO, **l-m**), and 7 (14dpi cKO) mice; n=4 mice/group (**n-o**). **p**, Control/cKO spinal cords showing intact neurons without fibrosis/gliosis (14dpi). **q-r,** Image (**q**) and quantification (**r**) of cCasp3^{+} puncta within corpus callosum in control or cKO mice (14dpi). n=4 (sham-control), 6 (sham-cKO), 8 (stroke-control), or 7 (stroke-cKO) mice (2-4 slices averaged/mouse). **s**, Evans Blue extravasation in uninjured (resting or sham) or contralateral/lesioned hemispheres of controls/cKOs, 4dpi. n=6 (uninjured-control), 7 (uninjured-cKO), or 9 (contralateral/lesioned-control and cKO), mice. **t**, Quantification of overt bleeding in controls/cKOs, 4dpi. n=9 (control) or 7 (cKO) mice. **u,** ER-TR7 coverage in control or cKO mice induced with late tamoxifen (beginning 14dpi). 28dpi; n=6 (control) or 7 (cKO) mice. **v**, Co-expression of TGFβ-activating integrin pairs *Itgav* and *Itgb1, Itgb6,* or *Itgb8* (snRNAseq). **w-y,** Quantification of lesional Col1a1^{GFP+} fibroblast total density (**w**) and density within in inner core (**x**) or fibrotic border (**y**) in IgG- or ADWA11-treated mice. 14dpi; n=3 (IgG) or 4 (ADWA11) mice (2 slices averaged/mouse). **z-ac,** Lesion size (**z**, normalized per experiment), cortical monocytes (**aa**), and meningeal (**ab**) or blood neutrophils (**ac**) in IgG- and ADWA11-treated mice (14dpi). n=14 (IgG) or 13 (ADWA11) mice (**z**, 2 slices averaged/mouse); n=7 (IgG) or 8 (ADWA11) mice (**aa,ac**) or 6 (IgG) or 7 (ADWA11) mice (**ab**). **ad**, Itgb8^{TdT} mouse, with perilesional/astrocytic *TdT*, 14dpi (insets: GFAP/TdT colocalization, yellow). **ae**, Lesion size (14dpi) in hGfap^{cre}; Itgb8^{flox} mice and controls. n=12 (control) or 7 (cKO) mice (2 slices averaged/mouse); normalized to controls. **af-ah,** Control or Emx1^{cre}; Itgb8^{flox} lesional images (**af**), ER-TR7 coverage (**ag**), and lesion size (**ah**, normalized to controls). 14dpi. n=7 mice/group (2 slices averaged/mouse). Graphs show mean±s.d. ns=not significant, *p<0.05, **p<0.01, ***p<0.001, ****p<0.0001; * lesioned-control vs. lesioned-cKO; # lesioned-control vs. contralateral-control; † lesioned-cKO vs. contralateral-cKO (**i**); Student's T-test (**c-f,n,o,t,u,w-ac,ae,ag,ah**); two-way ANOVA, Sidak's post-test (**i** [repeated measures]; **j-m,r,s**). 14μm slices; images represent two or more mice.

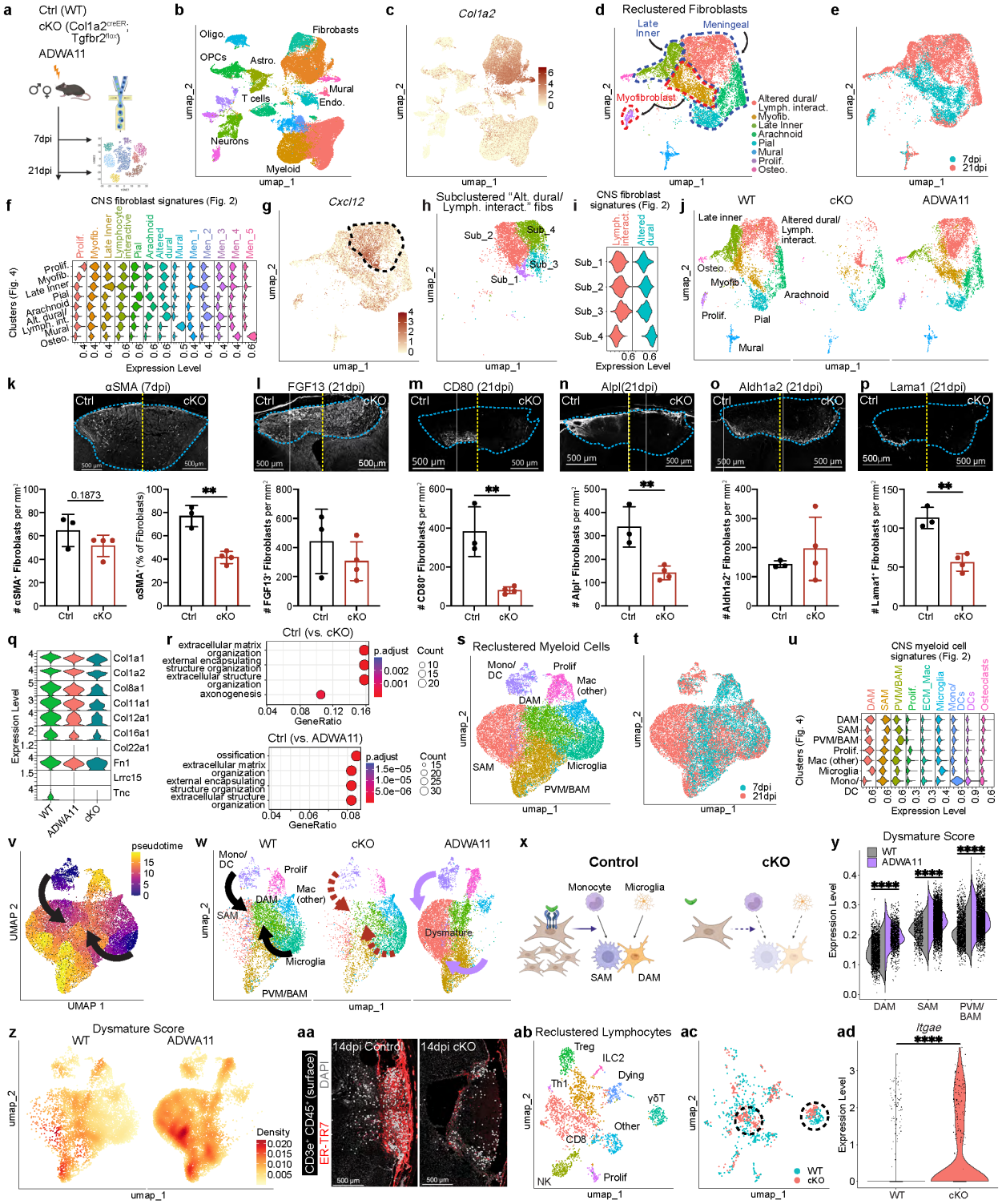


Fig. 13. Additional molecular characterization of injury response after fibroblast impairment. a, snRNAseq schematic. WT, cKO (Col1a2^{creER}; Tgfbr2^{flox}), and $\alpha_v\beta_8$-blocking antibody (ADWA11)-treated mice were harvested at 7 and 21dpi (2 mice per timepoint/condition), lesions were micro-dissected, and nuclei were sorted (DAPI$^+$) and *(Figure caption continued on the next page)*

(Figure caption continued from the previous page)
sequenced. **b-c**, Global UMAPs from snRNAseq data showing indicated cell types (**b**) or *Col1a2* expression (**c**). **d-e**, UMAPs showing fibroblast subclusters (**d**) or timepoint (**e**). **f**, Violin plots mapping "CNS fibroblast signatures" (derived from **Fig. 4**, x-axis) onto clusters identified in **d** (y-axis). **g-i**, Characterization of "Altered dural/lymphocyte interactive" fibroblasts, shown as highlighted cluster in *Cxcl12* feature plot (**g**), UMAP with subclusters (**h**), and violin plots showing subcluster expression of "Lymphocyte interactive" and "Altered dural" signatures (derived from **Fig. 4**), highlighting 3 lymphocyte-interactive-like and 1 altered-dural-like subcluster(s) (**i**). **j**, Fibroblast UMAP separated by condition, with pan-fibroblast reduction in cKO mice and late inner fibroblast reduction in $\alpha_v\beta_8$-blocked (ADWA11) mice. **k-p,** Images (top) and quantification (bottom) of fibroblast subset marker expression among Col1a2^{creER} R26^{TdT} fibroblasts in control or cKO mice. 7dpi cKOs show a decrease in αSMA$^+$ myofibroblasts (**k**, quantified as myofibroblast density [left] or proportion [right]). 21dpi cKOs show a trending decrease in Fgf13$^+$ late inner fibroblasts (**l**) and decreases in CD80$^+$ lymphocyte interactive fibroblasts (**m**), Alpl$^+$ altered dural fibroblasts (**n**), and Lama1$^+$ pial fibroblasts (**p**), though Aldh1a2$^+$ leptomeningeal/arachnoid fibroblasts are preserved (**o**). Blue dotted lines show lesion border. n=3 (control) or 4 (cKO) mice. **q,** Violin plots showing expression of myofibroblast-related genes among the myofibroblast cluster. **r,** Gene set enrichment among the myofibroblast cluster, with controls showing ECM-process enrichment. **S-t**, UMAPs showing myeloid cell subclusters (**s**) or timepoint (**t**). **u**, Violin plots mapping expression of "CNS myeloid cell signatures" (derived from **Fig. 4**, x-axis) onto clusters identified in **s** (y-axis). **v-w**, Pseudotime (**v**, Monocle3) and UMAP plots separated by condition (**w**) showing potential myeloid differentiation trajectories, including monocyte-to-SAM (top) and microglia-to-DAM (bottom), with monocytes and microglia as root states. **x**, Schematic showing effect of TGFβ-driven fibroblasts on SAM/DAM formation. **y-z**, Violin (**y**) or UMAP plots (**z**) showing "dysmature" transcriptional signature across conditions. n=1841/1281 (WT/ADWA11 DAM), 573/5551 (WT/ADWA11 SAM), or 1724/3181 (WT/ADWA11 PVM/BAM) nuclei (**y**). **aa**, Surfaced T cells (CD3e$^+$ CD45$^+$) in control and cKO mice, with fibroblast-rich (ER-TR7$^+$) lesion. **ab-ac**, UMAP showing lymphocyte subclusters (**ab**) or genotype (**ac**, WT and cKO). Dotted black lines highlight CD8 and $\gamma\delta$T cells. **ad**, Violin plot of lymphocyte *Itgae* expression. n=495 (WT) or 336 (cKO) nuclei. **p<0.01, ****p<0.0001; Student's T-test (k-o); Mann-Whitney test (**y,ad**). 14μm slices; images represent two or more mice.

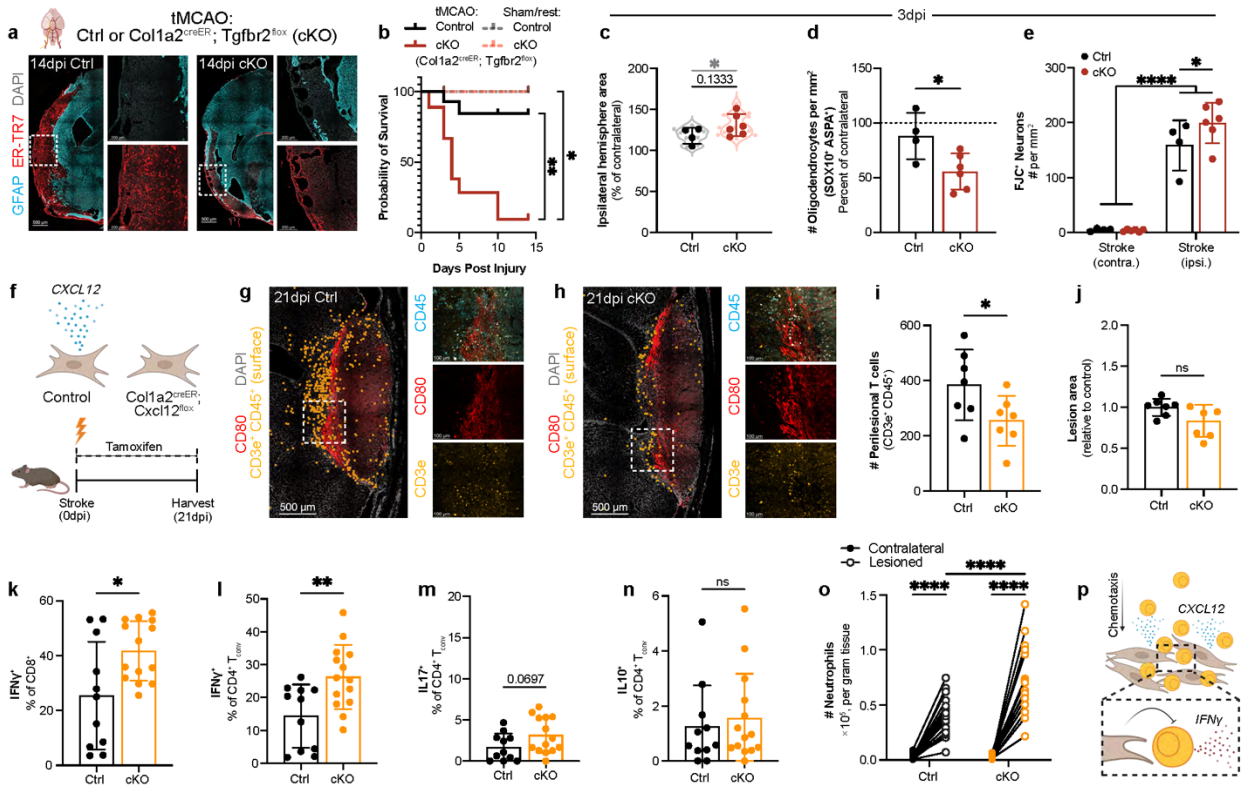


Fig. 14: Discrete beneficial functions of early myofibroblasts and late lymphocyte interactive fibroblasts. a-b, 14dpi fibrotic lesion (**a**) or survival (**b**) after tMCAO. n=14 (control tMCAO), 18 (cKO tMCAO), 6 (control sham/rest), or 10 (cKO sham/rest) mice (tamoxifen days -3-1, 2, 5, 8, 11). **c-e**, Quantification of ipsilateral hemisphere enlargement/edema (**c**), oligodendrocyte density (**d**), and FluoroJade C+ (degenerating) neuron density (**e**) in control or cKO brains at 3dpi (tMCAO). n=4 (control) or 6 (cKO) mice (in **c**, 2 slices averaged per mouse; slice values and statistics shown with lighter colors/smaller points). **f,** Schematic showing loss of CXCL12 production in Col1a2^{creER}; Cxcl12^{flox} cKO fibroblasts (control and cKO tamoxifen induction days 0-2, 7-9, 14-16). **g-j,** Surfaced images showing T cells (CD3e+ CD45+) and lymphocyte interactive fibroblasts (CD80+) in control **(g)** or *Cxcl12* cKO mice (**h**), with quantification of T cells (**i**) and lesion size (**j**, normalized to controls). 21dpi; n=7 mice/group (2 slices averaged/mouse). **k-n,** Expression of IFNγ among CD8+ T cells (**k**) and expression of IFNγ (**l**), IL17 (**m**), or IL10 (**n**) among CD4+ T cells. 21dpi; n=11 (control) or 14 (cKO) mice. **o**, Cortical neutrophils in control or *Cxcl12* cKO mice. 21dpi; n=21 (control) or 16 (cKO) mice. **p**, Schematic showing T cell chemotaxis and putative cytokine regulation mediated in part by late lesional fibroblast-derived CXCL12. Graphs show mean±s.d. *p<0.05, **p<0.01, ****p<0.0001; Log-rank (Mantel-Cox) test (**b**); Student's T-test (**c,d, i-n**); two-way repeated-measures ANOVA, Sidak's post-test (**e,o**). 14µm slices; images represent two or more mice.

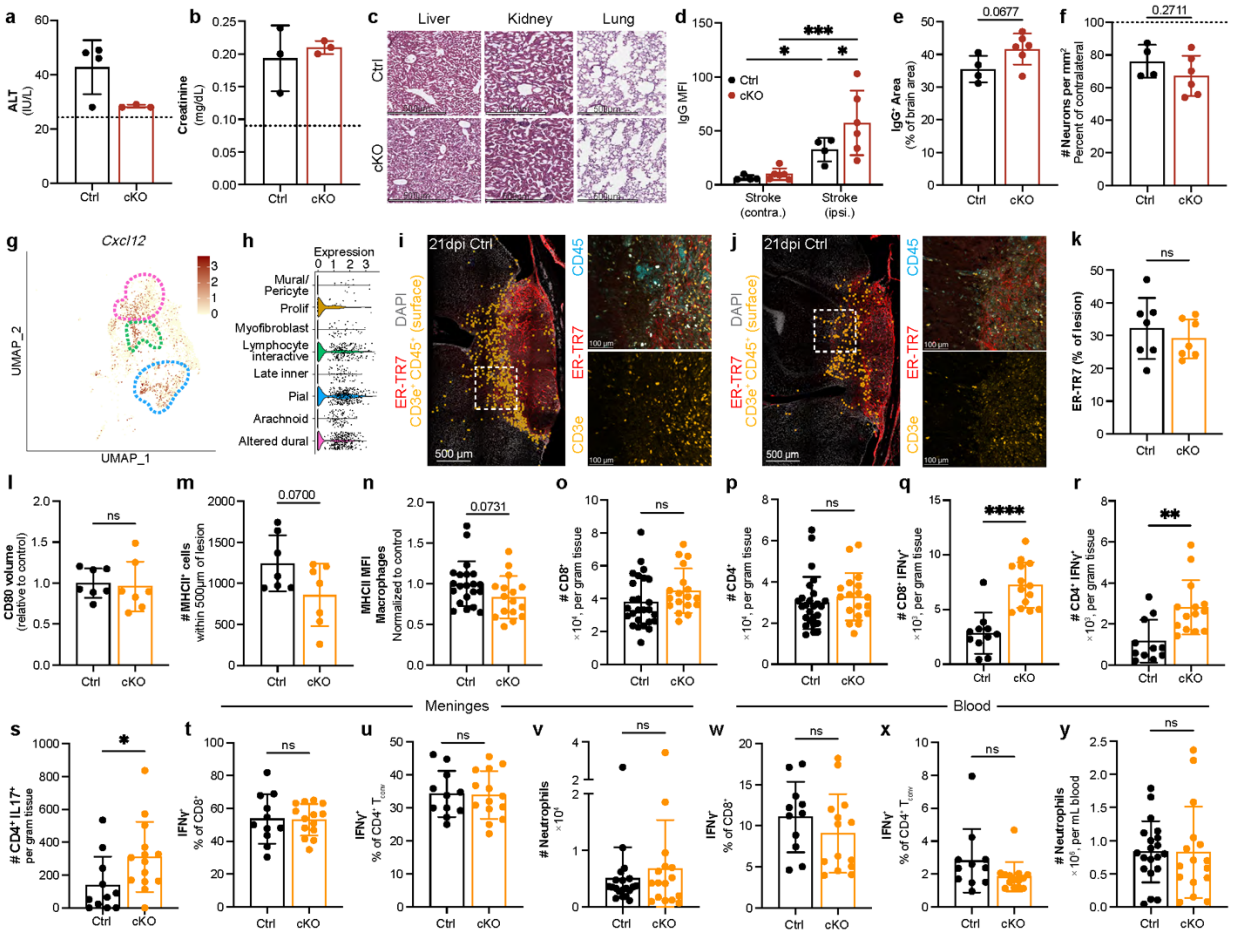


Fig. 15. Additional characterization of *Tgfbr2* and *Cxcl12* cKO mice. a-c, Serum levels of ALT (**a**) or creatinine (**b**) and hematoxylin and eosin staining of liver, kidney, and lung tissue (**c**) in control and cKO (Col1a2^{creER}; Tgfbr2^{flox}) mice without brain injury. n=4 (control [**a**]) or 3 (cKO [**a**], ctrl/cKO [**b**]) mice; images representative of n=2 mice/group (**c**). Dotted lines indicate lower bound of normal range. **d-f,** IgG MFI (**d**) and area of immunopositivity (**e**, normalized to brain area) or neuronal density (**f**) in control or cKO mice (3dpi, tMCAO). n=4 (control) or 6 (cKO) mice. **g-h**, Feature plot (**g**) or violin plot (**h**) showing *Cxcl12* expression among late fibroblast subsets including lymphocyte interactive, pial, and altered dural fibroblasts. **i-k,** Surfaced images showing T cells (CD3e$^+$ CD45$^+$) near ER-TR7$^+$ lesion in control (**i**) or *Cxcl12* cKO mice (**j**), with quantification of ER-TR7 coverage (**k**). 21dpi; n=7 mice/group. **l**, Volume of surfaced CD80$^+$ cells in control or *Cxcl12* cKO mice. 21dpi; n=7 mice/group. **m,** MHCII$^+$ cells within 500µm of lesion. 21dpi; n=7 mice/group. **n,** MHCII expression among (perilesionally enriched) macrophages, normalized to controls per experiment. 21dpi; n=21 (control) or 16 (cKO) mice. **o-s**, Quantification of total cortical CD8$^+$ (**o**) or CD4$^+$ (**p**) T cells, IFNγ$^+$ CD8$^+$ (**q**) or CD4$^+$ (**r**) T cells, or IL17$^+$ CD4$^+$ T cells (**s**). 21dpi; n=26 (control) or 18 (cKO) mice (**o,p**); n=11 (control) or 14 (cKO) mice (**q-s**). **t-y,** Expression of IFNγ among CD8$^+$ or CD4$^+$ T cells and neutrophil counts in meninges (**t-v**) or blood (**w-y**). n=11 (control) or 14 (cKO) mice (**t,u,w,x**); n=20 (control) or 16 (cKO) mice (**v,y**). *p<0.05, **p<0.01, ***p<0.001, ****p<0.0001; Student's T-test (**a,b,e,f,i,l-y**); two-way repeated-measures ANOVA, Sidak's post-test (**d**). 14µm slices; images represent two or more mice.

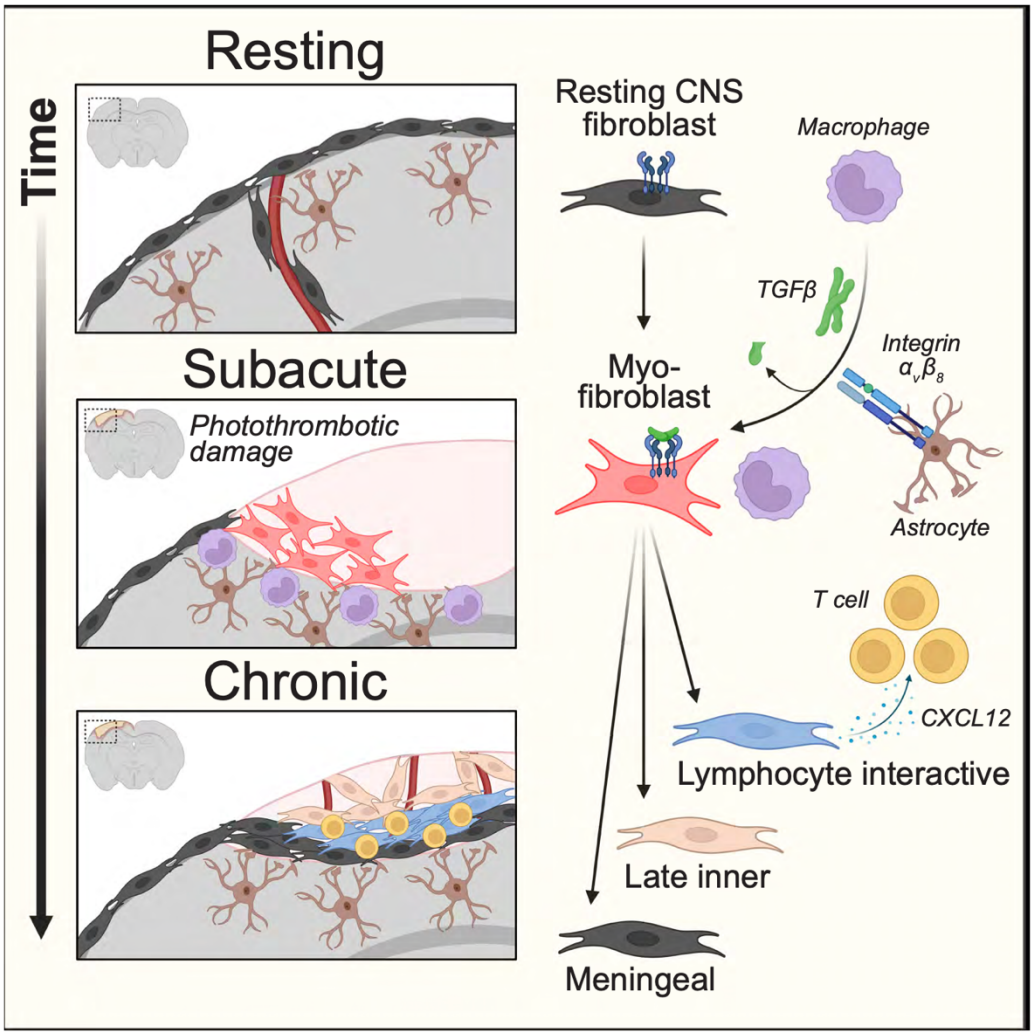


Fig. 16. Graphical Summary

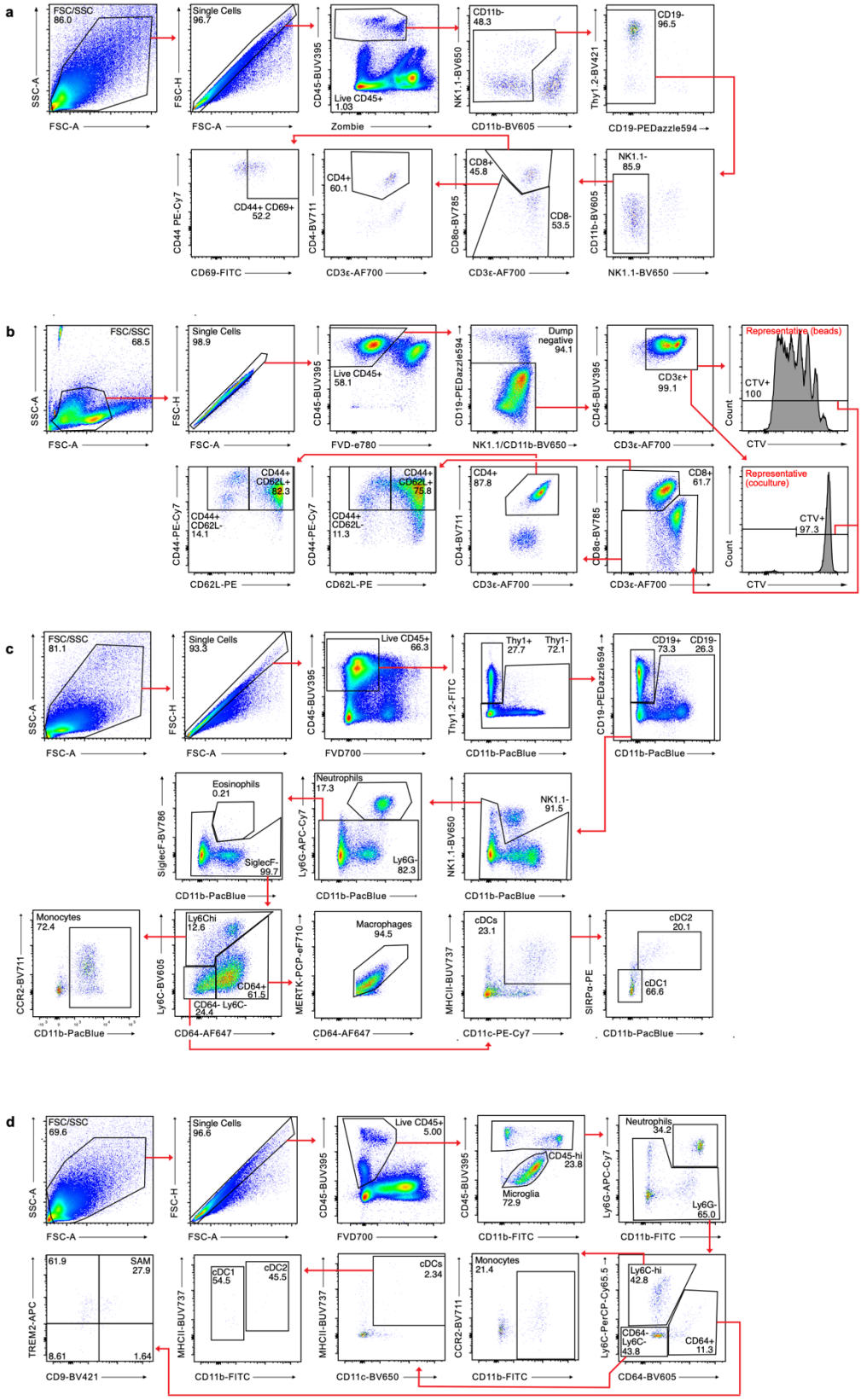


Fig. 17: Representative flow cytometry gating. a-d, Gating of T cells in cortical tissue
(Figure caption continued on the next page)

(Figure caption continued from the previous page)
(**a**), T cells in *ex vivo* coculture (**b**), myeloid cells in spleen (**c**), and myeloid cells in cortical tissue (**d**).

2.4 Supplemental files

2.4.1 Supplementary Video 1:

Whole lesion (PT injury, 14dpi, iDISCO) with fibroblasts and associated ECM.

2.4.2 Supplementary Video 2:

Thick section image (200μm, iDISCO; PT injury, 7dpi) showing vascular remodeling, with Pdgfrα^{GFP+} nuclei, marking both fibroblasts and oligodendrocyte precursor cells (OPCs), enriched in perivascular regions.

2.4.3 Supplementary Video 3:

Persistent *Cthrc1*-lineage^{+} fibroblasts and surrounding gliosis at 21dpi (14μm; PT injury, tamoxifen 0-21dpi).

2.5 Materials and methods

Mice

To lineage trace resting fibroblasts and track injury-responsive fibroblasts, we crossed Col1a2^{creERT2} mice (MGI 6721050, from Bin Zhou, Institute of Biochemistry and Cell Biology, Shanghai Institutes for Biological Sciences)[151] with Rosa26$^{TdT\text{-}Ai14}$ mice (R26-CAG-RFP, Jackson 007914) containing a flox-stop-flox sequence upstream of a CAG-RFP-WPRE cassette in the constitutively expressed ROSA26 locus. Tamoxifen induces RFP expression in *Col1a2*-lineage^{+} cells. Col1a2^{creERT2} mice were also crossed to Rosa26^{Sun1GFP} mice (Jackson 030952), enabling fibroblast nuclear identification. For dMCAO experiments, a distinct Col1a2^{creERT} allele was used (Jackson 029567). Additional stromal reporters used include Col1a1^{GFP} mice (from David Brenner, University of California, San Diego) to mark active *Col1a1*-expressing cells[152]; Pdgfra^{GFP} (PDGFRa-H2B-eGFP nuclear-localized GFP, Jackson 007669) to track fibroblasts and oligodendrocyte lineage cells[153,154]; and Rosa26$^{Tdt\text{-}Ai14}$ mice crossed to Gli1^{creERT2} mice (Jackson 007913) to track adventitial fibroblasts[42]; Twist2^{cre} mice (Jackson 008712) to track fibroblasts and mural cells[155]; Acta2^{creERT2} mice to track myofibroblasts and smooth muscle cells[156]; Ng2^{creER} mice (Ng2creER^{TM}, Jackson 008538) to mark pericytes and oligodendrocyte precursor cells[157]; Atp13a5^{creERT2} mice to mark pericytes[158]; and Cthrc1^{creER} mice (generously provided by Dean Sheppard) to track myofibroblasts[129].

To track immune cell subsets, we crossed Rosa26$^{TdT\text{-}Ai14}$ mice to CD4^{cre} mice (Jackson 022071) track CD4^{+} and CD8^{+} T cells[159]; Ccr2^{creERT2} mice (from Burkhard Becher, University of Zurich, Switzerland) to track monocyte-derived cells; P2ry12^{creERT2} (Jackson 034727) to track microglia-derived cells; Cx3cr1^{creER} (Jackson 020940) to track

macrophages; and PF4^{cre} (Jackson 008535) to track border associated macrophages. We also used T-bet (Tbx21)-zsGreen transgenic mice (generously provided by Jinfang Zhu, Lab of Immune System Biology, NIH)[160] to track type 1 lymphocytes. Cx3cr1^{creER} mice were additionally crossed with Tgfb1^{GFP} mice (MGI 3719583)[161] and Tgfb1^{flox} mice (Jackson 033001) to drive deletion of *Tgfb1* in macrophages (in Cx3cr1^{creER}; Tgfb1$^{GFP/flox}$ mice). Controls were littermate tamoxifen-induced, Cx3cr1^{creER}; Tgfb1$^{flox/+}$ mice.

To conditionally delete fibroblast *Tgfbr2*, we crossed Col1a2^{creERT2} mice to Tgfbr2^{flox} mice (both Tgfbr2-exon2^{flox}, MGI 2384513[162], and Tgfbr2-exon4^{flox}, Jackson 012603). To conditionally delete fibroblast *Cxcl12,* we crossed Col1a2^{creERT2} to Cxcl12^{flox} mice (Jackson 021773). We used Itgb8^{TdT} mice (Itgb8-IRES-TdT, generously provided by Helena Paidassi)[163] to visualize *Itgb8* expression. We used Itgb8^{flox} mice (MGI 3608910)[164] crossed to Emx1^{cre} mice (Jackson 005628) or hGfap^{cre} mice (Jackson 004600), to delete *Itgb8* from neurons and glial cells[140,165,166]; some hGfap^{cre} mice were crossed to iSure^{cre} (MGI 6361135[167]) to optimize *Cre* efficiency. For above conditional knockout strains, controls were tamoxifen-induced (when relevant), littermate Cre-negative or flox-heterozygous mice; cohoused non-littermate lineage tracers for select experiments involving fibroblast quantification; or age-matched, uninduced non-littermate controls for select tMCAO experiments. Additionally, to enable depletion of myofibroblasts, we crossed Cthrc1^{creER} mice to Rosa26^{DTA} mice; controls were littermate cre-positive vehicle-treated (saline or corn oil) or cre-negative tamoxifen-induced mice.

Mice were mixed gender animals backcrossed on C57BL/6 for at least 10 generations, or on a mixed genetic background (Gli1^{creERT2}, Cx3cr1^{creER}, Emx1^{cre}). If not otherwise stated, all experiments were performed with 7-21 week old male and female

mice. All mice were bred and maintained in specific-pathogen-free conditions at the animal facilities of UCSF or UCSD and were used in accordance with institutional guidelines and under study protocols approved by the UCSF or UCSD Institutional Animal Care and Use Committee (protocols AN193180-01J, AN195716-01B [UCSF], s14044 [UCSD]).

Marmoset

n=11 outbred middle-aged marmoset monkeys (*Callithrix jacchus;* >5 years; median age ~7 years) were used in this study. No siblings were used. Animals were housed in family groups (12:12 hrs light/dark cycle, temperature 31°C, humidity 65%). Experiments were conducted according to the Australian Code of Practice for the Care and Use of Animals for Scientific Purposes and were approved by the Monash University Animal Ethics Committee. Marmosets were obtained from the National Nonhuman Primate Breeding and Research Facility (Monash University, Australia).

Tamoxifen-induced Cre recombination

Mice were injected i.p. with 200μL of tamoxifen (Sigma-Aldrich) dissolved in corn oil at 10mg/mL. For transcranial activation, 4-OH-tamoxifen (Sigma-Aldrich), the active metabolite of tamoxifen[168], was dissolved in acetone at 100μg/mL. 100μL of 4-OHT was applied to a specific cranial location, determined stereotactically as described below ("Photothrombotic injury"). Tamoxifen was applied via micropipette (approximately 5μL at a time) and allowed to evaporate in between applications.

Photothrombotic injury

For PT injury surgeries[169–171], mice were anesthetized via inhaled isoflurane, shaved on the scalp, and stereotaxically fixed. After sterilization with iodine and 70%

ethanol, 0.5% lidocaine was administered subcutaneously to the scalp. The cranium was surgically exposed, and a fiber optic white light is placed over the S1 cortex (3.0mm, -0.5mm (x,y) from bregma, with coordinates determined via stereotax). Mice were injected intraperitoneally with 8mg/kg Rose Bengal dye; after 1 minute, the cranium was exposed to high intensity white light (150W) for 2 minutes. The scalp was sutured using nylon sutures and surgical glue, and buprenorphine was administered.

TBI

For TBI surgeries[20], mice were anesthetized and stereotaxically fixed, as above. A 3-mm craniotomy was performed over the right S1 centered at –1 mm posterior from bregma, +3 mm lateral from the midline. TBI was performed with a CCI device (Impact One Stereotaxic Impactor for CCI, Leica Microsystems) equipped with a metal piston using the following parameters: 3 mm tip diameter, 15° angle, 0.8 mm depth from the dura, 3 m/s velocity, and 100 ms dwell time. Sutures were administered as above.

tMCAO

Mice (age P25-45) underwent focal ischemia-reperfusion with transient right middle cerebral artery occlusion (tMCAO) for 3 hours, or sham surgery, as detailed previously[172–174]. Briefly, the right internal carotid artery (ICA) was dissected, and a temporary ligature was tied using a strand of 6-0 suture at its origin. This ligature was retracted laterally and posteriorly to prevent retrograde blood flow. A second suture strand was looped around the ICA above the pterygopalatine artery and an arteriotomy was made proximal to the isolated ICA. A silicone coated 6-0 nylon filament from Doccol Corporation (Sharon, MA, USA) was inserted 6.5-7 mm to occlude the MCA and the second suture strand was tied off to secure the filament for the duration of occlusion.

Injury was confirmed by severe left frontal/hindlimb paresis resulting in circling movements during the occlusion period. For reperfusion, each animal was anesthetized and all suture ties and the occluding filament were removed. Avitene Microfibrillar Collagen Hemostat (Warwick, RI, USA) was placed over the arteriotomy and the skin incision was closed. According to pre-established criteria, litters displaying excessive bleeding at time of reperfusion were excluded. Litters with significantly underweight mice (less than 85% of expected weight at time of surgery) were excluded from survival analysis. Sham animals were anesthetized for 15 minutes, equivalent to surgery procedure time; at the time of reperfusion, the sham animals were once again anesthetized for 5 minutes, equivalent to the reperfusion procedure time for tMCAO animals.

dMCAO

dMCAO surgeries were performed as previously described[175]. Briefly, mice were sedated with isoflurane and analgesic administered before surgery. An incision was made between the eye and ear, the temporal muscle retracted, and the skull removed above the distal middle cerebral artery (dMCA). The dMCA was then occluded with a bipolar coagulator which clots the artery, reducing blood flow to the ipsilateral cortex. Following this procedure, the incision was closed and mice monitored daily.

Marmoset stroke

Induction of focal stroke to the marmoset primary visual cortex (V1) was performed by vasoconstrictor-mediated vascular occlusion of the calcarine branch of the posterior cerebral artery (PCAca), as detailed previously[176,177]. Briefly, following anesthesia (Alfaxalone 5mg/kg; maintained with inspired isoflurane 0.5-4%), a craniotomy and dural

thinning was performed, followed by intracortical injections of endothelin-1 (ET-1; 0.1µl/30s pulse at 30s intervals, totaling ~0.7 µL over 7 sites) proximal to the PCAca, which supplies operculum V1. The craniotomy was replaced, secured with tissue adhesive (Vetbond; 3M) and the skin sutured closed. Monkeys recovered for 7 days (n=2), 6 weeks (n=2) and 1 year (n=2; equal sex).

Liposome injection

Clodronate liposomes or empty control liposomes (Encapsula Nanoscience) were randomly assigned and administered intraperitoneally, beginning with injection 3 days prior to injury (200µL) followed by injection on the day of injury (100µL) and every 3 days subsequently (100µL) until harvest (14dpi).

Antibody injection

ADWA11[178,179] (generously provided by Dean Sheppard) or IgG1 isotype control (InVivoMab) was randomly assigned, diluted in sterile DPBS to 10mg/kg, and injected intraperitoneally on the day of injury (0dpi) and every week subsequently until harvest (7dpi, etc.).

EdU injection

To measure proliferation, 5-ethynyl-2'-deoxyuridine (EdU, Thermo Scientific) was reconstituted at 5mg/mL in DPBS and injected at 50mg/kg i.p. Mice were injected either every other day throughout the injury timecourse or 2 hours prior to sacrifice.

Tissue processing: imaging (mouse)

Following CO_2 euthanasia, mice were transcardially perfused with 10mL of DPBS and 10mL of 4% PFA (Thermo Scientific). Skullcaps/brains were removed from bases. Skullcaps (meningeal imaging) or skullcaps/brains were fixed overnight (4% PFA, 4°C).

Skullcaps/brains were washed (DPBS) and decalcified in 0.3M EDTA (VWR) (1 week, 4°C) followed by cryoprotection (30% sucrose). When removed from skullcaps, brains were cryoprotected directly after fixation. Brains were frozen in O.C.T. (Thermo Scientific) on dry ice and sliced to indicated thickness on a cryostat (Leica). Spinal cords processed similarly (decalcifying intact vertebra). For spatial transcriptomics, tissue processing was performed as above, without PFA perfusion/fixation. Brains were removed from skullcaps and directly frozen. For quantitative imaging of (blinded) PT lesions, 2 14μm sections were collected per 100μm sliced, and sections representing a lesion's maximal cross-sectional area were stained, imaged, and quantified. Lesion size outliers (diameter <25% of normal, representing technical errors during injury) were excluded prior to unblinding, resulting in one exclusion from **Fig. 10g,h,** and one exclusion from **Fig. 10p, Fig. 12ad**. Mice with hydrocephalus were also excluded.

Tissue processing: imaging (marmoset)

For immunofluorescence, naïve controls (n=2; equal sex) and post-stroke marmosets were administered an overdose of pentobarbitone sodium (100mg/kg; intraperitoneal). Following apnea, animals were transcardially perfused with 0.1M heparinized PBS, followed by 4% paraformaldehyde (PFA) in PBS (0.1M). Brains were dissected, post-fixed and cryoprotected, as outlined previously[131,176,177]. Following separation of the hemispheres, each hemisphere was bisected coronally at the start of the caudal pole of the diencephalon and frozen in liquid nitrogen at -40°C. Tissue was cryosectioned in the parasagittal plane at -20°C to obtain 40μm for free-floating sections stored in cyroprotectant solution (50% PBS 0.1M, 20% ethylene glycol, 30% glycerol).

IHC

Slide-mounted thin sections were thawed, washed (DPBS), and blocked (1 hour, DPBS/0.4% TritonX-100/5% secondary-host serum). For select antibodies, antigen retrieval was performed prior to blocking, involving a) incubation for up to 15 minutes in L.A.B. solution (Liberate Antibody Binding Solution, Polysciences) followed by a 5 minute wash in PBS (ASPA), or b) incubation for 3 (Aldh1a2 [thin section only], Alpl, α-SMA [thin section only], FGF13, Laminin, SEMA3C, CDH18) or 5 minutes (cCasp3) in 0.01M $Na_3C_6H_5O_7$ (heated to 95°C in a water bath), followed by cooling to room temperature (20 minutes) and 3 washes in PBS (5 minutes each). Samples were then incubated in primary antibodies diluted in blocking solution (room temperature, 1 hour, or 4°C, overnight). Samples were washed (DPBS/0.05% TritonX-100, 5 minutes, 3 times) and incubated in secondary antibodies diluted 1:1000 in blocking solution (room temperature, 45-60 minutes). Samples were washed, mounted in DAPI Fluoromount-G (Thermo Scientific), and imaged. Proliferation was measured using the Click-iT EdU Alexa Fluor 647 Imaging Kit (Thermo Fisher), according to the manufacturer's instructions (in between primary and secondary staining steps). Fluoro-Jade C was stained using the Fluoro-Jade C Ready-to-Dilute Staining Kit (VWR), according to the manufacturer's instructions.

Medium-thickness sections (30-50μm) were blocked in 250μL DPBS/0.25% TritonX-100/5% secondary-host serum (1 hour, room temperature). Samples were subsequently incubated in primary antibody diluted in blocking solution (4°C, overnight), washed (DPBS/0.05% TritonX-100, 5 minutes, 4 times), and incubated in secondary antibodies diluted 1:500 in blocking solution (room temperature, 45-60 minutes). Samples were washed 3 times, mounted in DAPI Fluoromount-G, and imaged.

Meninges were blocked and stained before removal from skullcaps (block: 4°C, overnight, in 2mL DPBS/0.3% TritonX-100/5% FBS/0.5% BSA/0.05% NaN_3). Samples were incubated in primary antibody diluted in 600μL of staining solution (DPBS/0.15% TritonX-100/7.5% FBS/0.75% BSA/0.075% NaN_3; 4°C, 72 hours), washed (DPBS/0.15% TritonX-100, 4°C, 30 minutes, 3 times), and incubated in secondary antibodies diluted 1:400 in staining solution solution (4°C, 24 hours). Samples were washed and incubated in 10μg/mL DAPI in PBS (room temperature, 1 hour). Dural meninges were subsequently microdissected from skullcap, mounted in 50-100μL of Refractive Index Matching Solution (RIMS, DPBS/Histodenz [133.33g/100mL]/0.017% Tween-20/0.17% NaN_3), and imaged.

Thick sections (100-200μm) were stained using the iDISCO protocol[180] with 1-2 days of permeabilization, 1-2 days of blocking, 3 days of primary antibody, and 3 days of secondary antibody.

For marmoset imaging, free-floating sections comprising the infarct and peri-infarct regions were selected and washed in PBS (0.1M) and pre-blocked in a solution of 10% normal goat serum in PBS + 0.3% Triton X-100 (TX; Sigma) before incubation with primary antibodies overnight at 4°C. Sections were rinsed in 0.1% PBS-Tween and incubated with secondary antibodies (1 hour). After washes in PBS, sections were treated with DAPI, mounted in Fluoromount-G, and imaged.

For H&E imaging, histology was performed by HistoWiz Inc. (histowiz.com) using a Standard Operating Procedure and fully automated workflow. Samples were processed, embedded in paraffin, and sectioned at 4μm. Immunohistochemistry was performed on a Bond Rx autostainer (Leica Biosystems) with enzyme treatment (1:1000) using standard protocols. Bond Polymer Refine Detection (Leica Biosystems) was used according to the

manufacturer's protocol. After staining, sections were dehydrated and film coverslipped using a TissueTek-Prisma and Coverslipper (Sakura). Whole slide scanning (40x) was performed on an Aperio AT2 (Leica Biosystems).

Imaging Antibodies

Primary antibodies used for murine imaging include chicken anti-GFP (Aves Labs GFP-1020, 1:200), rabbit anti-dsRed (Takara 632496, 1:300), chicken anti-GFAP (Invitrogen PA1-10004, 1:200), rat anti-GFAP (2.2B10, Invitrogen 13-0300, 1:200), rat anti-ER-TR7 (Novus Biologicals NB100-64932, 1:200), rabbit anti-αSMA (Abcam ab5694, 1:300), rat anti-CD31 (MEC13.3, Biolegend 102514, 1:200), goat anti-Desmin (GenWay Biotech GWB-EV0472, 1:200), goat anti-Decorin (Novus Biologicals AF1060, 1:200), goat anti-Collagen 1 (Southern Biotech 1310-01, 1:200), rabbit anti-Collagen 6α1 (Novus Biologicals NB120-6588, 1:200), rat anti-Periostin (345613, Novus Biologicals MAB3548, 1:200), rat anti-ICAM1 (YN1/1.7.4, Biolegend 116110, 1:200), syrian hamster-anti-CD3ε (500A2, BD Biosciences 553238, 1:200), goat anti-S100A8 (R&D Systems AF3059, 1:200), chicken anti-NeuN (Millipore Sigma ABN91, 1:200), rabbit anti-Iba1 (Aif3, Fujifilm Wako 019-19741, 1:200-1:1000), mouse anti-FGF13 (N235/22, Invitrogen MA5-27705, 1:100), goat anti-CD80 (R&D Systems AF740, 1:200), goat anti-Alpl (Novus Biologicals AF2910, 1:50), rabbit anti-Laminin (Millipore Sigma L9393-100UL, 1:25), rabbit anti-SEMA3C (Invitrogen PA5-103168, 1:100), rabbit anti-CDH18 (Invitrogen PA5-112902, 1:50), rabbit anti-Aldh1a2 (Novus Biologicals NBP2-92915, 1:200), goat anti-SOX10 (R&D Systems AF2864, 1:300), rabbit anti-ASPA (Genetex GTX113389, 1:1000), mouse anti-E-Cadherin (Clone 36, BD Biosciences 610181), rat anti-I-A/I-E (MHCII, M5/114.15.2, eBioscience 14-5321-82), and rabbit anti cleaved Caspase 3 (Cell Signaling

Technology 9661T, 1:400). For marmoset imaging, rabbit anti-COL6 (Abcam ab6588, 1:500) was used.

Secondary antibodies were used as necessary at protocol-specific concentrations, conjugated to AF488, AF555, AF594, and AF647 (Life Technologies, Thermo-Fisher).

Confocal and widefield microscopy

Confocal images (for thick sections, immune cell quantification, and some thin sections) were imaged using a Nikon A1R laser scanning confocal including 405, 488, 561, and 650 laser lines for excitation and imaging with 16X/0.8 NA Plan Apo long working distance water immersion, 20X/0.95 NA XLUM PlanFl long working distance water immersion, or 60X/1.2 NA Plan Apo VC water immersion objectives. Z steps were acquired every 4μm. Widefield images (for thin sections, fibrosis quantification, and lesion size quantification) were imaged using a Zeiss Axio Imager.M2 widefield fluorescent microscope with a 10X/0.3 or 20X/0.8 air objective, or on a Leica Aperio Versa 8 Slide Scanner with a HC PL APO 20X/0.75 CS2 air objective. Marmoset images were acquired using the VS200 slide scanner (Olympus).

Image analysis/quantification

z-stacks were rendered in 3D and quantitatively analyzed using Bitplane Imaris v9.8 software package (Andor Technology PLC, Belfast, N. Ireland). Individual cells (e.g., lymphocytes, fibroblasts, etc.) or fibrotic and glial scars were annotated using the Imaris surface function, thresholding on fluorescent signal (based on antibody staining or reporters when available), along with additional co-stains (e.g., CD45, Iba1, CD3e), DAPI staining, and size/morphological characteristics; when helpful, background signal in unrelated channels was excluded. 3D distances between lymphocytes and stromal/glial

cells were calculated using the Imaris Distance Transform Matlab extension. Proportions of immune or stromal cells within given cortical/lesional regions were determined by manually tracing regional borders (e.g., GFAP/ER-TR7) and filtering immune cell surfaces based on inclusion. Additional surface statistics were calculated using Imaris. Lesion sizes were calculated in Fiji (ImageJ version 1) by tracing the fibroblast-astrocyte border (using ER-TR7 and/or GFAP). Fibroblast or myeloid cell coverage was determined by thresholding the relevant channel (e.g., ER-TR7), using a consistent threshold for each slice except for cases of exceptionally high tissue background. Coverage was calculated as thresholded area normalized to lesion area, and data was subsequently unblinded. For pooled data, equivalent thresholds were applied across experiments when possible, with exceptions made for varying tissue background. Border thickness was calculated in Fiji, using a macro to calculate the distance between each (manually traced) border edge at points 100μm apart, followed by averaging these distances.

Serum chemistries:

Serum analysis was performed by the Unit for Laboratory Animal Medicine Pathology Core (University of Michigan). Whole blood was collected into serum separator tubes, allowed to clot, and separated into serum by centrifugation. Serum chemistries were run on an AU480 chemistry analyzer (Beckman Coulter Inc.).

Tissue Processing: Visium

Tissue was collected from 1 resting mouse, 1 2dpi mouse, 2 7dpi mice, and 4 21dpi mice (including 2 Cthrc1^{creER}; R26^{DTA} mice, discarded after initial clustering due to undetectable deletion; PT injury). Tissue was collected as above. 10μm slices were prepared via cryostat and directly mounted onto Tissue Optimization and Spatial Gene

Expression slides (10X Genomics). Tissue optimization was carried out as per manufacturer's recommendations, resulting in an optimal tissue permeabilization time of 12 minutes. Tissue mounted on the Spatial Gene Expression slide was processed as per manufacturer's recommendations, imaged on a Leica Aperio Versa slide scanner at 20X, and transferred to the Gladstone Genomics Core for library preparation according to the manufacturer's protocol. Samples were subsequently transferred to the UCSF Center for Advanced Technology for sequencing on the NovaSeq 6000 system.

Tissue processing: nuclear isolation (murine)

Nuclear isolation was employed to overcome limitations of traditional flow cytometry and/or scRNAseq, including ECM interference with fibroblast isolation and dissociation signatures that disproportionately affect stromal and immune cells[181]. For nuclear flow cytometry, tissue was collected from resting, 7, or 14dpi (PT injury) $Pdgfra^{GFP}$ mice. For single nuclear RNA sequencing experiment 1 (timecourse), tissue was collected from 2 wildtype mice per timepoint (1 male and 1 female) at rest, 2dpi, 7dpi, and 21dpi. 2 mice/timepoint with impaired TGFβ signaling ($Col1a2^{creER}$; $Tgfbr2^{flox}$ and $Cdh5^{creER}$; $Tgfbr2^{flox}$) were harvested at 7/21dpi but were discarded after initial clustering and not analyzed separately due to insufficient yield. Alternatively, for single nuclear RNA sequencing experiment 2, tissue was collected from 2 WT mice, 2 $Col1a2^{creER}$; $Tgfbr2^{flox}$ mice, and 2 ADWA11-treated mice at 7 and 21dpi (1 male and 1 female per timepoint/condition).

Following CO_2 euthanasia, mice were transcardially perfused (10mL DPBS) and decapitated. Brains were removed from skullcaps and placed in iMED+ (15mM HEPES [Fisher] and 0.6% glucose in HBSS with phenol red)[182]. For nuclear flow cytometry and

single nuclear RNAseq experiment 1 (timecourse), dura, lesion, and perilesional cortex (with or without contralateral cortex) were microdissected and processed separately. For RNAseq experiment 2 (WT, cKO, and ADWA11), only lesions were dissected. Microdissection involved meningeal/skullcap separation, removal of subcortical structures, and separation of lesions from skullcaps (lesions often separate from cortex during initial dissection but can be micro-dissected as necessary). For snRNAseq, tissue from male and female mice within experimental conditions was combined.

Tissue was processed using ST-based buffer protocol[181], with the following modifications: initial centrifugation was performed at 500g for 10 minutes. After lysis/initial centrifugation, nuclei were resuspended in 1mL ST buffer (nuclear flow cytometry, RNAseq experiment 2) or PBS/1% BSA/0.2UμL Protector RNAse inhibitor (Roche) (RNAseq experiment 1), filtered through 35μm cell strainers, and subsequently processed as below.

For nuclear flow cytometry and single nuclear RNAseq experiment 2, nuclei were centrifuged for 5 minutes at 500g, resuspended in FANS buffer (DPBS/1% BSA/0.1mM EDTA)[183] with 2μg/μL DAPI and 0.2U/μL RNase inhibitor (snRNAseq), and stained (nuclear flow) or sorted (snRNAseq).

For single nuclear RNAseq experiment 1, cell counts were performed after initial centrifugation (NucleoCounter, Chemometic), and a maximum of $2x10^6$ nuclei were multiplexed using CellPlex Multiplexing technology (10X Genomics) according to the manufacturer's instructions (using protocol 1 for nuclear multiplexing, with only one wash after multiplexing to increase yield). Nuclei were resuspended in FANS buffer with 0.2U/μL RNase inhibitor and 2μg/μL DAPI and nuclear concentrations were determined.

Immediately before sorting, multiplexed microanatomical regions (including lesion, parenchyma, and dural meninges) from individual mice were combined at desired ratios (75% lesion, 25% parenchyma). Nuclei were sorted (forward and side scatter and DAPI) into pre-coated tubes containing 200μL PBS/1% BSA/0.2U/μL RNase inhibitor (BDFACSAria II sorting system, 100μm nozzle size, 4 way-purity sort mode). Resting dural fibroblasts were enriched using $Col1a2^{creER}$; $Rosa26^{Sun1GFP}$ and resting nuclei were combined after sorting (50% GFP^+ meninges, 25% GFP^- meninges, 25% parenchyma).

After sorting/pooling (snRNAseq), samples were centrifuged (500g, 15 minutes), and supernatant was removed to leave a minimum final volume of 45μL with a maximum of 16,500 nuclei. Final nuclear concentrations were acquired, and samples were transferred to the UCSF Genomics CoLab for library preparation. Up to 1.6×10^4 nuclei were loaded onto the Chromium Controller (10X Genomics). Chromium Single Cell 3' v3.1 reagents were used for library preparation according to the manufacturer's protocol. Libraries were transferred to the UCSF Institute for Human Genetics for sequencing on the NovaSeq 6000 system.

Tissue processing: nuclear isolation (marmoset)

For single-nuclei RNA sequencing (snRNAseq), naïve control marmosets (n=3; 1 female, 2 male; median age 4Y) were administered an overdose of pentobarbitone sodium (100 $mg.kg^{-1}$; intraperitoneal). Following apnea, frontal lobes were recovered and dissected under aseptic conditions in sterile ice-cold phosphate buffered saline (PBS; 0.1M; pH 7.2). Tissues were and snap frozen in isopentane chilled in liquid nitrogen. The procedures/ dissections were performed in chilled RNAase-free PBS with RNase-free sterilized instruments under RNase-free conditions. Approximate time from apnea to

snap-freezing ranged from 20-30 minutes. All 6 samples passed QC. Nuclear isolation was performed as described previously[131], involving pulverization in liquid nitrogen, lysis in lysis buffer, dounce homogenization, and gradient purification. After isolation, nuclei were counted and diluted to 1 million/mL with sample-run buffer (0.1% BSA, RNAse inhibitor [80U/mL], 1mM DTT in DPBS). snRNAseq was performed on the 10x Genomics Chromium System. Cellranger commercial software was utilized to conduct initial data processes including sequence alignment to the marmoset genome (CalJac3).

Tissue processing: single cell isolation (murine)

Single cell suspensions were prepared from tissues including brain, spinal cord, meninges, blood, and spleen. Immediately following CO_2 euthanasia, spleens were removed into RPMI/10% FBS and peripheral blood was collected through the right ventricle into heparin tubes. Mice were subsequently transcardially perfused through the left ventricle with 10mL of DPBS, decapitated, and brains were carefully removed from skullcaps and placed in iMED+ as above[182]. For select experiments, spinal cords were carefully dissected from vertebra. Cortex, lesion, and meninges were dissected as above. Brain was weighed and subsequently homogenized in iMED+ homogenized using a 2mL glass tissue grinder (VWR; 6 plunges, followed by filtration through a 70μm filter, addition of 2mL iMED+, and 6 more plunges). Filtered suspensions were centrifuged at 220g for 10 minutes and resuspended in 5mL of 22% Percoll (GE Healthcare) in Myelin Gradient Buffer (5.6mM $NaH_2PO_4 \cdot H_2O$, 20mM $Na_2HPO_4 \cdot 2H_2O$, 140mM NaCl, 5.4mM KCl, 11mM glucose in H_2O)[182]. 1mL of PBS was layered on top of Percoll. Samples were centrifuged at 950g for 20 minutes at 4°C with no break to separate myelin and resuspended in FACS buffer. Dissected meninges were incubated in digestion medium (RPMI/10%

FBS/80μg/mL DNase I/40μg/mL Liberase TM (Roche)). Tissue was subsequently mashed through 70μm filters, followed by centrifugation and resuspension in FACS buffer. Spleens were prepared by mashing tissue through 70μm filters without tissue digestion, followed by centrifugation. Red blood cells were lysed for 2 minutes using 1X Pharm-Lyse and the remaining cell pellet were resuspended in FACS buffer. Blood samples were centrifuged for 5 minutes at 500g. Pellets were resuspended in 1X Pharm-Lyse 5 minutes at room temperature, followed by centrifugation and suspension in FACS buffer. For cytokine restimulation assays, samples were transferred to U-bottom plates and incubated in stimulation medium (RPMI supplemented with 10% FBS, 1% penicillin/streptomycin, 1X Glutamax (Thermo Scientific), 1X HEPES buffer (Fisher), 1X non-essential Amino Acids (Thermo Scientific), 1mM $NaC_3H_3O_3$ (Thermo Scientific), 55μM b-mercaptoethanol, 1X Cell Stimulation Cocktail (Tonbo), and 1X Brefeldin A (Thermo Scientific)) at 37°C for 3 hours, followed by centrifugation and transfer to a V-bottom plate.

Flow cytometry

Resuspended samples were stained in 96-well V-bottom plates. Surface staining was performed at 4°C for 45 minutes in 50μL staining volume. For experiments involving intra-cellular staining (including transcription factor and cytokine staining), cells were fixed and permeabilized using Foxp3 Transcription Factor Staining Buffer Set (eBioscience) followed by staining at 4°C for 1 hour in 50μL staining volume. All samples were acquired on a BD LSRII Fortessa Dual or a BD FACSAria II for cell sorting. Live cells or nuclei were gated based on their forward and side scatter followed by Zombie NIR fixable (Biolegend 423106), Fixable Viability Dye eF780 (eBioScience 65086514), Draq7 (Biolegend

424001), or DAPI (40,6-diamidine-20-phenylindole dihydrochloride; Millipore Sigma D9542-10MG) exclusion (or inclusion for nuclei). Lineages were subsequently identified as follows:

Oligodendrocyte-lineage nuclei were identified as DAPI^{+}, Pdgfra$^{GFP\text{-}hi}$, Olig2^{+}. Fibroblast nuclei were identified as DAPI^{+}, Pdgfra$^{GFP\text{-}int}$ or DAPI^{+}, Col1a2^{creER}; Rosa26$^{Sun1GFP+}$ (snRNAseq experiment 1, resting dural meninges). Bulk nuclei were identified as DAPI^{+}. Global lymphocytes were defined as CD45^{+}, Thy1^{+}. T cells were identified as CD45^{+}, CD11b^{-}, CD19^{-}, NK1.1^{-}, CD3ε^{+}, CD4^{+} (CD4 T cells), or CD8α^{+} (CD8 T cells), and were further defined as CD44^{+}, CD69^{+} (resident memory T cells, TRM), CD62L^{+} (naïve T cells), CD62L^{-}, CD44^{+} (activated T cells), or CTV^{diluted} (proliferating T cells). Additionally, CD4 T cells were defined as T-bet^{+} (Th1 T cells), Gata3^{+} (Th2 T cells), or RORγt^{+} (Th17 T cells), or cytokine-positive or negative (IFNγ, IL17A, IL10). Neutrophils were defined as CD45^{+}, CD11b^{+}, Ly6G^{+} (and optionally Thy1^{-}, CD19^{-}, NK1.1^{-}). Monocytes were defined as CD45^{+}, CD11b^{+}, Ly6G^{-}, Ly6C^{+} (and optionally Thy1^{-}, CD19^{-}, NK1.1^{-}, Siglec F^{-}). Microglia were defined as CD45^{int}, CD11b^{+}. Macrophages were defined as CD45^{+}, Ly6G^{-}, Ly6G^{-}, CD64^{+} (optionally MERTK^{+}). Microglia/macrophages were further defined as Disease Associated Microglia/Scar Associated Macrophages (DAM/SAM, CD9^{+} and CD63^{+}/TREM2^{+}). cDCs were identified as CD45^{+}, Ly6G^{-}, Ly6C^{-}, CD64^{-}, MHCII^{+}, CD11c^{+}, and were further defined as cDC1s (CD11b^{lo}, optionally SIRPα^{-}) or cDC2s (CD11b^{hi}, optionally SIRPα^{+}). B cells were defined as CD45^{+}, Thy1^{-}, CD19^{+}. Eosinophils were defined as CD45^{+}, Thy1^{-}, CD19^{-}, NK1.1^{-}, Ly6G^{-}, CD11b^{+}, Siglec F^{+}. Populations were back-gated to verify purity and gating.

Data were analyzed using FlowJo software (TreeStar, USA) and compiled using Prism (Graphpad Software). Cell counts were performed using flow cytometry counting beads (CountBright Absolute; Life Technologies) per manufacturer's instructions.

Flow cytometry Antibodies

Antibodies used for flow cytometry include rabbit anti-Olig2 (Thermo P21954**),** anti CD45 (30-F11, BD Biosciences 564279 or Biolegend 103132 or 103104), anti-CD90.2 (Thy1, 53-2.1, Biolegend 140327, BD Biosciences 553004), anti-CD11b (M1/70, Biolegend 101224 or BD Biosciences 563015), anti-CD19 (6D5, Biolegend 115554), anti-NK1.1 (PK136, Biolegend 108736), anti-CD3ε (17A2, Biolegend 100216), anti-CD4 (RM4-5, Biolegend 100557, or GK1.5, BD Biosciences 563050), anti-CD8α (53-6.7, Biolegend 100750), anti-CD44 (IM7, Biolegend 103030), anti-CD69 (H1.2F3, Biolegend 104505), anti-CD62L (MEL-14, Biolegend 104407), anti-Tbet (4B10, Biolegend 25-5825-80), anti-Gata3 (TWAJ, eBioscience 12-9966-41), anti-RORγt (B2D, eBioscience 17-6981-82), anti-Ly6G (1A8, Biolegend 127624), anti-IFNγ (XMG1.2, Biolegend 505810), anti-IL17A (TC11-18H10.1, Biolegend 506922), anti-IL10 (JES5-16E3, eBioscience 12-7101-81), anti-Ly6C (HK1.4, Biolegend 128011 or 128035), anti-CD64 (X-54-5/7.1, Biolegend 139323 or BD Biosciences 558539), anti-MERTK (DS5MMER, eBioscience 46-5751-80), anti-CD9 (KMC8, BD Biosciences 564235), anti-TREM2 (237920, R&D systems FAB17291A), anti-CD63 (NVG-2, Biolegend 143904), anti-I-A/I-E (MHCII, M5/114.15.2, BD Biosciences 748845), anti-CD11c (N418, Biolegend 117339 or 117318), anti-CD172a (SIRPα, P84, eBioscience 12-1721-80), anti-Siglec-F (E50-2440, BD Biosciences 740956), anti-Podoplanin (gp38, 8.1.1, Biolegend 127412), anti-CD31 (390, Biolegend 102404 or 102408), anti-EpCAM (G8.8, Biolegend 118230), anti-PDGFRa

(APA5, Biolegend 135908), anti-Sca-1 (Ly-6A/E, D7, Biolegend 108131), and anti-phosphoSmad3 (EP823Y, Abcam ab52903).

Ex vivo coculture

For *ex vivo* coculture experiments, lesions and contralateral cortex were dissected as described above and divided into halves or equivalently sized sections (contralateral cortex). Tissue was added to 96-well round bottom plates in 100μL of R10 (RPMI supplemented with 10% FBS, 1% penicillin/streptomycin, 1X Glutamax (Thermo Scientific), and 55μM b-mercaptoethanol).

For myeloid cell cocultures, single cell suspensions from perilesional (ipsilateral) cortex were generated and stained as above. Homeostatic microglia (negative for DAM markers, i.e., CD9, CD63) were sorted into pre-coated tubes containing 3mL R10 (BDFACSAria II sorting system, 100μm nozzle size, 4 way-purity sort mode) and checked for purity post-sort. Cells were subsequently counted, and a maximum of $1x10^7$ cells were labeled with 5mM CellTrace CFSE in PBS (Thermo Scientific) for 10 minutes, followed by washing with R10, centrifugation, and resuspension at $4.5x10^4$ cells/mL. 100μL of suspension (containing 45,000 microglia) was subsequently plated with lesions or alone.

For T cell cocultures, T cells were isolated from spleens and cervical/inguinal lymph nodes using EasySep Magnetic Bead negative selection (Stem Cell), according to the manufacturer's instructions (using 31.5μL of vortexed selection beads). A maximum of $1x10^7$ T cells were labeled with 5mM CellTrace Violet in PBS (Thermo Scientific) for 10 minutes, followed by washing with R10, centrifugation, and resuspension at $1x10^6$ cells/mL. 100μL of suspension (containing 100,000 T cells) was subsequently plated with lesions, control tissue, or alone. As a positive control, anti-CD3/CD28 T cell activating

DynaBeads (Thermo scientific) were magnetically washed in 1mL DPBS and added to T cells at a 1:1 ratio.

For purified fibroblast cocultures, meninges were processed as above. Lungs were perfused, dissected, and digested in PBS with Dispase II (15u/mL), Collagenase 1 (22,500U/mL), and DNAse 1 (10mg/mL) for 30 minutes at 37°C, followed by centrifugation, filtration, and RBC lysis as above. Endothelial and hematopoietic cells were negatively selected using magnetic beads per manufacturers' instructions. After staining as above, fibroblasts were sorted as Lineage$^-$ PDGFRa$^+$ gp38$^+$ (meningeal) or PDGFRa$^+$ gp38$^+$ Sca1$^+$ (lung adventitial), plated at up to 15,000 per well in a flat bottom 96 well plate, and cultured for 7 days prior to initiation of lymphocyte coculture, as above.

Plates were incubated at 37°C, 5% CO_2 for 72 hours. After coculture completion, wells were mixed by pipetting and cells were transferred to a V-bottom plate, and blocked, stained, and analyzed as above. For cocultured wells, CTV or CFSE staining was used to identify plated (vs. lesion-resident) T cells or microglia; given the low rates of proliferation observed, gates were gates chosen to maximize exclusion of unlabeled cells while still including proliferating/CTV-diluting cells (up to at least 3 rounds of division). **Fig. 8s** and **Fig. 9t-v** include pooled control data from experiments where wildtype lesions were cultured with diphtheria toxin (100ng/mL; any lesions expressing Rosa26^{DTR} were excluded), empty liposomes, or IgG1 isotype control (BioXCell). For direct comparisons between 7dpi and 21dpi lesions, media refeeding was performed daily (replacing 100µL, 2x) to mitigate rapid media acidification by 7dpi lesions.

Vascular permeability and hemorrhage analysis

Vascular permeability was measured using Evans Blue extravasation[184]. Briefly, Evans Blue (1% in saline) was injected i.p. (8mL/kg) 3 hours prior to sacrifice. Following euthanasia, mice were transcardially perfused (10mL DPBS), and mice that did not show appropriate liver clearing were excluded. Brains were dissected as above, whole hemispheres were weighed and added to 250 or 500μL formamide, and tissue was incubated for 44-48 hours to extract Evans Blue. Evans Blue fluorescence was measured on a SpectraMax microplate reader (excitation 620nm, emission 680nm). A standard curve (4-point logistic regression) was used to calculate extravasated mass, which was subsequently normalized to tissue weight.

To quantify hemorrhage/bleeding, photographs were taken of frozen brains during slicing (1 photograph per 100-150μm). Representative photographs were chosen from across the lesion volume for quantification (3 photographs per brain). Regions of overtly visible blood (corresponding to erythroid cell accumulation, as visible by microscopy) were traced in Fiji, followed by normalization to lesion area (traced via tissue discoloration) and averaging per animal.

Visium data processing

Sequencing data were aligned to mouse genome mm10 with SpaceRanger version 2.0.0 (10x Genomics). Data was processed using the Seurat R package, version 4.2.1[185]. Individual capture areas were processed using Seurat's *SCTransform* function to normalize data, select variable features for dimensionality reduction, and scale data. Capture areas were subsequently merged for further analysis. Principle components were calculated using Seurat's *RunPCA* function, followed by graph-based clustering using Seurat's *FindNeighbors* (dims =1:30) and *FindClusters* (res = 0.8) functions and 2D

visualization using Seurat's *RunUMAP* function (dims = 1:30). Feature and spatial feature plots, violin plots, and UMAP plots were generated using Seurat. We used *FindAllMarkers* to identify markers for each cluster (test.use = MAST, min.pct = 0.05, logfc.threshold = 0.2) and generated resulting dot plots using Seurat. Fibroblast-containing clusters were identified via expression of *Col1a1* and further investigated using feature plots and spatial feature plots. One large cluster (cluster 10) was subclustered using Seurat's *FindSubCluster* function (res = 0.5); subcluster 10_0 was identified as a 7dpi fibroblast-enriched cluster and selected for further analysis based on expression of *Pdgfra*. Cluster 8 was identified as a 21dpi fibroblast-enriched cluster.

Analyzing WT tissue, we used Seurat's *FindMarkers* function (min.pct = 0.05, logfc.threshold = 0.2) to determine markers for cluster 10_0 and 8 and used the EnhancedVolcano R package to visualize relevant DEGs (*EnhancedVolcano* function, minfc = 1.15, alpha = 0.05)[186]. To calculate fibroblast TGFβ scores, we utilized a previously generated bulk sequencing dataset of primary lung fibroblasts treated with TGFβ (1ng/mL) or PBS for 48 hours[187]. TGFβ-upregulated genes were identified from normalized data (log2FC > 0, q < 0.05). Module scores were generated using Seurat's *AddModuleScore* function. To calculate proliferation scores, we utilized a proliferation signature composed of 23 genes (*Ccnb1, Ccne1, Ccnd1, E2f1, Tfdp1, Cdkn2b, Cdkn1a, Plk4, Wee1, Aurkb, Bub1, Chek1, Prim1, Top2a, Cks1, Rad51l1, Shc, Racgap1, Cbx1, Mki67, Mybl2, Bub1, Plk1*)[188,189].

Murine snRNAseq data processing

Sequencing data were aligned to mouse genome mm10 with CellRanger version 7.1.0 (snRNAseq experiment 1; timecourse) or version 7.2.0 (snRNAseq experiment 2;

WT, cKO, and ADWA11) (10x Genomics). Data was processed using the Seurat R package, version 4.2.1 (experiment 1) or 5.0.1 (experiment 2). We excluded cells with high mitochondrial gene expression and low or high UMI and feature counts, using the bottom and top 2.5 percentiles as our cutoff. We used Seurat's *SCTransform* function to normalize data, select variable features for dimensionality reduction (with the removal of certain sex-related and mitochondrial genes), and scale data. Principle components were calculated using Seurat's *RunPCA* function, followed by graph-based clustering using Seurat's *FindNeighbors* (dims =1:30) and *FindClusters* (res = 0.5) functions and 2D visualization using Seurat's *RunUMAP* function (dims = 1:30). We used *FindAllMarkers* (test.use = MAST, experiment 1) or *RunPrestoAll*[190] (experiment 2) to identify markers for each cluster (min.pct = 0.05, logfc.threshold = 0.2) and annotated clusters using select common and well-validated lineage marker genes (e.g., *Col1a1, Col1a2, Pgdfra* [fibroblasts]; *Cspg4* [mural]; *Itgam* [myeloid]; *P2ry12, Sall1* [microglia]; *Cd3e, Cd4, Cd8* [T cells]; *Rbfox3* [neurons]; *Dcx, Prom1* [neural progenitors]; *Gfap, Aldh1l1* [astrocytes]; *Mbp, Olig2, Sox10* [oligodendrocytes]; *Olig2, Sox10, Pdgfra* [oligodendrocyte precursor cells]; and *Pecam1* [endothelial cells]). We identified and excluded 2 clusters made up of likely doublets based on gene expression and excluded 1 sample due to insufficient nuclear yield (experiment 1), visualizing resultant clusters on UMAPs and dot plots using Seurat. Final datasets comprised 28,187 cells including 8,096 fibroblasts; 189 mural cells; 4,568 myeloid cells/microglia; 548 T cells; 11,216 neurons; 2,026 astrocytes; 537 oligodendrocytes; 94 oligodendrocyte precursor cells; 470 endothelial cells; 259 neural progenitor cells; and 184 unassigned nuclei (experiment 1); or 18,455 fibroblasts; 496 mural cells; 24,302 myeloid cells/microglia; 2,271 T cells; 5,994 neurons; 2,781

astrocytes; 1,669 oligodendrocytes; 2,399 oligodendrocyte precursor cells; and 1,703 endothelial cells (experiment 2). We subsequently subset the data to wildtype cells for downstream analysis (experiment 1). Additional feature plots, UMAP plots and dot plots, and heatmaps were generated using Seurat. Joint densities for gene combinations (including published meningeal layer signatures)[75] were visualized using the NebulosaPlot R package (*plot_density* function)[191] and modified using the ScCustomize R package (*Plot_Density_Custom* function)[192].

Fibroblasts and immune cells were subset and reclustered as above (immediately prior to WT subsetting [experiment 1]; res = 0.5 [experiment 1] or 0.2 [experiment 2] for fibroblasts, res = 0.15 [experiment 1] or 0.25 [experiment 2] for immune cells) and DEGs were recalculated. Clusters expressing high levels of myeloid or neuronal genes were excluded as likely contaminants and removed from global UMAP and bar plots. For experiment 1, resting dural meningeal fibroblasts were removed (by microanatomical metadata and cluster) for downstream analysis. For experiment 2, clusters were annotated by expression of previously defined CNS fibroblast or myeloid cell "signatures" generated from experiment 1 DEG marker lists (visualized using *AddModuleScore* and violin plots). Dural fibroblasts were subclustered (*FindSubCluster* function) to identify lymphocyte-interactive and dural subsets. Relative abundance across time was calculated for each fibroblast and macrophage subcluster after normalizing for timepoint or condition sample size (i.e., total # nuclei). Gene ontology analysis was performed using the ClusterProfiler R package for gene set testing (*enrichGO* function)[193]. Ligand-receptor and ligand-signaling-network interactions underlying myofibroblast emergence were interrogated using the NicheNetR R package[194]. Beginning with the global Seurat object,

fibroblasts were treated as “receiver” cells, with resting fibroblasts as the “reference condition” and 7dpi myofibroblasts as the “condition of interest.” Potential “sender” cells were any cells present at rest, 2, or 7dpi. Integration of single nuclear and Visium data was performed using the SpaceXR package[195] (to deconvolute individual spots) and using Seurat’s *AddModuleScore* function (to score each Visium cluster with marker sets for single nuclear fibroblast clusters). Multi-gene scores were calculated as follows and generated using *AddModuleScore.* Myofibroblast (fibroblast TGFβ) scores were calculated as above. Profibrotic “SAM scores” were generated as published previously, using a combination of 6 genes (*Trem2*, *Cd9*, *Spp1*, *Gpnmb*, *Fabp5*, and *Cd63*).[62] Disease Associated Microglia (“DAM”) scores were generated using the top 30 published markers specific to DAM ($p < 0.001$, ranked by logFC)[95]. Dysmaturity scores were generated using genes significantly upregulated in microglia from $Emx1^{cre}$; $Itgb8^{flox}$ mice (relative to controls; bulk sequencing data accessed via the GEO and analyzed with originally described parameters)[138]. Macrophage-fibroblast ligand-receptor interactions were interrogated and visualized using CellPhoneDB (Version 4, statistical method)[196]. Pseudotime trajectories for myeloid cells were generated using the monocle3 R package v1.3.4 (*learn_graph* and *order_cells* functions), with homeostatic microglia and monocytes chosen as 2 possible roots. Phylogenetic trees were calculated using Seurat’s *BuildClusterTree* function.

Marmoset snRNAseq data processing

Processed data from 7dpi marmosets (ET1-induced stroke)[131] and resting marmosets (unpublished) was generously provided by the J. Bourne lab. Fibroblasts from both datasets were identified via COL1A1 expression, subset, and integrated using the

Seurat *FindIntegrationAnchors* and *IntegrateData* functions (dims = 1:30). The integrated data was subsequently rescaled, PCAs were calculated, clusters were identified, and marker genes were selected as above. UMAP plots, barplots, and heatmaps of selected fibrosis-related genes were generated using Seurat. Myofibroblast (fibroblast TGFβ) scores were calculated as above.

Human TBI snRNAseq data processing

Human TBI snRNAseq data was accessed via the GEO[132]. Datasets representing individual patients were merged, and quality control was performed on mitochondrial expression, UMI counts, and gene counts, as above. We used Seurat's *SCTransform* function to normalize data, select variable features for dimensionality reduction (with the removal of certain sex-related and mitochondrial genes), and scale data. Principle components were calculated using Seurat's *RunPCA* function, followed by batch correction using Harmony[197], graph-based clustering, and cluster identification as above (res = 0.1). After cluster annotation, fibroblasts were identified via COL1A1 expression and subset. Heatmaps and violin plots were generated using Seurat. Myofibroblast (fibroblast TGFβ) scores were calculated as above.

Human GBM scRNASeq data processing

Human GBM data was generously provided by the M. Aghi lab[35]. QC was performed in accordance with the original publication (excluding cells with mt.percent > 20% and fewer than 200 or more than 20,000 UMIs). We used Seurat's *SCTransform* function to normalize data, select variable features for dimensionality reduction (with the removal of certain sex-related and mitochondrial genes), and scale data. Principle components were calculated using Seurat's *RunPCA* function, followed by graph-based

clustering and cluster identification as above (res = 0.1). After cluster annotation, fibroblasts were identified via COL1A1 expression, subset, and reclustered as above (res = 0.6). UMAP plots, feature plots, and heatmaps were generated using Seurat. Myofibroblast (fibroblast TGFβ) scores were calculated as above.

Statistical analysis

All data were analyzed by comparison of means using unpaired (unless otherwise noted) two-tailed Student's t-tests; for multiple comparisons, one-way or two-way ANOVA (with Tukey or Sidak's post hoc test) were used as appropriate (Prism, GraphPad Software, La Jolla, CA). ns = not significant, *p<0.05, **p<0.01, ***p<0.001, ****p<0.0001. Figures display means ± standard deviation (SD) unless otherwise noted. When possible, results from independent experiments were pooled. All data points reflect individual biological mouse replicates, unless otherwise noted. For all experiments, analysis was performed in at least three mice from at least two independent experiments unless otherwise noted (e.g., RNA sequencing).

2.6 Manuscript information

Data availability

Spatial and single nuclear transcriptomic data generated in this paper are deposited in Gene Expression Omnibus (GEO) (accession number will be released at the time of publication). Accession codes for 7dpi Marmoset data (Boghdadi et al.)[131], human TBI data (Garza et al.)[132], and human GBM data (Jain et al.)[35] can be found in the referenced studies.

Code availability

All original code generated to analyze RNA sequencing data is available at GitHub ("https://github.com/newingcrystal/CNS_Fibroblasts").

Acknowledgments

We thank Dr. Richard Locksley for his constructive feedback on this manuscript, as well as the UCSF Parnassus Flow Core RRID:SCR_018206 and DRC Center Grant NIH P30 DK063720, the UCSF Biological Imaging and Development Core (BIDC), the UCSF Genomics CoLab, the UCSF Institute for Human Genetics, the Gladstone Histology & Light Microscopy Core (HLMC), the Gladstone Genomics Core, the Monash Histology Platform, the University of Michigan University for Laboratory Animal Medicine Pathology Core, and Histowiz, Inc. for instruments and services. T.T. is supported by the NHLBI (NIH K99/R00HL155786). L.T. and J.A.B. are supported by the National Health and Medical Research Council (NHMRC; Australia; APP20140228) and The Yulgilbar Foundation Fund to JAB. The Australian Regenerative Medicine Institute is supported by the State Government of Victoria and the Australian Government. J.T.P. is supported by the NINDS (NIH R01NS096369). F.F.G. is supported by the NINDS (NIH R01NS107039).

D.S. is supported by the NHLBI (NIH R01HL142568). T.D.A. is supported by the NINDS (NIH R01NS119615-01). J.T.P., A.B.M., and A.V.M. are supported by the NINDS (NIH R01NS126765), UCSF PBBR grant, and UCSF Dept. of Lab Medicine discretionary funds; A.B.M. is additionally supported by the NIAID (NIH R01AI162806).

Competing interests

D.S. and UCSF hold patents on the uses of antibodies that block integrin $\alpha_v\beta_8$. D.S. is a founder of Pliant Therapeutics and has received research funding from Abbvie, Pfizer, and Pliant Therapeutics. D.S. serves on the Scientific Review Board for Genentech, and on the Inflammation Scientific Advisory Board for Amgen. The remaining authors declare no competing interests.

Lead contact

Further information and requests for resources and reagents should be directed to and will be fulfilled by the Lead Contact, Ari B. Molofsky (ari.molofsky@ucsf.edu).

CHAPTER 3: CLOSING AND FUTURE DIRECTIONS

In this dissertation, I have identified and characterized a fibroblast response to brain injury across several injury models and mammalian species. I defined a stereotyped fibroblast state transition from early myofibroblasts to late states including lymphocyte interactive fibroblasts. I showed that perilesional profibrotic myeloid cells – including both monocyte- and microglia-derived cells – promote the early myofibroblast response, in part through TGFβ production. Meanwhile, I implicated perilesional glial integrins in activating TGFβ and enabling fibroblast expansion. Attenuation of a full myofibroblast response via disruption of TGFβ sources, activators, or receptors caused impaired wound healing and/or exacerbated neuroinflammation, which correlated with exacerbated mortality in a severe stroke model. Finally, late lymphocyte-interactive fibroblasts played a distinct role in regulating lymphocyte positioning and immune tone.

The brain has classically been considered a fibro-privileged organ; fibroblasts have only been recently appreciated as relevant cell types in injury, and the full extent of their contribution to healing has not been characterized. Thus, while the fibroblast wound-healing programs identified here resemble processes seen in peripheral organ (e.g., skin) wound healing, where TGFβ-driven myofibroblast populations are also critical for tissue repair[6], the identification of this program in the brain (and the dissection of molecular pathways involving brain-resident cells) is a novel addition to the fields of neuroscience and brain injury. Additionally (and conversely), while the brain-specific insights gained from this dissertation are valuable, the brain is also an ideal model organ for studying fibroblast biology more generally. The brain is a sterile environment with relatively few resting fibroblasts or pre-existing stromal-immune niches; as such, our studies may help

dissociate the impacts of microbial signals and/or pre-existing tissue fibroblasts that are abundant in resting barrier sites (e.g., skin, intestine, respiratory tract, genitourinary tract).

Several open questions remain, with a view towards expanding our understanding of both wound healing after brain injury and fibroblast-immune biology more broadly. It will be critical to fully understand not only the molecular states inhabited by fibroblasts, but also the individual signals regulating transitions between states. Is TGFβ sufficient for the acquisition of a myofibroblast identity and fibroblast expansion after brain injury, as it seems to be in the periphery, or are other signals required to overcome fibro-privilege? Induced expression of constitutively active TGFβ signaling machinery will help answer this question. What signals drive the loss of the myofibroblast state and acquisition of late (e.g., lymphocyte-interactive) states? In the setting of cancer, several groups have identified myofibroblast-like cancer-associated fibroblasts (myCAFs) driven by TGFβ and a separate population of inflammatory CAFs (iCAFs) driven by IL-1β[59,198,199]. Is IL-1β similarly involved in the loss of a myofibroblast phenotype and acquisition of a lymphocyte-interactive phenotype? Or are other signals, potentially including withdrawal of local TGFβ, involved? Careful investigation with mouse genetic tools will enable these questions to be tested; single nuclear RNA sequencing and/or immunofluorescent imaging using our state-specific markers will be essential for detecting changes in fibroblast state dynamics.

Additionally, further investigation is required to fully define the lymphocyte niches observed after injury. What additional signals, besides CXCL12, are required for formation and maintenance of these long-lasting fibroblast-lymphocyte niches? Do they include additional chemokines, survival signals, proliferative signals, and/or effects on

lymphocyte metabolism via modulation of microenvironmentally available nutrient sources? *Ex vivo* approaches may prove useful for high throughput screens of candidate signals. Future work should also investigate potential effects of long-lived lymphocyte niches. Are fibroblasts anatomically and phenotypically restraining a lymphocyte population that would otherwise cause damage and exacerbate chronic neuroinflammation? In this case, lymphocyte-interactive fibroblasts might be an injury-induced check on autoimmunity. Alternatively, are lymphocytes recruited to physically weakened border regions to patrol for antigens and prevent opportunistic infections? This model is consistent with the resemblance of lymphocyte-interactive fibroblasts to dural fibroblasts, which recruit T cells engaged in homeostatic immune surveillance of the CNS[68]. Testing these questions will require manipulation of T cells and/or fibroblast niches in settings of exacerbated autoimmunity (e.g., genetic backgrounds involving autoreactive TCRs) or infection. Moreover, as with fibroblasts, the relative dearth of homeostatic lymphocytes will enable the dissociation of injury-induced lymphocyte responses from tissue-resident immune populations and processes present in most peripheral organs. A full understanding of these responses will enable the design of targeted therapies, with a view towards modulating chronic immune-driven sequelae of stroke (potentially including neurodegeneration[87]), and will further our understanding of stromal-immune interactions underlying a broad swathe of disease states.

REFERENCES

1. Gao, Z. *et al.* Restoring After Central Nervous System Injuries: Neural Mechanisms and Translational Applications of Motor Recovery. *Neurosci Bull* **38**, 1569–1587 (2022).
2. Iadecola, C., Buckwalter, M. S. & Anrather, J. Immune responses to stroke: mechanisms, modulation, and therapeutic potential. *J Clin Invest* **130**, 2777–2788 (2020).
3. Fehily, B. & Fitzgerald, M. Repeated Mild Traumatic Brain Injury. *Cell Transplant* **26**, 1131–1155 (2017).
4. Kirschenbaum, D. *et al.* Time-resolved single-cell transcriptomics defines immune trajectories in glioblastoma. *Cell* (2023) doi:10.1016/j.cell.2023.11.032.
5. Demirci, Y. *et al.* Brain Regeneration Resembles Brain Cancer at Its Early Wound Healing Stage and Diverges From Cancer Later at Its Proliferation and Differentiation Stages. *Front Cell Dev Biol* **10**, 813314 (2022).
6. Hu, K. H. *et al.* Transcriptional space-time mapping identifies concerted immune and stromal cell patterns and gene programs in wound healing and cancer. *Cell Stem Cell* **30**, 885-903.e10 (2023).
7. Dhandapani, S. S., Manju, D. & Mahapatra, A. K. The economic divide in outcome following severe head injury. *Asian J Neurosurg* **7**, 17–20 (2012).
8. Al-Qazzaz, N. K., Ali, S. H., Ahmad, S. A., Islam, S. & Mohamad, K. Cognitive impairment and memory dysfunction after a stroke diagnosis: a post-stroke memory assessment. *Neuropsychiatr Dis Treat* **10**, 1677–1691 (2014).

9. Neumann, D. & Lequerica, A. Cognitive Problems After Traumatic Brain Injury. *Archives of Physical Medicine and Rehabilitation* **96**, 179–180 (2015).
10. Rabinowitz, A. R. & Levin, H. S. Cognitive Sequelae of Traumatic Brain Injury. *Psychiatr Clin North Am* **37**, 1–11 (2014).
11. Englander, J., Cifu, D. X. & Diaz-Arrastia, R. Seizures after Traumatic Brain Injury. *Arch Phys Med Rehabil* **95**, 1223–1224 (2014).
12. Cruz-Haces, M., Tang, J., Acosta, G., Fernandez, J. & Shi, R. Pathological correlations between traumatic brain injury and chronic neurodegenerative diseases. *Translational Neurodegeneration* **6**, 20 (2017).
13. Brett, B. L., Gardner, R. C., Godbout, J., Dams-O'Connor, K. & Keene, C. D. Traumatic Brain Injury and Risk of Neurodegenerative Disorder. *Biol Psychiatry* **91**, 498–507 (2022).
14. Emberson, J. *et al.* Effect of treatment delay, age, and stroke severity on the effects of intravenous thrombolysis with alteplase for acute ischaemic stroke: a meta-analysis of individual patient data from randomised trials. *The Lancet* **384**, 1929–1935 (2014).
15. Hacke, W. *et al.* Thrombolysis with Alteplase 3 to 4.5 Hours after Acute Ischemic Stroke. *New England Journal of Medicine* **359**, 1317–1329 (2008).
16. Yiannopoulou, K. G. & Papageorgiou, S. G. Current and Future Treatments in Alzheimer Disease: An Update. *J Cent Nerv Syst Dis* **12**, 1179573520907397 (2020).

17. Fernandes, C. *et al.* Current Standards of Care in Glioblastoma Therapy. in *Glioblastoma* (ed. De Vleeschouwer, S.) (Codon Publications, Brisbane (AU), 2017).
18. Heindl, S. *et al.* Chronic T cell proliferation in brains after stroke could interfere with the efficacy of immunotherapies. *Journal of Experimental Medicine* **218**, (2021).
19. Alawieh, A., Zhao, J. & Feng, W. Factors affecting post-stroke motor recovery: Implications on neurotherapy after brain injury. *Behav Brain Res* **340**, 94–101 (2018).
20. Stephanie S. Holden *et al.* Complement factor C1q mediates sleep spindle loss and epileptic spikes after mild brain injury. *Science* **373**, eabj2685 (2021).
21. Sofroniew, M. V. & Vinters, H. V. Astrocytes: biology and pathology. *Acta Neuropathologica* **119**, 7–35 (2010).
22. Zehendner, C. M. *et al.* Traumatic brain injury results in rapid pericyte loss followed by reactive pericytosis in the cerebral cortex. *Scientific Reports* **5**, 13497 (2015).
23. Yokota, K. *et al.* Periostin Promotes Scar Formation through the Interaction between Pericytes and Infiltrating Monocytes/Macrophages after Spinal Cord Injury. *The American Journal of Pathology* **187**, 639–653 (2017).
24. Dias, D. O. *et al.* Reducing Pericyte-Derived Scarring Promotes Recovery after Spinal Cord Injury. *Cell* **173**, 153-165.e22 (2018).
25. Göritz, C. *et al.* A Pericyte Origin of Spinal Cord Scar Tissue. *Science* **333**, 238 (2011).
26. Kelly, K. K. *et al.* Col1a1+ perivascular cells in the brain are a source of retinoic acid following stroke. *BMC Neuroscience* **17**, 49 (2016).

27. Makihara, N. *et al.* Involvement of platelet-derived growth factor receptor β in fibrosis through extracellular matrix protein production after ischemic stroke. *Exp Neurol* **264**, 127–34 (2015).
28. Fernández-Klett, F. *et al.* Early loss of pericytes and perivascular stromal cell-induced scar formation after stroke. *J Cereb Blood Flow Metab* **33**, 428–439 (2013).
29. Dias, D. O. *et al.* Pericyte-derived fibrotic scarring is conserved across diverse central nervous system lesions. *Nature Communications* **12**, 5501 (2021).
30. Xu, L. *et al.* Fibroblasts repair blood-brain barrier damage and hemorrhagic brain injury via TIMP2. *Cell Reports* **41**, (2022).
31. Soderblom, C. *et al.* Perivascular fibroblasts form the fibrotic scar after contusive spinal cord injury. *J Neurosci* **33**, 13882–13887 (2013).
32. Pikor, N. B. *et al.* Integration of Th17- and Lymphotoxin-Derived Signals Initiates Meningeal-Resident Stromal Cell Remodeling to Propagate Neuroinflammation. *Immunity* **43**, 1160–73 (2015).
33. Cupovic, J. *et al.* Central Nervous System Stromal Cells Control Local CD8(+) T Cell Responses during Virus-Induced Neuroinflammation. *Immunity* **44**, 622–633 (2016).
34. Yang, A. C. *et al.* A human brain vascular atlas reveals diverse cell mediators of Alzheimer's disease risk. *bioRxiv* 2021.04.26.441262 (2021) doi:10.1101/2021.04.26.441262.

35. Jain, S. *et al.* Single-cell RNA sequencing and spatial transcriptomics reveal cancer-associated fibroblasts in glioblastoma with protumoral effects. *J Clin Invest* **133**, e147087.

36. Watanabe, R., Kakizaki, M., Ikehara, Y. & Togayachi, A. Formation of fibroblastic reticular network in the brain after infection with neurovirulent murine coronavirus. *Neuropathology* **36**, 513–526 (2016).

37. Månberg, A. *et al.* Altered perivascular fibroblast activity precedes ALS disease onset. *Nature Medicine* **27**, 640–646 (2021).

38. Dorrier, C. E. *et al.* CNS fibroblasts form a fibrotic scar in response to immune cell infiltration. *Nature Neuroscience* **24**, 234–244 (2021).

39. Dorrier, C. E., Jones, H. E., Pintarić, L., Siegenthaler, J. A. & Daneman, R. Emerging roles for CNS fibroblasts in health, injury and disease. *Nature Reviews Neuroscience* (2021) doi:10.1038/s41583-021-00525-w.

40. Buechler, M. B. *et al.* Cross-tissue organization of the fibroblast lineage. *Nature* (2021) doi:10.1038/s41586-021-03549-5.

41. Pradhan, R. N., Krishnamurty, A. T., Fletcher, A. L., Turley, S. J. & Müller, S. A bird's eye view of fibroblast heterogeneity: A pan-disease, pan-cancer perspective. *Immunological Reviews* **n/a**, (2021).

42. Dahlgren, M. W. *et al.* Adventitial Stromal Cells Define Group 2 Innate Lymphoid Cell Tissue Niches. *Immunity* **50**, 707-722.e6 (2019).

43. Boothby, I. C. *et al.* Early-life inflammation primes a T helper 2 cell–fibroblast niche in skin. *Nature* (2021) doi:10.1038/s41586-021-04044-7.

44. Smillie, C. S. *et al.* Intra- and Inter-cellular Rewiring of the Human Colon during Ulcerative Colitis. *Cell* **178**, 714-730.e22 (2019).

45. Kinchen, J. *et al.* Structural Remodeling of the Human Colonic Mesenchyme in Inflammatory Bowel Disease. *Cell* **175**, 372-386.e17 (2018).

46. Buckley, C. D. *et al.* Persistent induction of the chemokine receptor CXCR4 by TGF-beta 1 on synovial T cells contributes to their accumulation within the rheumatoid synovium. *J Immunol* **165**, 3423–9 (2000).

47. Croft, A. P. *et al.* Distinct fibroblast subsets drive inflammation and damage in arthritis. *Nature* **570**, 246–251 (2019).

48. Ko, K. I. *et al.* Distinct fibroblast progenitor subpopulation expedites regenerative mucosal healing by immunomodulation. *J Exp Med* **220**, e20221350 (2023).

49. Sbierski-Kind, J., Mroz, N. & Molofsky, A. B. Perivascular stromal cells: Directors of tissue immune niches. *Immunol Rev* (2021) doi:10.1111/imr.12984.

50. Yannick O. Alexandre *et al.* A diverse fibroblastic stromal cell landscape in the spleen directs tissue homeostasis and immunity. *Science Immunology* **7**, eabj0641 (2022).

51. Davidson, S. *et al.* Fibroblasts as immune regulators in infection, inflammation and cancer. *Nature Reviews Immunology* **21**, 704–717 (2021).

52. Kapoor, V. N. *et al.* Gremlin 1+ fibroblastic niche maintains dendritic cell homeostasis in lymphoid tissues. *Nature Immunology* (2021) doi:10.1038/s41590-021-00920-6.

53. Krausgruber, T. *et al.* Structural cells are key regulators of organ-specific immune responses. *Nature* **583**, 296–302 (2020).

54. Xu, Z. *et al.* Anatomically distinct fibroblast subsets determine skin autoimmune patterns. *Nature* (2021) doi:10.1038/s41586-021-04221-8.

55. Öhlund, D. *et al.* Distinct populations of inflammatory fibroblasts and myofibroblasts in pancreatic cancer. *The Journal of experimental medicine* **214**, 579–596 (2017).

56. Cautivo, K. M. *et al.* Interferon gamma constrains type 2 lymphocyte niche boundaries during mixed inflammation. *Immunity* **55**, 254-271.e7 (2022).

57. Cautivo, K. M., Steer, C. A. & Molofsky, A. B. Immune outposts in the adventitia: One foot in sea and one on shore. *Curr Opin Immunol* **64**, 34–41 (2020).

58. Hinz, B. The role of myofibroblasts in wound healing. *Curr Res Transl Med* **64**, 171–177 (2016).

59. Krishnamurty, A. T. *et al.* LRRC15+ myofibroblasts dictate the stromal setpoint to suppress tumour immunity. *Nature* **611**, 148–154 (2022).

60. Tsukui, T. *et al.* Collagen-producing lung cell atlas identifies multiple subsets with distinct localization and relevance to fibrosis. *Nature Communications* **11**, 1920–1920 (2020).

61. Kis, K., Liu, X. & Hagood, J. S. Myofibroblast differentiation and survival in fibrotic disease. *Expert Reviews in Molecular Medicine* **13**, e27 (2011).

62. Fabre, T. *et al.* Identification of a broadly fibrogenic macrophage subset induced by type 3 inflammation. *Science Immunology* **8**, eadd8945 (2023).

63. Tsukui, T. & Sheppard, D. Tracing the origin of pathologic pulmonary fibroblasts. *bioRxiv* 2022.11.18.517147 (2022) doi:10.1101/2022.11.18.517147.

64. Zhao, Z. *et al.* TGF-β promotes pericyte-myofibroblast transition in subretinal fibrosis through the Smad2/3 and Akt/mTOR pathways. *Exp Mol Med* **54**, 673–684 (2022).

65. Bonney, S. K., Sullivan, L. T., Cherry, T. J., Daneman, R. & Shih, A. Y. Distinct features of brain perivascular fibroblasts and mural cells revealed by in vivo two-photon imaging. *Journal of Cerebral Blood Flow & Metabolism* **42**, 966 (2021).
66. Mastorakos, P. & McGavern, D. The anatomy and immunology of vasculature in the central nervous system. *Science Immunology* **4**, eaav0492 (2019).
67. Jones, H. E. *et al.* Meningeal origins and dynamics of perivascular fibroblast development on the mouse cerebral vasculature. 2023.03.23.533982 Preprint at https://doi.org/10.1101/2023.03.23.533982 (2023).
68. Rustenhoven, J. *et al.* Functional characterization of the dural sinuses as a neuroimmune interface. *Cell* (2021) doi:https://doi.org/10.1016/j.cell.2020.12.040.
69. Rasmussen, M. K., Mestre, H. & Nedergaard, M. Fluid transport in the brain. *Physiological Reviews* **102**, 1025–1151 (2022).
70. Munk, A. S. *et al.* PDGF-B Is Required for Development of the Glymphatic System. *Cell Rep* **26**, 2955-2969.e3 (2019).
71. Pietilä, R. *et al.* Molecular anatomy of adult mouse leptomeninges. *Neuron* **0**, (2023).
72. Kearns, N. *et al.* Dissecting the Human Leptomeninges at single-cell resolution. 2022.12.15.520647 Preprint at https://doi.org/10.1101/2022.12.15.520647 (2022).
73. Saunders, A. *et al.* Molecular Diversity and Specializations among the Cells of the Adult Mouse Brain. *Cell* **174**, 1015-1030.e16 (2018).
74. Vanlandewijck, M. *et al.* A molecular atlas of cell types and zonation in the brain vasculature. *Nature* **554**, 475–480 (2018).

75. DeSisto, J. *et al.* Single-Cell Transcriptomic Analyses of the Developing Meninges Reveal Meningeal Fibroblast Diversity and Function. *Developmental Cell* **54**, 43-59.e4 (2020).

76. Holl, D. *et al.* Distinct origin and region-dependent contribution of stromal fibroblasts to fibrosis following traumatic injury in mice. *Nat Neurosci* 1–14 (2024) doi:10.1038/s41593-024-01678-4.

77. Xue, X. *et al.* Heterogeneous fibroblasts contribute to fibrotic scar formation after spinal cord injury in mice and monkeys. *Nat Commun* **15**, 6321 (2024).

78. Franklin, R. A. Fibroblasts and macrophages: Collaborators in tissue homeostasis. *Immunological Reviews* **n/a**, (2021).

79. Norris, G. T. & Kipnis, J. Immune cells and CNS physiology: Microglia and beyond. *The Journal of experimental medicine* **216**, 60–70 (2019).

80. Weinhard, L. *et al.* Microglia remodel synapses by presynaptic trogocytosis and spine head filopodia induction. *Nat Commun* **9**, 1228 (2018).

81. Han, R. T. *et al.* Microglial pattern recognition via IL-33 promotes synaptic refinement in developing corticothalamic circuits in mice. *J Exp Med* **220**, e20220605 (2022).

82. Nguyen, P. T. *et al.* Microglial Remodeling of the Extracellular Matrix Promotes Synapse Plasticity. *Cell* **182**, 388-403.e15 (2020).

83. O'Keeffe, M. *et al.* Typical development of synaptic and neuronal properties can proceed without microglia in the cortex and thalamus. *Nat Neurosci* 1–12 (2025) doi:10.1038/s41593-024-01833-x.

84. Kierdorf, K., Masuda, T., Jordão, M. J. C. & Prinz, M. Macrophages at CNS interfaces: ontogeny and function in health and disease. *Nature Reviews Neuroscience* **20**, 547–562 (2019).

85. Masuda, T. *et al.* Specification of CNS macrophage subsets occurs postnatally in defined niches. *Nature* (2022) doi:10.1038/s41586-022-04596-2.

86. Drieu, A. *et al.* Parenchymal border macrophages regulate the flow dynamics of the cerebrospinal fluid. *Nature* (2022) doi:10.1038/s41586-022-05397-3.

87. Iadecola, C. & Anrather, J. The immunology of stroke and dementia. *Immunity* **58**, 18–39 (2025).

88. Rayasam, A. *et al.* Immune responses in stroke: how the immune system contributes to damage and healing after stroke and how this knowledge could be translated to better cures? *Immunology* **154**, 363–376 (2018).

89. Beuker, C. *et al.* Stroke induces disease-specific myeloid cells in the brain parenchyma and pia. *Nature Communications* **13**, 945 (2022).

90. De Vlaminck, K. *et al.* Differential plasticity and fate of brain-resident and recruited macrophages during the onset and resolution of neuroinflammation. *Immunity* doi:10.1016/j.immuni.2022.09.005.

91. Mastorakos, P. *et al.* Temporally distinct myeloid cell responses mediate damage and repair after cerebrovascular injury. *Nature Neuroscience* **24**, 245–258 (2021).

92. Choi, B.-R., Johnson, K. R., Maric, D. & McGavern, D. B. Monocyte-derived IL-6 programs microglia to rebuild damaged brain vasculature. *Nat Immunol* 1–14 (2023) doi:10.1038/s41590-023-01521-1.

93. Chen, H.-R. *et al.* Fate mapping via CCR2-CreER mice reveals monocyte-to-microglia transition in development and neonatal stroke. *Sci Adv* **6**, eabb2119–eabb2119 (2020).
94. Deczkowska, A. *et al.* Disease-Associated Microglia: A Universal Immune Sensor of Neurodegeneration. *Cell* **173**, 1073–1081 (2018).
95. Keren-Shaul, H. *et al.* A Unique Microglia Type Associated with Restricting Development of Alzheimer's Disease. *Cell* **169**, 1276-1290.e17 (2017).
96. Zhou, X. *et al.* Circuit Design Features of a Stable Two-Cell System. *Cell* **172**, 744-757.e17 (2018).
97. King, E. M. *et al.* Gpnmb and Spp1 mark a conserved macrophage injury response masking fibrosis-specific programming in the lung. https://insight.jci.org/articles/view/182700/sd/6 (2024) doi:10.1172/jci.insight.182700.
98. Buechler, M. B., Fu, W. & Turley, S. J. Fibroblast-macrophage reciprocal interactions in health, fibrosis, and cancer. *Immunity* **54**, 903–915 (2021).
99. Hoeft, K. *et al.* Platelet-instructed SPP1+ macrophages drive myofibroblast activation in fibrosis in a CXCL4-dependent manner. *Cell Reports* **42**, (2023).
100. Frangogiannis, N. Transforming growth factor-β in tissue fibrosis. *The Journal of experimental medicine* **217**, e20190103–e20190103 (2020).
101. Young, L. R. *et al.* Epithelial-macrophage interactions determine pulmonary fibrosis susceptibility in Hermansky-Pudlak syndrome. *JCI Insight* **1**, (2016).

102. Juban, G. *et al.* AMPK Activation Regulates LTBP4-Dependent TGF-β1 Secretion by Pro-inflammatory Macrophages and Controls Fibrosis in Duchenne Muscular Dystrophy. *Cell Rep* **25**, 2163-2176.e6 (2018).
103. Dewald, O. *et al.* CCL2/Monocyte Chemoattractant Protein-1 regulates inflammatory responses critical to healing myocardial infarcts. *Circ Res* **96**, 881–9 (2005).
104. Frangogiannis, N. G. *et al.* Critical role of monocyte chemoattractant protein-1/CC chemokine ligand 2 in the pathogenesis of ischemic cardiomyopathy. *Circulation* **115**, 584–92 (2007).
105. Behr, F. M., Chuwonpad, A., Stark, R. & van Gisbergen, K. P. J. M. Armed and Ready: Transcriptional Regulation of Tissue-Resident Memory CD8 T Cells. *Frontiers in Immunology* **9**, (2018).
106. Pasciuto, E. *et al.* Microglia Require CD4 T Cells to Complete the Fetal-to-Adult Transition. *Cell* **182**, 625-640.e24 (2020).
107. Louveau, A., Harris, T. H. & Kipnis, J. Revisiting the concept of CNS immune privilege. *Trends Immunol* **36**, 569–577 (2015).
108. Alves de Lima, K. *et al.* Meningeal γδ T cells regulate anxiety-like behavior via IL-17a signaling in neurons. *Nat Immunol* **21**, 1421–1429 (2020).
109. Filiano, A. J. *et al.* Unexpected role of interferon-γ in regulating neuronal connectivity and social behaviour. *Nature* **535**, 425–429 (2016).
110. Fu, Z. *et al.* GABAergic neuronal IL-4R mediates T cell effect on memory. *Neuron* 2021.03.16.435727 (2021) doi:10.1101/2021.03.16.435727.

111. Javidi, E. & Magnus, T. Autoimmunity After Ischemic Stroke and Brain Injury. *Frontiers in Immunology* **10**, (2019).

112. Gao, W. *et al.* Engineered T cell therapy for central nervous system injury. *Nature* 1–9 (2024) doi:10.1038/s41586-024-07906-y.

113. Planas Anna, M. Role of Immune Cells Migrating to the Ischemic Brain. *Stroke* **49**, 2261–2267 (2018).

114. Gokhan Yilmaz, Thiruma V. Arumugam, Karen Y. Stokes & D. Neil Granger. Role of T Lymphocytes and Interferon-γ in Ischemic Stroke. *Circulation* **113**, 2105–2112 (2006).

115. Ito, M. *et al.* Brain regulatory T cells suppress astrogliosis and potentiate neurological recovery. *Nature* **565**, 246–250 (2019).

116. Shi, L. *et al.* Treg cell-derived osteopontin promotes microglia-mediated white matter repair after ischemic stroke. *Immunity* (2021) doi:10.1016/j.immuni.2021.04.022.

117. Selvaraj, U. M. & Stowe, A. M. Long-term T cell responses in the brain after an ischemic stroke. *Discov Med* **24**, 323–333 (2017).

118. Mroz, N. M. *et al.* Type 1 lymphocytes and interferon-γ accumulate in the thalamus and restrict seizure susceptibility after traumatic brain injury. 2024.12.28.630606 Preprint at https://doi.org/10.1101/2024.12.28.630606 (2024).

119. Landrith, T. A. *et al.* CD103+ CD8 T Cells in the Toxoplasma-Infected Brain Exhibit a Tissue-Resident Memory Transcriptional Profile. *Frontiers in Immunology* **8**, (2017).

120. Steinbach, K. *et al.* Brain-resident memory T cells represent an autonomous cytotoxic barrier to viral infection. *The Journal of experimental medicine* **213**, 1571–87 (2016).

121. Ilena Vincenti *et al.* Tissue-resident memory $CD8^+$ T cells cooperate with $CD4^+$ T cells to drive compartmentalized immunopathology in the CNS. *Science Translational Medicine* **14**, eabl6058 (2022).

122. David Frieser *et al.* Tissue-resident $CD8^+$ T cells drive compartmentalized and chronic autoimmune damage against CNS neurons. *Science Translational Medicine* **14**, eabl6157 (2022).

123. Wakim, L. M. *et al.* The molecular signature of tissue resident memory CD8 T cells isolated from the brain. *J Immunol* **189**, 3462–71 (2012).

124. Linda M. Wakim, Amanda Woodward-Davis & Michael J. Bevan. Memory T cells persisting within the brain after local infection show functional adaptations to their tissue of residence. *Proceedings of the National Academy of Sciences* **107**, 17872–17879 (2010).

125. Garber, C. *et al.* T cells promote microglia-mediated synaptic elimination and cognitive dysfunction during recovery from neuropathogenic flaviviruses. *Nat Neurosci* **22**, 1276–1288 (2019).

126. Brigas, H. C. *et al.* IL-17 triggers the onset of cognitive and synaptic deficits in early stages of Alzheimer's disease. *Cell Reports* **36**, 109574 (2021).

127. Gate, D. *et al.* Clonally expanded CD8 T cells patrol the cerebrospinal fluid in Alzheimer's disease. *Nature* **577**, 399–404 (2020).

128. Chen, X. *et al.* Microglia-mediated T cell infiltration drives neurodegeneration in tauopathy. *Nature* 1–10 (2023) doi:10.1038/s41586-023-05788-0.
129. Tsukui, T., Wolters, P. J. & Sheppard, D. Alveolar fibroblast lineage orchestrates lung inflammation and fibrosis. *Nature* 1–8 (2024) doi:10.1038/s41586-024-07660-1.
130. Dobie, R. *et al.* Single-Cell Transcriptomics Uncovers Zonation of Function in the Mesenchyme during Liver Fibrosis. *Cell Reports* **29**, 1832 (2019).
131. Boghdadi, A. G. *et al.* NogoA-expressing astrocytes limit peripheral macrophage infiltration after ischemic brain injury in primates. *Nature Communications* **12**, 6906 (2021).
132. Garza, R. *et al.* Single-cell transcriptomics of resected human traumatic brain injury tissues reveals acute activation of endogenous retroviruses in oligodendroglia. 2022.09.07.506982 Preprint at https://doi.org/10.1101/2022.09.07.506982 (2023).
133. Griffith, J. W., Sokol, C. L. & Luster, A. D. Chemokines and chemokine receptors: positioning cells for host defense and immunity. *Annu Rev Immunol* **32**, 659–702 (2014).
134. Levard, D. *et al.* Central nervous system-associated macrophages modulate the immune response following stroke in aged mice. *Nat Neurosci* 1–13 (2024) doi:10.1038/s41593-024-01695-3.
135. Derynck, R. & Budi, E. H. Specificity, versatility, and control of TGF-β family signaling. *Science Signaling* **12**, eaav5183 (2019).
136. Glushakova, O. Y. *et al.* Role of Caspase-3-Mediated Apoptosis in Chronic Caspase-3-Cleaved Tau Accumulation and Blood-Brain Barrier Damage in the

Corpus Callosum after Traumatic Brain Injury in Rats. *J Neurotrauma* **35**, 157–173 (2018).

137. Henderson, N. C. *et al.* Targeting of αv integrin identifies a core molecular pathway that regulates fibrosis in several organs. *Nat Med* **19**, 1617–1624 (2013).
138. Yin, Z. *et al.* APOE4 impairs the microglial response in Alzheimer's disease by inducing TGFβ-mediated checkpoints. *Nat Immunol* **24**, 1839–1853 (2023).
139. Arnold, T. D. *et al.* Impaired αVβ8 and TGFβ signaling lead to microglial dysmaturation and neuromotor dysfunction. *Journal of Experimental Medicine* **216**, 900–915 (2019).
140. McKinsey, G. L. *et al.* Radial glia control microglial differentiation via integrin avb8-dependent trans-activation of TGFB1. 2023.07.13.548459 Preprint at https://doi.org/10.1101/2023.07.13.548459 (2023).
141. Knezic, A., Broughton, B. R. S., Widdop, R. E. & McCarthy, C. A. Optimising the photothrombotic model of stroke in the C57Bl/6 and FVB/N strains of mouse. *Sci Rep* **12**, 7598 (2022).
142. Sommer, C. J. Ischemic stroke: experimental models and reality. *Acta Neuropathol* **133**, 245–261 (2017).
143. Zhu, Y. & Murakami, F. Chemokine CXCL12 and its receptors in the developing central nervous system: Emerging themes and future perspectives. *Developmental Neurobiology* **72**, 1349–1362 (2012).
144. Kim, C. C., Nakamura, M. C. & Hsieh, C. L. Brain trauma elicits non-canonical macrophage activation states. *J Neuroinflammation* **13**, 117 (2016).

145. Ransohoff, R. M. A polarizing question: do M1 and M2 microglia exist? *Nat Neurosci* **19**, 987–991 (2016).
146. Hammond, T. R. *et al.* Single-Cell RNA Sequencing of Microglia throughout the Mouse Lifespan and in the Injured Brain Reveals Complex Cell-State Changes. *Immunity* **50**, 253-271.e6 (2019).
147. Salmon, H. *et al.* Matrix architecture defines the preferential localization and migration of T cells into the stroma of human lung tumors. *J Clin Invest* **122**, 899–910 (2012).
148. Rustenhoven, J. & Kipnis, J. Brain borders at the central stage of neuroimmunology. *Nature* **612**, 417–429 (2022).
149. Junghof, J. *et al.* CDH18 is a fetal epicardial biomarker regulating differentiation towards vascular smooth muscle cells. *npj Regen Med* **7**, 1–14 (2022).
150. Lepore, J. J. *et al.* GATA-6 regulates semaphorin 3C and is required in cardiac neural crest for cardiovascular morphogenesis. *J Clin Invest* **116**, 929–939 (2006).
151. He, L. *et al.* Preexisting endothelial cells mediate cardiac neovascularization after injury. *J Clin Invest* **127**, 2968–2981 (2017).
152. Krempen, K. *et al.* Far upstream regulatory elements enhance position-independent and uterus-specific expression of the murine alpha1(I) collagen promoter in transgenic mice. *Gene Expr* **8**, 151–163 (1999).
153. Hamilton, T. G., Klinghoffer, R. A., Corrin, P. D. & Soriano, P. Evolutionary divergence of platelet-derived growth factor alpha receptor signaling mechanisms. *Mol Cell Biol* **23**, 4013–4025 (2003).

154. Rivers, L. E. *et al.* PDGFRA/NG2 glia generate myelinating oligodendrocytes and piriform projection neurons in adult mice. *Nat Neurosci* **11**, 10.1038/nn.2220 (2008).

155. Šošić, D., Richardson, J. A., Yu, K., Ornitz, D. M. & Olson, E. N. Twist regulates cytokine gene expression through a negative feedback loop that represses NF-kappaB activity. *Cell* **112**, 169–180 (2003).

156. Wendling, O., Bornert, J.-M., Chambon, P. & Metzger, D. Efficient temporally-controlled targeted mutagenesis in smooth muscle cells of the adult mouse. *genesis* **47**, 14–18 (2009).

157. Zhu, X. *et al.* Age-dependent fate and lineage restriction of single NG2 cells. *Development (Cambridge, England)* **138**, 745 (2011).

158. Guo, X. *et al.* Atp13a5 Marker Reveals Pericyte Specification in the Mouse Central Nervous System. *J Neurosci* **44**, e0727242024 (2024).

159. Lee, P. P. *et al.* A critical role for Dnmt1 and DNA methylation in T cell development, function, and survival. *Immunity* **15**, 763–774 (2001).

160. Zhu, J. *et al.* The transcription factor T-bet is induced by multiple pathways and prevents an endogenous Th2 cell program during Th1 cell responses. *Immunity* **37**, 660–673 (2012).

161. Li, M. O., Wan, Y. Y. & Flavell, R. A. T Cell-Produced Transforming Growth Factor-β1 Controls T Cell Tolerance and Regulates Th1- and Th17-Cell Differentiation. *Immunity* **26**, 579–591 (2007).

162. Chytil, A., Magnuson, M. A., Wright, C. V. E. & Moses, H. L. Conditional inactivation of the TGF-β type II receptor using Cre:Lox. *genesis* **32**, 73–75 (2002).

163. Nakawesi, J. *et al.* αvβ8 integrin-expression by BATF3-dependent dendritic cells facilitates early IgA responses to Rotavirus. *Mucosal Immunol* **14**, 53–67 (2021).
164. Proctor, J. M., Zang, K., Wang, D., Wang, R. & Reichardt, L. F. Vascular Development of the Brain Requires β8 Integrin Expression in the Neuroepithelium. *J. Neurosci.* **25**, 9940–9948 (2005).
165. Gorski, J. A. *et al.* Cortical excitatory neurons and glia, but not GABAergic neurons, are produced in the Emx1-expressing lineage. *J Neurosci* **22**, 6309–6314 (2002).
166. Sudwarts, A. *et al.* BIN1 is a key regulator of proinflammatory and neurodegeneration-related activation in microglia. *Mol Neurodegener* **17**, 33 (2022).
167. Fernández-Chacón, M. *et al.* iSuRe-Cre is a genetic tool to reliably induce and report Cre-dependent genetic modifications. *Nat Commun* **10**, 2262 (2019).
168. Cohen, J. N. *et al.* Regulatory T cells in skin mediate immune privilege of the hair follicle stem cell niche. *Science Immunology* **9**, eadh0152 (2024).
169. Labat-gest, V. & Tomasi, S. Photothrombotic ischemia: a minimally invasive and reproducible photochemical cortical lesion model for mouse stroke studies. *J Vis Exp* 50370 (2013) doi:10.3791/50370.
170. Lee, J. K. *et al.* Photochemically induced cerebral ischemia in a mouse model. *Surg Neurol* **67**, 620–5; discussion 625 (2007).
171. Liu, N.-W. *et al.* Evolutional Characterization of Photochemically Induced Stroke in Rats: a Multimodality Imaging and Molecular Biological Study. *Translational Stroke Research* **8**, 244–256 (2017).

172. Gonzalez, F. F. *et al.* Erythropoietin increases neurogenesis and oligodendrogliosis of subventricular zone precursor cells after neonatal stroke. *Stroke* **44**, 753–758 (2013).
173. McKinsey, G. L. *et al.* A new genetic strategy for targeting microglia in development and disease. *eLife* **9**, e54590 (2020).
174. Larpthaveesarp, A. & Gonzalez, F. F. Transient Middle Cerebral Artery Occlusion Model of Neonatal Stroke in P10 Rats. *J Vis Exp* 54830 (2017) doi:10.3791/54830.
175. Llovera, G., Roth, S., Plesnila, N., Veltkamp, R. & Liesz, A. Modeling Stroke in Mice: Permanent Coagulation of the Distal Middle Cerebral Artery. *JoVE (Journal of Visualized Experiments)* e51729 (2014) doi:10.3791/51729.
176. Teo, L. *et al.* Replicating infant-specific reactive astrocyte functions in the injured adult brain. *Prog Neurobiol* **204**, 102108 (2021).
177. Teo, L. & Bourne, J. A. A Reproducible and Translatable Model of Focal Ischemia in the Visual Cortex of Infant and Adult Marmoset Monkeys. *Brain Pathology* **24**, 459–474 (2014).
178. Stockis, J. *et al.* Blocking immunosuppression by human Tregs in vivo with antibodies targeting integrin αVβ8. *Proc Natl Acad Sci U S A* **114**, E10161–E10168 (2017).
179. Dodagatta-Marri, E. *et al.* Integrin αvβ8 on T cells suppresses anti-tumor immunity in multiple models and is a promising target for tumor immunotherapy. *Cell Reports* **36**, 109309 (2021).
180. Renier, N. *et al.* iDISCO: A Simple, Rapid Method to Immunolabel Large Tissue Samples for Volume Imaging. *Cell* **159**, 896–910 (2014).

181. Slyper, M. *et al.* A single-cell and single-nucleus RNA-Seq toolbox for fresh and frozen human tumors. *Nat Med* **26**, 792–802 (2020).
182. Galatro, T. F., Vainchtein, I. D., Brouwer, N., Boddeke, E. W. G. M. & Eggen, B. J. L. Isolation of Microglia and Immune Infiltrates from Mouse and Primate Central Nervous System. *Methods Mol Biol* **1559**, 333–342 (2017).
183. Nott, A., Schlachetzki, J. C. M., Fixsen, B. R. & Glass, C. K. Nuclei isolation of multiple brain cell types for omics interrogation. *Nat Protoc* **16**, 1629–1646 (2021).
184. Radu, M. & Chernoff, J. An in vivo Assay to Test Blood Vessel Permeability. *J Vis Exp* 50062 (2013) doi:10.3791/50062.
185. Hao, Y. *et al.* Integrated analysis of multimodal single-cell data. *Cell* **184**, 3573-3587.e29 (2021).
186. Blighe, K. *et al.* EnhancedVolcano: Publication-ready volcano plots with enhanced colouring and labeling. Bioconductor version: Release (3.18) https://doi.org/10.18129/B9.bioc.EnhancedVolcano (2023).
187. Sbierski-Kind, J. *et al.* Group 2 innate lymphoid cells constrain type 3/17 lymphocytes in shared stromal niches to restrict liver fibrosis. 2023.04.26.537913 Preprint at https://doi.org/10.1101/2023.04.26.537913 (2023).
188. Lenburg, M. E., Sinha, A., Faller, D. V. & Denis, G. V. Tumor-specific and Proliferation-specific Gene Expression Typifies Murine Transgenic B Cell Lymphomagenesis. *J Biol Chem* **282**, 4803 (2007).
189. Whitfield, M. L., George, L. K., Grant, G. D. & Perou, C. M. Common markers of proliferation. *Nat Rev Cancer* **6**, 99–106 (2006).

190. Korsunsky, I., Nathan, A., Millard, N. & Raychaudhuri, S. Presto scales Wilcoxon and auROC analyses to millions of observations. 653253 Preprint at https://doi.org/10.1101/653253 (2019).
191. Alquicira-Hernandez, J. & Powell, J. E. Nebulosa recovers single-cell gene expression signals by kernel density estimation. *Bioinformatics* **37**, 2485–2487 (2021).
192. Marsh, S. samuel-marsh/scCustomize: Version 2.0.1. doi:10.5281/zenodo.10161832.
193. Wu, T. *et al.* clusterProfiler 4.0: A universal enrichment tool for interpreting omics data. *Innovation (Camb)* **2**, 100141 (2021).
194. Browaeys, R., Saelens, W. & Saeys, Y. NicheNet: modeling intercellular communication by linking ligands to target genes. *Nat Methods* **17**, 159–162 (2020).
195. Cable, D. M. *et al.* Robust decomposition of cell type mixtures in spatial transcriptomics. *Nat Biotechnol* **40**, 517–526 (2022).
196. Garcia-Alonso, L. *et al.* Single-cell roadmap of human gonadal development. *Nature* **607**, 540–547 (2022).
197. Korsunsky, I. *et al.* Fast, sensitive and accurate integration of single-cell data with Harmony. *Nat Methods* **16**, 1289–1296 (2019).
198. Biffi, G. *et al.* IL1-Induced JAK/STAT Signaling Is Antagonized by TGFβ to Shape CAF Heterogeneity in Pancreatic Ductal Adenocarcinoma. *Cancer Discov* **9**, 282–301 (2019).

199. Koncina, E. *et al.* IL1R1+ cancer-associated fibroblasts drive tumor development and immunosuppression in colorectal cancer. *Nat Commun* **14**, 4251 (2023).

Publishing Agreement

It is the policy of the University to encourage open access and broad distribution of all theses, dissertations, and manuscripts. The Graduate Division will facilitate the distribution of UCSF theses, dissertations, and manuscripts to the UCSF Library for open access and distribution. UCSF will make such theses, dissertations, and manuscripts accessible to the public and will take reasonable steps to preserve these works in perpetuity.

I hereby grant the non-exclusive, perpetual right to The Regents of the University of California to reproduce, publicly display, distribute, preserve, and publish copies of my thesis, dissertation, or manuscript in any form or media, now existing or later derived, including access online for teaching, research, and public service purposes.

DocuSigned by:
Nathan Ewing-Crystal
2BADA938CD1F460...
Author Signature

1/22/2025
Date